Evaluation of Rock Particle Media Shape Contribution to Abrasive Wear

by

Steven Duncan

A thesis submitted in partial fulfillment of the requirements for the degree of

Master of Science

in

Mining Engineering

Department of Civil and Environmental Engineering
University of Alberta

# ABSTRACT

Chrome carbide samples prepared using submerged arc welding procedures were subjected to physical abrasion testing in a modified machine similar to the ASTM G65 standard, in an investigation of media particle shape contribution to abrasive wear. The primary intent of this study was to determine what correlation existed between abrasive media particle shape and abrasive wear rate, in a test that was designed to closely mimic field conditions, in order to better predict potential severity of abrasive wear. As secondary objectives, the uses of specific energy were to be examined, as well as the use of abrasive media angle of repose to determine particle shape characteristics. The investigation of specific energy was intended to be used in the extrapolation of lab results to field conditions, to better assist industry in the prediction and prevention of abrasive wear through improved testing. Abrasive media types utilized were: raw oil sand with bitumen fraction stripped, sand collected from an oil sand tailings beach, granite rock crushed to small particle sizes, and cube mould test sand. Normal force load was derived from field shovel excavator force data. Measured abrasive media shape parameters included form factor, form index, angularity index, convexity, angularity parameter, spike parameter quadratic fit and texture. All abrasive shape parameters displayed excellent correlation with abrasive wear rates; $R^2$ coefficients for correlation between abrasive wear rate and shape parameters were 0.9966, 0.9241, 0.9825, 0.8901, 0.9422, 0.9476, and 0.8778, respectively. The particle size effect was particularly evident in testing with the tailings beach sand, where extremely low abrasive rates were found. Texture parameter was found to correlate closely with media angle of repose, suggesting it may be an easy, quick and effective way for industry to estimate shape parameters which heavily influenced abrasivity of media. Specific energy of lab and field tests were found to not be closely correlated, but still within an order of magnitude, suggesting that while it may still be an effective extrapolation method of lab results for industry, more investigation is required.

# ACKNOWLEDGEMENTS

I would like to extend my gratitude towards Syncrude Canada, who provided the two oil sand media samples, as well as Wilkinson Steel and Metals in Edmonton, who provided the chrome carbide samples. Without this sort of help from industry, many projects would never be possible.

I would like to thank my supervisors, Dr. Patricio Mendez, Dr. Tim Joseph, as well as Dr. Jozef Szymanski for their patience, knowledge and guidance. Without their help, this thesis would not have been possible, and I am forever grateful for their input.

The entire lab at the Canadian Center for Welding and Joining were an invaluable asset throughout my entire journey to complete this thesis. Their incredible knowledge, guidance and support were invaluable to me. Their lab is among the best in the world, and without access to their help I would never have been able to complete my study.

Next, I would like to extend a special thank you to my friend and colleague, Mark Curley. He was always there throughout my studies to provide support and encouragement, as well as acting as a sounding board for ideas, thoughts and concepts.

Finally, I would like to extend a heartfelt thank you to my friends and family, who provided the love and encouragement I needed.

# TABLE OF CONTENTS

# LIST OF TABLES

# LIST OF FIGURES

# 1 Introduction

Wear, in the broadest sense of the term, refers to the loss of material from a solid surface, caused by relative motion between that surface and another body. It is a global issue, stretching across every industry, and is a multi-billion dollar problem in the mining industry.

One of the most damaging types of wear is abrasive wear, which refers to the loss of material through the scratching of one surface by a harder surface or particle. Of particular interest to the mining industry is abrasive wear of a surface (material) caused by impinging particles (media). This type of wear has many influencing factors including media shape, size and hardness; as well as material hardness and composition. The speed of interactions between media and material as well as the normal force associated with these interactions also play a significant role.

The major focus of this work was the investigation of particle shape and its relationship with two body abrasive wear, under actual field abrasive conditions. It has been shown in the literature that particle shape correlates closely with abrasive wear rates; however the majority of these studies were conducted under idealized conditions that are not representative of those found in the field. As a secondary foci, particle surface friction as a function of angle of repose was investigated, particularly its relationship with shape characteristics and associated abrasive wear rate. Finally, the energy required to cause a unit volume of abrasive wear (specific energy) was explored in an attempt to be able to extrapolate experimental results to predict wear in actual mining systems.

This work relied on the ASTM standard G65 test for abrasive wear, with significant changes made to better reflect field conditions. Power draw of an ultra-class shovel was analyzed to determine forces experienced at the equipment-ground interaction through a number of dig cycles. This force was then used as the normal force applied for the abrasion testing, which was done with abrasive media that could be found in actual field abrasive scenarios.

Sand particles were taken from four different sources to be used as abrasive media in the testing of surfaces. These particles were imaged with a scanning electron microscope and analyzed to determine various particle shape characteristics. Correlation between particle shape factors, angle of repose and abrasive wear rates were analysed and presented as the basis for further conclusions.

## 1.1 Postulates

In order to facilitate testing, three major postulates were required:

1. The bitumen content of the oil sand used as an abrasive media plays a negligible role in overall abrasive wear, and therefore can be stripped from the sand, which will still form an abrasive media indicative of field conditions.
2. The destruction of media particles through breakage during testing does not play a significant role in altering particle shape characteristics, as abrasive media is only re-used a small number of times.
3. When all other media characteristics are kept relatively constant (size, hardness), and are exposed to the same loading conditions (speed, normal force), particle shape is the dominating factor in abrasive potential.

## 1.2 Hypotheses

Three hypotheses form the major basis of this work, all of which are equally applicable of lab scale tests or full size tests in the field:

1. The consensus that more angular particles produce higher abrasive wear rates will hold true under a test that is truly indicative of field conditions.
2. Media angle of repose is an excellent indicator of particle surface friction properties, which in turn is closely tied to particle shape, and therefore will closely correlate with not only particle shape parameters but also abrasive wear rates.
3. Specific energy is a constant value based upon the hardness of material, and can be used in the extrapolation of lab results to field conditions.

It is expected that this study will result in a better understanding of the role that particle shape plays in abrasive wear, as well as shed light on the accuracy of what may be an easier indirect method (angle of repose) to measure overall particle rugosity, as opposed to the direct analysis of particles. Ultimately, it is hoped that the investigation carried out will contribute to the comprehension of abrasive wear characteristics and assist in better prediction of field wear performance.

# 2 Literature Review

## 2.1 Athabasca Oil Sands

### 2.1.1 Introduction

The Athabasca Oil Sands, located in the north-eastern portion of Alberta, represent a tremendous economic opportunity for not only that province, but also the entire country of Canada. The Alberta Energy Regulator has estimated Canada's oil reserves to be 169 billion barrels proven (the third largest proven reserve in the world), with 167 billion of those barrels contained within the oil sands (Alberta Energy Regulator, 2014). In terms of oil reserves, Canada is one of only two countries in the top 10 not associated with OPEC (the other being Russia), and as such represents a remarkable source of stable oil production for the world (US EIA, 2014). However, the technical issues associated with the development of the Athabasca Oil Sands are immense and offer incredible engineering challenges.

The Athabasca Oil Sand deposit consists of 4-18 wt% bitumen, 55-80 wt% inorganic materials, and 2-15wt% water (Osacky, Geramian, Ivey, Liu, and Etsell, 2013). Deep deposits are typically recovered using steam assisted gravity drainage techniques, whereas shallow deposits are amenable to surface mining methods, using large cable or hydraulic driven shovels and massive trucks. Major issues arise in the mining and processing of oil sands ore due to the degradation of equipment by wear and corrosion, not only through replacement of equipment, but also lost production.

### 2.1.2 Lithology

The Athabasca Oil Sands are found in the McMurray and Clearwater formations of north-eastern Alberta, with the majority of oil found within the McMurray formation (Carrigy, 1966). The thickness of this formation averages approximately 60m, but is quite variable with a diverse lithology that includes beds of conglomerate and coarse grained sands as well as laminated silt (Carrigy, 1966). The inorganic portion of the deposit consists mostly of quartz grains (95%), feldspar grains (2-3%), mica flakes and clay particles (2-3%), with traces of other minerals scattered throughout (Mossop, 1980).

Carrigy (1966, 1959) proposed the separation of the Athabasca oil sands into three different classes based on grain size. Within each of these classes, mineral composition varies. The classifications are given here:

#### *2.1.2.1 Class I Type*

The lower portion of the McMurray formation is typically composed of coarse grained sand, defined by Carrigy as

> "having a maximum size greater than 1mm, more than 80% by weight of a size greater than 74 microns, median diameter greater than 130 microns, and a cumulative curve which falls in the Class 1 envelope" (Carrigy,1966).

Mineral composition of these sands is mostly quartz grains that are

> "worn but not well rounded" (Carrigy, 1966)

Also present are potash feldspar (0-3.5%) and chert (0-2.5%), as well as various non-opaque heavy minerals (mostly garnet, staurolite, kyanite, and tourmaline) (Carrigy, 1966).

#### *2.1.2.2 Class II Type*

To be categorized as Class II, the finer grained sands that tend to overly Class I sand must contain

> "more than 80% of a sample by weight greater than 74 microns, maximum size is less than 300 microns, and median diameter is between 180 and 90 microns" (Carrigy, 1966).

These sands tend to be the richest in oil of the three classes, averaging 14.02wt% oil. Similar to Class I, Class II sands are composed of mostly quartz, feldspars (<8%) and mica (<5%), with the quartz varying in form from angular to well rounded. Heavy minerals present in Class II sands include chloritoid, tourmaline, garnet, staurolite, kyanite, zircon, rutile and apatite (Carrigy, 1966).

#### *2.1.2.3 Class III Type*

Materials categorized as Class III are

> "all that sediment with less than 80% of the total weight greater than 74 microns and with median diameters less than 120 microns" (Carrigy, 1966).

These types of sediments can contain significant amounts of oil and are have a similar mineral content to Class II sands, with quartz, feldspars and mica commonly found. Heavy mineral content is also similar to Class II sands (Carrigy, 1966).

The mineral types associated with these classes, and where they belong in the Upper, Middle and Lower members of the McMurray formation are given in Table 2-1.

#### *2.1.2.4 Abrasivity*

The main focus of this work revolved around the abrasivity of sand particles, and what influence particle angularity may have on abrasion rate. Generally speaking, smaller sand particles equate to longer fluvial transportation distances, and therefore less angular particles. For this reason, the finer Class II and III sands found in the upper and middle McMurray formation should be expected to be more rounded than the coarser Class I sands found in the middle and lower McMurray formation. In the Class I sands, a higher percentage of extremely hard garnet, staurolite and kyanite would also be expected to increase abrasivity of that sand type. Additionally, it has been proven by several studies that larger particles tend to cause higher amounts of abrasive wear; this phenomenon is covered in section 2.2.3.2 below. For these reasons the coarser Class I sand would be expected to show the highest amount of wear.

Table 2-1: Lithographic Data for the McMurray formation of the Athabasca Oil Sands (Adapted from Carrigy, 1966; Web Mineral, 2012; University of Minnesota, 2009; World Mineral Exchange, 2014; King, 2014)

| | Grain Size | Oil Content | Major Constituents | Moh's Hardness | Significant Non-Opaque Minerals | Moh's Hardness | Clay Minerals |
|---|---|---|---|---|---|---|---|
| Upper | Silt, Very Fine Sand (Class III) | Thin oil sand layers interbedded with barren silts or mottled oil impregnation/staining | Quartz<br>K-Feldspar<br>Muscovite | 7<br>6<br>3 | Choloritoid<br>Tourmaline<br>Zircon | 6.5<br>7.5<br>7.5 | Kaolinite<br>Illite |
| Middle | Fine Sand (Class II) | Rich, uniform, pregnant | Quartz<br>K-Feldspar<br>Muscovite | 7<br>6<br>3 | Tourmaline<br>Zircon<br>Choloritoid | 7.5<br>7.5<br>6.5 | Kaolinite<br>Illite |
| | Medium Sand (Class II) | Rich, uniform, pregnant | Quartz<br>K-Feldspar<br>Muscovite | 7<br>6<br>3 | Tourmaline<br>Zircon<br>Choloritoid | 7.5<br>7.5<br>6.5 | Kaolinite<br>Illite |
| Lower | Coarse Sand (Class I) Gravel, Silt, Clay | Rich but variable | Quartzite<br>Quartz<br>K-Feldspar | 7<br>7<br>6 | Garnet<br>Kyanite<br>Staurolite | 8<br>4.5-7<br>7.5 | Kaolinite<br>Illite |

### 2.1.3 Issues Presented for Operators

One of the major factors in determining wear of equipment is the ratio of wear protection material hardness ($H_M$) to the hardness of the abrasive media ($H_A$); the rate of wear decreases

significantly as the ratio $H_M/H_A$ is reduced below 1 (Llewellyn, Anderson, and Chiovelli, 2003). As can be seen in Table 2-1 above, heavy mineral hardness for materials in the oil sands ranges from 3 to 8 hardness on the Mohs scale, with the majority of minerals nearing 7 (1200Hv). Compared to a basic steel, with Vickers hardness of approximately 450-700 (Llewellyn et al., 2003), large amounts of wear would be expected, and thus it is no surprise that maintenance costs in commercial oil sands operations are extremely high.

## 2.2 Wear

In broad terms, wear is

"damage to a solid surface, generally involving progressive loss of material, due to relative motion between that surface and a contacting substance or substances" (ASTM, 2001).

As stated, wear generally does involve the progressive loss of material, but should not be limited to only situations where this occurs; damage can still occur through the displacement of material without any actual material loss. Wear can even occur even without any dimensional changes or material loss, such as the development of cracks in a lens or windshield (Bayer, 1994). It is important to realize that unlike other failure types, such as fatigue and fracture, there is no defined theory or model that unifies wear; it is not a material property, but rather a system property (Bayer, 1994).

This definition purposely encompasses a broad spectrum of processes; the one common aspect to all processes is relative movement of a surface and another substance. This motion can involve solids, liquids or gases, and can range from two solid surfaces sliding or rolling against each other, hard particles or liquids flowing against or impacting on a surface, to the collapse of cavitation bubbles within a liquid. In the mining industry, the term "material" is commonly used to refer to the substance/machine that is being abraded (shovel tooth, pump impeller, dozer blade), and "media" is typically used to describe the particles that are causing the abrasion.

The mechanisms by which wear occurs can be summarized as one of three broad types: mechanical, thermal or chemical. Kato, 2002, described these three main types as follows: mechanical wear as the loss or alteration of ductile material through deformation and brittle material through fracturing, chemical wear as the wear that is governed by the growth of a chemical reaction film (but not limited to situations with relative motion, and not including

purely corrosive environments), and thermal wear as the wear that occurs when frictional heating is enough to cause local surface melting. These terms only broadly describe the mechanism by which wear occurs, and should be further classified in order to accurately describe modes by which wear actually occurs.

### 2.2.1 Wear Modes

Mechanical wear can occur in a multitude of ways. When contacting bodies form an adhesive bond, resulting in production of wear particles, adhesive wear is said to occur (Stachowiak, 2013; Kato, 2002). Closely related to adhesive wear, flow wear occurs when plastic flow is the main type of deterioration (Kato, 2002).

Scratching of a softer surface by a harder particle or surface is termed abrasive wear, which can be particularly damaging (Stachowiak, 2013). Abrasive wear can be divided into two broad categories, “two-body” and “three-body”, Two-body wear occurs when particles that are constrained from movement abrade another surface (sandpaper on wood), and three-body wear occurs when particles are free to roll and slide down a surface (a excavator tooth digging through unconsolidated oil sand). Another type of wear closely related to abrasive wear is erosive wear, which occurs when hard particles impinge on a surface (Bayer, 1994).

Most contact between solid bodies will cause at least a small amount of wear; impact wear (also sometimes referred to as erosive wear) is another type caused simply by the impact between bodies (Stachowiak, 2013). Repetitive contact cycles can result in crack initiation and propagation, often through a combination of adhesive and impact wear, which results in different type of wear termed fatigue wear (Stachowiak, 2013; Kato, 2002). Another type of wear closely related to fatigue/impact/adhesive wear is fretting wear. This type of wear generally occurs as some combination of fatigue/impact/adhesive wear; however the difference between fretting wear and the other types of wear is the actual scale at which the motion occurs. In fretting wear, motion between contacting bodies is limited to very small distances, just a few micrometers (Stachowiak, 2013).

Any wear mode alters the surface of the materials involved and forms a thin layer of material. In the case of corrosive wear, this thin film is formed by a chemical attack on either contacting body, and is termed ‘tribofilm’ (Stachowiak, 2013; Kato, 2002). This tribofilm that forms is inevitably the subject of significant wear in several forms, all of which involve some form of tribofilm removal that resembles abrasive, adhesive or flow wear (Kato, 2002).

Thermal wear is a slightly less complicated, and is the result of high enough friction between contacts to raise the temperature to the melting point. This type of wear is termed melt wear, and when examined on the atomic scale can be termed diffusive wear. Diffusive wear does not normally result in significant volume losses; however the diffusion of particles from one surface to another can result in enhanced abrasive or adhesive wear (Kato, 2002).

#### *2.2.1.1 Abrasive Wear*

The major mode of interest to this work is abrasive wear. Abrasive wear is of particular interest to industry, as it has been estimated that as much as 50% of wear encountered in industrial situation is abrasive in form (Eyre, 1976). It is heavily dependent on hardness of material as well as the force load, making the ultra-class shovels digging in quartz-rich Athabasca oil sands an ideal candidate for abrasive wear.

Originally it was thought that abrasive wear was similar to the action of machine tools or a file on a surface; however research has shown that this simplified view only applies in rare occasions, and often is much more complicated than that (Stachowiak, 2013). Abrasive wear mechanisms can be generally classified into two broad categories by damage type: deformation or particle formation (Bayer, 1994). The actual mechanisms of abrasive wear are shown in Figure 2-1.

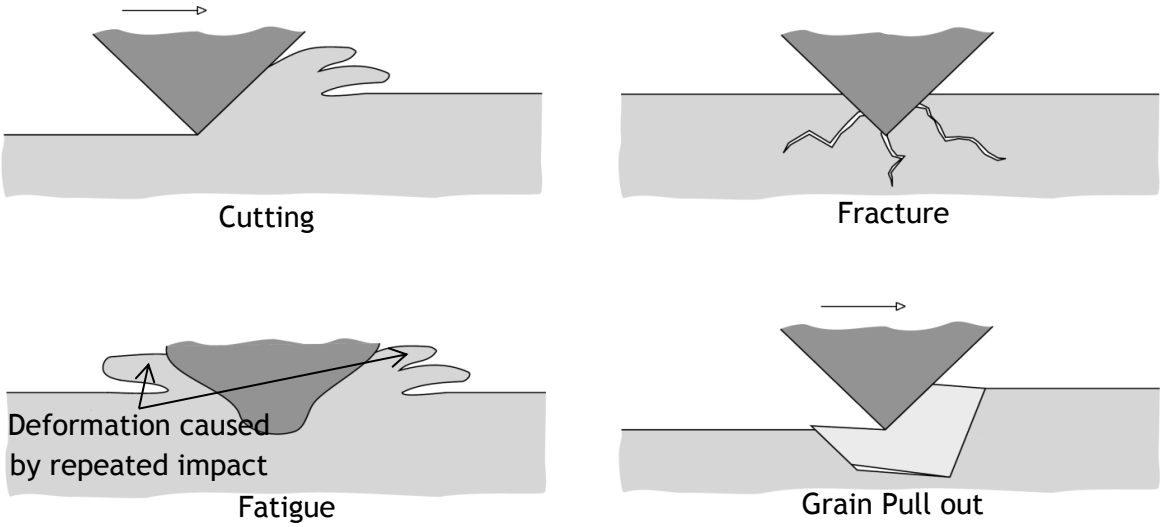


Figure 2-1: Mechanisms of Abrasive Wear (After Stachowiak, 2013)

Cutting represents the original school of thought, where a harder asperity scratches a softer surface and removes material. This was revealed by observation under an SEM to be caused by

two distinct mechanisms, ploughing and micro-cutting (Kayaba, 1986). Ploughing is the build-up of wear debris in front of the asperity, and micro-cutting is responsible for the removal of this build up as wear debris flakes.

Kayamba et al. (1986) further investigated the cutting mechanism and classified it into cutting, flaking, wedge and ploughing type wear. The differences are based on the type of wear debris created. Cutting will create a continuous microchip of ribbon like debris, flaking is similar to cutting but produces multiple flakes instead of one long continuous one, wedge type wear is characterized by the formation of a build-up of material in front of the contact, and ploughing is a negligible type of wear that involves the formation of a groove with ridges on both sides without causing much actual material loss (Kayaba, 1986). Ploughing and wedge type wear are very closely related, with wedge type wear referring to only the initial build-up of wear debris after contact, whereas ploughing refers to the continuous formation of a groove without any wear debris actually forming (Kayaba, 1986). The transition between these different types was found by SEM investigation to be based upon the penetration ratio of the abrasive (Kayaba, 1986).

Fracture wear will occur if the surface material is brittle, and usually is the result of crack convergence (Stachowiak, 2013). Fracture mechanisms dominate when the loads on abrasive grits are high, the grits themselves have sharp edges, and the fracture toughness to hardness of material ratio is low (Moore and King, 1980).

Fatigue wear is caused by repeated strains from a particle that causes the sideways deformation of the surface of a material. This is a milder form of abrasive wear, as repeated deformations are required to cause formation of wear particles (Stachowiak, 2013).

The final form of abrasive wear outlined by Stachowiak is “grain pull-out”. As the name implies, this type of wear occurs when failure along grain boundaries cause the grain to fall out, and is often associated with ceramic materials (Stachowiak, 2013). Carbide type materials are another common medium in which to find this mechanism of wear. The extremely hard carbide particles are held by a more ductile matrix material. This matrix material is preferentially worn, and once it reaches a certain point can no longer hold onto the carbide particles, which are pulled out.

### 2.2.2 Wear Modeling

Wear is not an intrinsic material property, but rather a reaction to a complicated system of conditions and as such is extraordinarily difficult to model accurately for several reasons (Hutchings, 2005). The process of wear alters the surface of the materials involved and forms a thin layer of material that separates the two sliding surfaces. This thin layer must be treated as a 'third-body' that is part of the system, and brings with it a new set of properties that can be quite variable (Berthier, 2005). The alteration of the surfaces not only forms a third-body but also changes the original topography continuously throughout the life of the system. The actual mechanisms by which wear occurs is also often a complex mix of mechanical, chemical and thermal processes that all work to change not only the surfaces, but also how destructive the other processes involved can be. The simple change from purely plastic deformation mechanism to fracture mechanisms can result in an increase of wear rate by ten times, and as such the proportion of each taking place is extremely important (Moore and King, 1980)

In the case of abrasive wear, which is the major focus of this work, chemical effects are usually minimal, but there are still the issues of modeling the deformation of the material, determining accurate ductile rupture or brittle fracture failure criteria, allowing for changes in surface topography, dealing with the inhomogeneity of the wear surface, as well as taking into account the individual interactions of particles with the wear surface (Hutchings, 2005). The individual interactions of particles itself is a large task; the bulk material characteristics of the material must be taken into account in addition to a full description of the particle shapes involved and variations in hardness (Hutchings, 2005).

One abrasive wear model sometimes used for analytical convenience simply assumes that abrasive wear can be treated as a combination of single conical asperities sliding across a surface. The wear volume is a function of the indentation hardness of the material, area of the abrasive asperity and sliding distance.

The load supported by the material being abraded is given as (Bayer, 1994):

$$W = H\frac{\pi r^2}{2} \qquad 2\text{-}1$$

Where W is the load supported by a single contact, H is indentation hardness (given as a unit of pressure) and r is the radius of the asperity, which can also be given by equation 2-2 (Bayer, 1994). A factor of ½ is used as only the leading edge of the asperity will make contact with the surface.

$$r = \frac{d}{\tan(90° - \theta)} \qquad 2\text{-}2$$

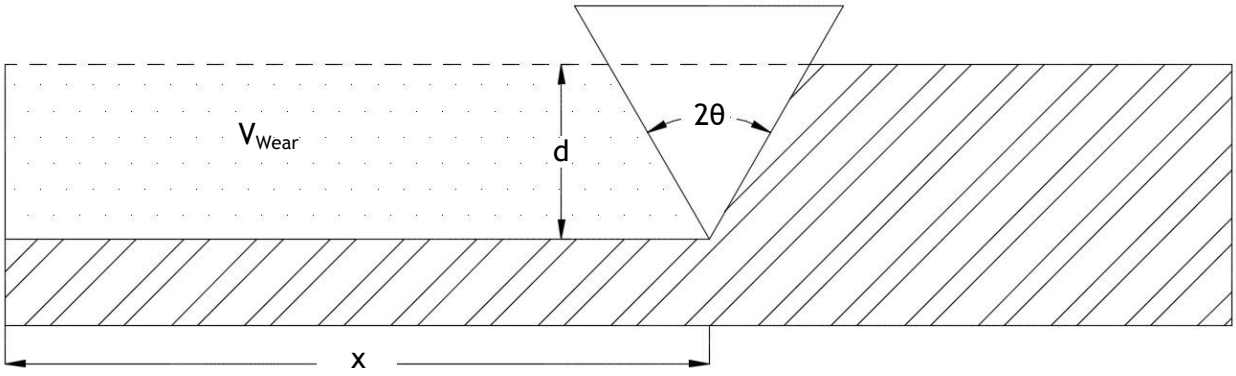


Figure 2-2: Abrasive Wear Model (after Bayer, 1994)

The total volume removal (V) can be treated simply as a function of the cross sectional area of the asperity and sliding distance, x (Bayer, 1994):

$$V = \tan(\theta)\, r^2 x \qquad 2\text{-}3$$

In this relationship, tan(θ) can be thought of as a sharpness of the abrasive material particles. Substituting equation 2-1 into 2-3 yields (Bayer, 1994):

$$V = \frac{2\tan(\theta)\, W}{\pi H} \qquad 2\text{-}4$$

The total wear is the sum of the individual asperities worn volumes. This formula however is only a simple model that does not take into account several realities. This relationship relies on all asperity/surface interactions being in the plastic deformation range, where as in reality many of the contacts will still be well in the elastic range, and therefore do not cause purely abrasive wear (Bayer, 1994). Also, this relationship relies on the assumption that the cross-sectional area of the asperity dictates the cross sectional area of the wear scar (Bayer, 1994). In reality, the wear groove may be significantly larger or smaller than the asperity, depending

on the material properties involved. These and other various factors can be taken into account through a dimensionless constant. This is illustrated by equation 2-5 (Bayer, 1994).

$$Q = \frac{KW}{H} \qquad 2\text{-}5$$

Where Q is the volume removed per unit sliding distance, W is the normal load, H is the indentation hardness of the surface, and K is a dimensionless constant normally referred to as the wear co-efficient. K can range from $10^{-2}$ in severe abrasive/erosive wear, down to $10^{-18}$ in some automotive applications (Neville and Morina, 2005).

In this highly simplified format, sliding wear can be considered to be directly proportional to the work done by friction. This relationship was likely first developed by Archard in 1953, though earlier work on the subject has been acknowledged, such as that done by Holm in 1946 (as referenced in Hutchings, 2005). Equation 2-5 is usually referred to as the Archard equation.

### 2.2.3 Influences on Wear Rates

Wear is a very complicated subject that usually involves multiple areas of science to explain a situation involving numerous random events. There are many influences on abrasive wear rates by grits but generally normal load, hardness of materials, speed of the relative motion between bodies, lubrication, and particle characteristics are considered to be the major influences. From the Archard equation (equation 2-5), as well as intuitively, it can be seen that normal load and hardness have an effect on abrasive wear rate. The speed of interactions between contacts follows from this; the more sliding distance covered in less time, the higher the wear rate. The relationship between wear rate and normal load/speed has been shown to be linear in nature (Hamblin and Stachowiak, 1996)

Lubrication and particle size have both been proven to have an effect, further examined in this section. The last normally cited major influence on wear rate is particle shape, specifically angularity, which is the major focus of this work.

When wear occurs of a sort that puts high stress on the abrasive particles, it is also important to examine media mechanical properties, such as fracture toughness, cleavage planes, etc, as these can greatly influence wear behaviour (Stachowiak, 2000). If as a particle fractures it greatly changes particle shape characteristics, it follows that abrasivity of the particles would likely change as well.

#### *2.2.3.1 Lubrication*

Lubrication is a factor can have a mixed effect on wear rate. Generally, the addition of a lubricant will decrease friction as well as wear rate, however this is not always the case. A lubricant can act to decrease the friction associated with adhesion, but at the same time provide a means to transport out wear particles that may normally clog surfaces up, thereby increasing abrasive wear (Bayer, 1994). This factor was not included as a major focus of this work, even though the presence of bitumen suggests this issue should be addressed. The rubber wheel abrasion test utilized in this work depends on the continuous and even flow of abrasive media, and would not have been able to function if oil sand with the bitumen fraction still present was used.

Dusseault and Morgenstern (1978) published a study on the physical properties of oil sands, in which they outlined two important characteristics that are of interest to this topic. The first characteristic is cohesion; oil sand has been shown in triaxial tests to have zero cohesion (Dusseault and Morgenstern, 1978). This is important as it suggests that there should be no adhesive wear caused by oil sands. The second characteristic is the fact that oil sand is "water-wet" (Dusseault and Morgenstern, 1978), and therefore interactions between media and material should not be as greatly influenced by the bitumen fraction.

Nonetheless, lubrication of the media/material interaction in the field may still play a large role, and its absence may have hampered the ability of the method used in this work to accurately predict field wear conditions. This subject may very well warrant further testing to be understood fully.

#### *2.2.3.2 Particle Size and the Particle Size Effect*

There is a well-defined relationship that exists between particle size and both two body and three body abrasive and erosive wear rate, as well as grinding and metal cutting; at particle sizes above 100μm, wear rate becomes essentially independent of particle size, and at less than 100 μm, wear rates tend to decrease steadily with decreasing particle size (Bayer, 1994; Misra and Finnie, 1981). The actual size at which wear rate becomes independent is somewhat variable; in testing done by Coronado, 2009, changes in the wear rate were seen up to abrasive sizes of 150-200 μm.

This particle size effect has been noted in many works (Graham and Baul, 1972; Coronado, 2009; Sasada, Oike, and Emori, 1984), and shown in theoretical models (Jacobson, Wallen,

and Hogmark, 1988) as well as been documented in erosion tests; with oil/sand slurries a definite correlation was seen between particle size and erosive wear rates (Clark, 1991).

Graham and Baul, 1972, using an impact test with a tool of known geometry to model the work of a single abrasive grit, showed a definite decrease in specific energy with an increase in tool size, showing that large particles abrade more efficiently than smaller ones. The argument they chose to use to explain this situation focused on the reduction in strength of a metal on the atomic level due to in-homogeneities such as grain boundaries and impurities, proposed by Backer et al, 1952. These defects are the source for the formation of chips, and as grit penetration decreases, the strength of a metal tends toward its theoretical value (Backer, Marshall, and Shaw, 1952)

Misra and Finnie (1981) published a comprehensive review of the possible causes of the size effect in abrasive and erosive wear. They examined or tested eleven different explanations that have been presented in various studies, and the only argument not discounted is the one shared with Backer et al., that the layer of material close to the surface exhibited a different flow stress than the bulk material (Misra and Finnie, 1981). Small particles were not able to penetrate through this layer; however larger ones did, and therefore exhibited a higher wear rate. Beyond whatever critical size is required to penetrate this layer, wear rates remained essentially steady. This size-strength effect was seen in micro-hardness indentation tests; measured hardness was increased by two to three times when indenters were reduced in size from 0.5mm to 0.2μm (Gane and Cox, 1970).

What the cause is of this flow stress gradient is not fully understood, but Misra and Finnie (1981) believe that it should be due to a material property, as it is seen in such a wide variety of situations. The best argument offered is that as abrasive microscopic deformation begins, the formation of dislocation tangles prevents the further movement of dislocations, forming a work-hardened surface layer (Misra and Finnie, 1981). This layer has been observed to range between 10-20μm thick (Misra and Finnie, 1981), and can be penetrated by larger particles, but not smaller ones, hence the phenomenon of a critical particle size.

De Pellegrin and Stachowiak (2004) came to a similar conclusion and believed that the main cause of the particle size effect is due to a scale dependent strengthening of materials as size is reduced.

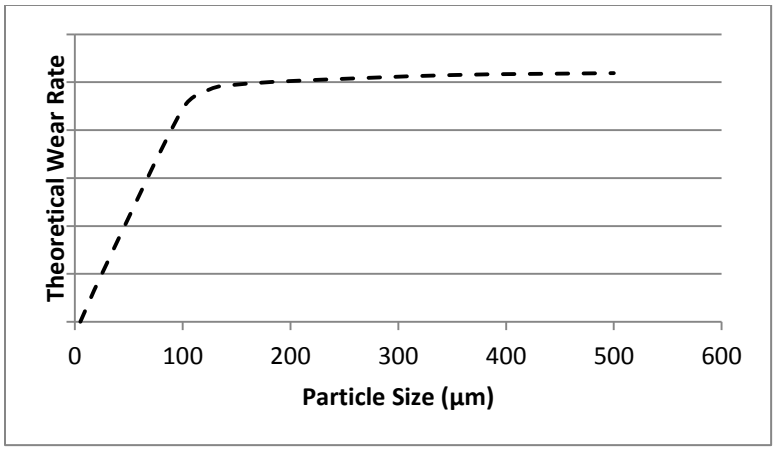


Figure 2-3: Particle Size Effect

#### *2.2.3.3 Hardness*

Hardness also intuitively has an effect on abrasivity; it has been studied extensively and shown that a harder material abrades more effectively than a softer one (Kulu, Tarbe, Kaerdi, and Goljandin, 2009; Levy and Chik, 1983; Torrance A.A., 1981; Hokkirigawa and Kato, 1988). For full abrasive cutting to occur the hardness of the abrasive material must be 20% greater than the hardness of the material being worn (Torrance A.A., 2005). If the ratio of material hardness to abrasive hardness is lower than 0.7,abrasive type wear such as micro-cutting and surface scratching will likely take place, however if this ratio is greater than 0.7, the wear process usually resembles some type of fatigue based wear (Kulu et al., 2009). Additionally, Kulu et al. found that for the extreme low end of abrasive material hardness, abrasive effectiveness approaches zero.

Levy and Chik (1983) explored the effects of hardness on erosion rate in their work, and found that above a certain abrasive hardness, wear rate was basically independent of particle hardness. In their study the erosive material hardness was approximately 4.5 times the hardness of the mild steel being tested before this effect was seen.

Clearly, any attempt to study field wear conditions should pay close attention to media and surface hardness ratio. In this work actual oil sand was used, which accurately models field conditions, as well as two other types of sand that share similar hardness to provide a basis for the angularity analysis. These elements are covered further in Chapter 4.

#### *2.2.3.4 Particle Shape*

Particle shape tends to have a more modest effect on wear rates than the other factors (De Pellegrin and Stachowiak, 2002). There are two broad types of methods to determine aggregate particle shape characteristics, indirect and direct. Indirect methods use the measurement of bulk properties to infer particle characteristics, through tests such as direct shear or uncompacted void content of aggregates tests, among others (Rousan, 2004). Direct methods measure, describe qualitatively, and sometimes quantify through direct methods, particle shape characteristics (Kandhal, Motter, and Khatri, 1991). Image analysis is a common method for this type of test, and has been focused on in this work, more information on the other types of tests can be found in Kandhal et al. (1991) and Janoo (1998).

Shape parameters generally describe the deviation of a particle from an ideal standard such as a circle or ellipse (De Pellegrin and Stachowiak, 2002). It has widely been accepted that particle shape can accurately be described by three different parameters: form, angularity/roundness, and surface texture (Wadell, 1932; Barrett, 1980). Form refers to the overall shape of the particle, angularity/roundness describes the shape of apexes and corners of particles that fit within the overall form, and surface texture refers to the small scale variations in the surface of a particle that have no effect on the overall shape of the particle (Barrett, 1980). Surface texture can also be considered proportional to the roughness of the surfaces of media and abraded metal or material. Therefore, the surface friction of the interaction between abrasive media particles themselves, or between particles and the surface of the material being abraded can be considered proportional to texture.

Of these main types, angularity is of particular interest to geologists and engineers. It is widely used as a measure of how far a particle has been fluvially transported, it is extremely important when discussing abrasivity of a material, as well as being important in the prediction of construction aggregate performance (Masad, Al-Rousan, Button, and Little, 2007; Tafesse, Fernlund, Sun, and Bergholm, 2013). In particular, high angularity in fine aggregates has been shown to have an important influence on shear strength, and therefore resistance to rutting of pavement mixtures (Masad, Olcott, White, and Tashman, 2001; Masad et al., 2007). Any measure of particle abrasivity must also include an analysis of particle angularity, as this is the largest factor in increasing micro-cutting and therefore wear rate (Hamblin and Stachowiak, 1996). It is intuitive and has been proven in multiple studies that angular particles produce much more rapid wear rates than rounded ones (Mulhear and Samuels, 1962; Stachowiak, 2000; Stachowiak, 2005; Hamblin and Stachowiak, 1995; Levy and

Chik, 1983; Clark, 1991). As such, it might be reasonably expected that more angular particles would produce troughed or grooved wear scars rather than a uniform abrasion of the surface.

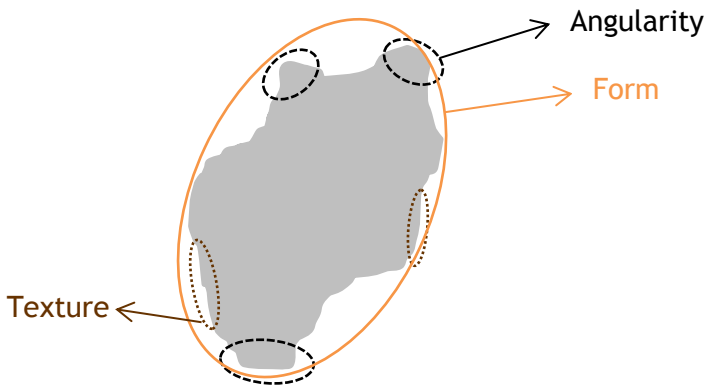


Figure 2-4: Particle Shape Characteristics (after Barrett, 1980)

This work focused on utilizing particle analysis as a method of determining potential abrasivity, and therefore prediction of contact tool performance in the mining industry. However, particle analysis has many other uses; it has already been covered that analysis of shape can be used to predict performance of aggregates in construction applications, as well as predict the wear inducing capabilities of aggregate. Additionally, particle analysis can perform another important function in diagnosis of machine health. By examining wear particles produced internally by machines, a better understanding of the wear processes that may be present in a system can be gained, and therefore the appropriate plan of action to deal with reducing this wear (Stachowiak, 1998). Adhesive, abrasive and fatigue wear are the most common types of wear encountered in industry, and by examining wear particle morphology, differences can be used to determine type of wear occurring within a machine (Stachowiak, Stachowiak, and Podsiadlo, 2008). Work has been done on the automation of this system to classify particles based on their morphology through the use of fractals and wavelets, through which particles may be assigned to a specific class based on wear process, surface morphology, etc (Stachowiak and Podsiadlo, 2006; 2001)

#### *2.2.3.5 Image Analysis*

The advent of computer software and digital imaging abilities has led to the development of many methods that attempt to quantify shape of particles. However, these methods must be applied carefully, as often the different methods bring with them different classification

results on the same samples (Tafesse et al., 2013; Al-Rousan, Masad, Tutumluer, and Pan, 2007).

It has been specified that in image analysis, images obtained should have a resolution of at least 100 pixels in the direction of the smallest particle diameter for angularity analysis, in order to properly obtain the resolution required to accurately differentiate the form from angularity, and angularity from texture (Masad and Button, 2000; Fletcher, Chandan, Masad, and Sivakumar, 2002; Masad et al., 2001).

The basic idea behind particle shape analysis is to combine various measurements of particle dimension in ways that eliminate units; commonly used dimensions include area, perimeter, ferret diameters and coordinates (Kuo and Freeman, 2000). A good particle shape parameter should be scale independent and also accurately describe geometrical properties (Hamblin and Stachowiak, 1995). Area is the number of picture pixels that the particle itself inhabits, and is often used to determine an equivalent circle, which is a perfect circle which contains the same area as the particle itself. This concept can be extended to the equivalent ellipsoid, which is an ellipsoid with the same area as well as major and minor axis dimensions as the actual particle. The diameters as well as perimeters of these equivalent shapes are used in the calculation of some factors. Perimeter is the number of pixels that the boundary of the particle occupies, and can be related to equivalent circle or ellipsoid perimeters for comparison against idealized shapes. Ferret diameters are measurements made between two parallel tangent lines, the use of which can determine overall particle linear dimensions. This concept is illustrated in Figure 2-5.

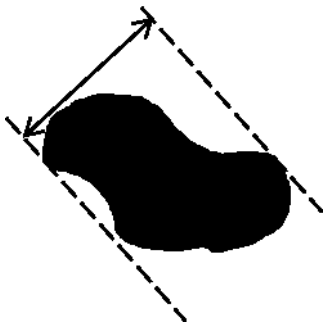

Figure 2-5: Ferret Diameter (after Kuo and Freeman, 2000)

Another concept used in particle analysis is the convex polygon. The easiest way to picture a convex polygon is to imagine an elastic band stretched around the particle, the area encompassed by the elastic band would be the convex polygon. This is illustrated in Figure 2-6. The convex polygon is considered to be an accurate way to model particle shape without

influence from surface texture (Kuo and Freeman, 2000). A convex polygon with 32 or more sides is generally considered a good approximation of overall form (Russ, 1995).

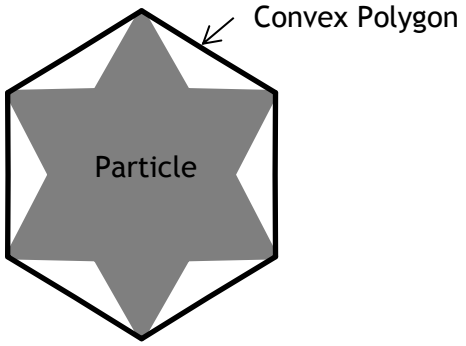


Figure 2-6: Convex Polygon (after Kuo and Freeman, 2000)

#### *2.2.3.6 Particle Shape Parameters*

Traditionally, particle shapes have been assigned subjective, visual type measurements such as “very angular”, “sub-angular”, or “rounded”. There has been a large amount of effort made towards the quantification of particle shape, a selection of these are examined in this section.

##### 2.2.3.6.1 Form

###### *2.2.3.6.1.1 Form Factor:*

Form factor is a widely used parameter to describe the overall form of a particle (Masad et al., 2001; Kuo and Freeman, 2000). It compares the perimeter of a circle with the same area as the particle, to the true perimeter of the particle. The calculation for form factor is shown in equation 2-6 (Masad et al., 2001; Kuo and Freeman, 2000).

$$Form\ Factor = \frac{4\pi A}{P^2} \qquad 2\text{-}6$$

Where A is the area of the particle and P is the perimeter of the particle. As texture and angularity both affect perimeter and area, it can be seen that form factor is not only a measure of the overall form, but also the angularity and texture (Masad et al., 2001; Kuo and Freeman, 2000). Form factor would be equal to one for a circle, and less than one for increasingly “un-circular” objects. This parameter is also sometimes adapted to a different form, known as “Roundness”, which is simply the inverse of form factor (Al-Rousan et al.,

2007). This change results in the roundness factor being equal to 1 for a circle, and greater than one for increasingly "un-circular" objects.

Form factor was shown to have a good correlation with two-body abrasive wear in a test by Hamblin and Stachowiak, 1995. However, they also noticed some issues with the parameter when applying it to images gathered on a scanning electron microsope. They found that a small adjustment in focus resulted in a 20% decrease in the form factor, due to the significant effect on perimeter when dealing with pixel level measurements.

#### *2.2.3.6.1.2 Form Index*

Form index is another parameter used to describe overall form (Masad et al., 2001). It utilizes the change in radius through a 5° increment along the particle boundary to describe form, as shown in equation 2-7 (Masad et al., 2001).

$$Form\ Index = \sum_{\theta=0}^{355} \frac{|R_{\theta+5} - R_{\theta}|}{R_{\theta}} \qquad 2\text{-}7$$

Where $R_{\theta+5}$ is the radius of the particle 5° ahead of the current position, and $R_{\theta}$ is the radius at the current position. The 5° increment was chosen to differentiate form index from angularity measurements, as it was found that most angularity type differences in a particle occur at a scale less than that (Masad et al., 2001). It has been shown that form index is indeed an accurate descriptor of particle form, without being influenced by angularity (Masad et al., 2001)

### 2.2.3.6.2 Angularity

#### *2.2.3.6.2.1 Angularity Index*

Masad et al, 2001 developed the angularity index as a method to determine angularity based on the radius of a particle. It is based on the difference between the actual particle and an equivalent ellipsoid that shares the same major and minor axes as the particle, but does not have any angularity. Radii are compared for every five degree increment around the particle. The equation for angularity index is shown in equation 2-8 (Masad et al., 2001).

$$AI = \sum_{\theta=0}^{355} \frac{|R_\theta - R_{EE\theta}|}{R_{EE\theta}} \quad \text{2-8}$$

Where $R_{EE\theta}$ is the equivalent ellipsoid radius at angle θ, and $R_\theta$ is the radius of the particle at that same angle. Therefore, for a circle or ellipse, angularity index would be equal to zero, and would increase for increasing angularity. It was shown that angularity index is an accurate descriptor of particle angularity, without being influenced by overall particle form (Masad et al., 2001)

*2.2.3.6.2.2 Convexity*

Convexity is another parameter that has been used to describe the angularity of particles (Al Rousan, 2004). It is based on the relationship between area of the particle, and the area of a convex polygon. The relationship is illustrated in equation 2-9 (Al Rousan, 2004)

$$Convexity = \sqrt{\frac{A_{Particle}}{A_{Convex}}} \quad \text{2-9}$$

Where $A_{Particle}$ refers to the area of the actual particle being analyzed, and $A_{Convex}$ is the area of the convex polygon surrounding the particle. Thus, a perfectly circular or perfectly square shape would both have a convexity of one, where as a star or spikey shape would be less than one, tending towards zero.

*2.2.3.6.2.3 Angularity Parameter:*

The "angularity parameter" was first proposed by Kuo and Freeman (2000) and utilizes the area of an equivalent ellipsoid and the bounding convex polygon. The relationship is shown in equation 2-10 (Kuo and Freeman, 2000).

$$Angularity\ Parameter = \left(\frac{P_{Convex}}{P_{Ellipse}}\right)^2 \quad \text{2-10}$$

Where $P_{Convex}$ is the perimeter of the convex bounding polygon, and $P_{Ellipse}$ is the perimeter of an equivalent ellipsoid (same area and aspect ratio as actual particle). Therefore, a perfect circle or ellipse would have an angularity parameter of one, and with increasing "spikiness", angularity parameter would continue to rise above one. Kuo and Freeman, 2000, believe this parameter excludes the influence of aspect ratio as well as surface texture and accurately measures angularity alone.

*2.2.3.6.2.4 Spike Parameter*

The spike parameter was first introduced by Hamblin and Stachowiak, 1995. This parameter is based on the representation of a particle boundary by a series of triangles, and was developed from the "Richardson Technique" used for boundary fractal dimensions (Hamblin and Stachowiak, 1995). The boundary of a particle is "stepped around" at set intervals, and a point on the actual particle boundary between steps forms the top of the triangle. This method is illustrated in Figure 2-7

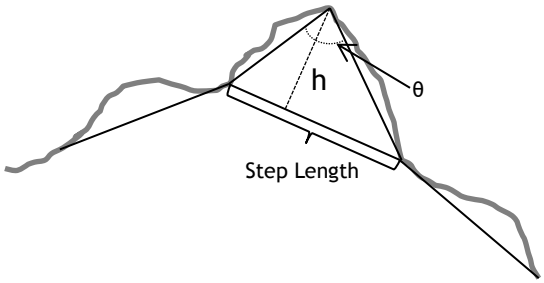


Figure 2-7: Spike Parameter (after Hamblin and Stachowiak, 1995)

As the triangles become taller (h), as well as sharper (θ), their relative abrasivity is increased. The spike value is the measure of this relative abrasivity and is defined in equation 2-11 (Hamblin and Stachowiak, 1995).

$$Spike\ Value = \cos\left(\frac{\theta}{2}\right) * h \qquad 2\text{-}11$$

Each step on the particle boundary with a valid triangle formed is examined to determine the maximum spike value for that step. After computing the spike values for each step, the whole process is repeated for each valid starting point. The maximum calculated spike values for each step size are averaged, and the entire process is repeated using a different step size. In Stachowiak's original work (1995), the initial step size used was 40 pixels, and was increased by 10 pixels until the step size reached 1/15$^{th}$ the size of the entire particle boundary. Using these maximum spike values, the "spike parameter" is calculated as follows (Hamblin and Stachowiak, 1995):

$$Spike\ Parameter = \frac{\sum\left[\sum \frac{sv_{max}}{h_{max}}\right]/m}{n} \qquad 2\text{-}12$$

Where $sv_{max}$ is the largest spike value for each valid triangle formed, $h_{max}$ is the associated maximum height of the triangle, m is the number of valid triangles for a given step size, and n is the number of step sizes used.

One of the benefits to this method over the fractal method is the ability to discount insignificant boundary features. Hamblin and Stachowiak (1995) suggested that if a triangle had an angle greater than 2.9 radians, it should be assigned a spike value of zero, which eliminated very shallow protrusions that are unlikely to come into contact with another surface.

The spike parameter has been used in several studies of abrasivity, and generally shows very good correlation with wear rates (Hamblin and Stachowiak, 1995; Stachowiak, 2000; Hamblin and Stachowiak, 1995; Stachowiak, 1998)

However, this parameter does has several shortcomings: it is very sensitive to focus/image quality and can assign false spike values due to this, underestimation of the true boundary spike angle can occur with convex shapes, and finally it is a computational intensive measurement, requiring many triangles to be analyzed for each particle (Stachowiak, 2000)

*2.2.3.6.2.5 Spike Parameter, Quadratic Fit*

While the spike parameter offers a better measure of abrasivity than the Richardson plot fractal method, it is still a slightly flawed system. Hamblin and Stachowiak (1996) introduced a refinement to this method that solved many of these issues, known as spike parameter, quadratic fit (SPQ).

This method utilized the centroid of the particle, as well as the equivalent circle to determine which particle protrusions warrant being included in calculations. The method begins with the calculation of the centroid of the particle, which the equivalent circle is centered on. Any point on the actual particle that falls outside the equivalent circle is deemed significant enough to be included in calculations.

For each area falling outside of the equivalent circle, the maximum radius point is found, which forms the middle point, similar to the original spike parameter. A quadratic polynomial is fitted from the middle point to the start and end point (determined in a similar way to the spike parameter, where the particle boundary crosses the equivalent circle boundary). Differentiating the curves at the middle point yields the apex angle, which is used to

calculate the spike value, quadratic fit, as shown in equation 2-13 (Hamblin and Stachowiak, 1996)

$$Spike\ Value, Quadratic\ Fit = \cos\left(\frac{\theta}{2}\right) \quad 2\text{-}13$$

SPQ is calculated as the average of spike values for all protrusions. The method is shown in Figure 2-8.

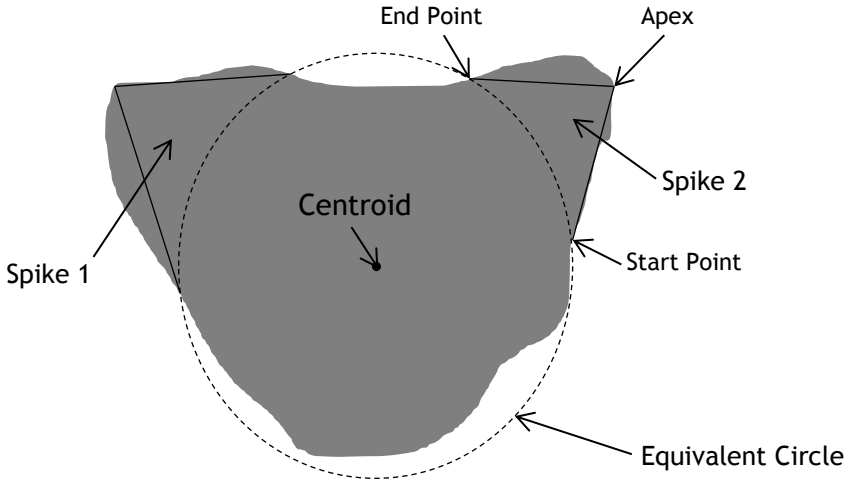


Figure 2-8: Spike Parameter, Quadratic Fit Method (after Hamblin and Stachowiak, 1996)

SPQ has the advantage over spike parameter in the ability to only consider corners of the particle that are likely to have an influence on abrasive wear, and discount unimportant features; although the mean diameter is an arbitrary choice, it is nevertheless effective (De Pellegrin and Stachowiak, 2002; Hamblin and Stachowiak, 1996). This is in contrast to the fractal (Kaye, 1984) or Fourier (Swanson and Vetter, 1985) methods, which both include insignificant features (De Pellegrin and Stachowiak, 2002)

It is also nearly insensitive to image focussing, with a less than 4% change compared to upwards of 20% for other shape factors at the same level of defocussing (Hamblin and Stachowiak, 1996)

This parameter has been applied in testing by Stachowiak (1995, 1998, 2000) and Kulu et al. (2009), among others, and has shown excellent correlation with abrasive wear. Stachowiak

(2000) found that it correlated better than the original spike parameter in his comparison of the two.

The SPQ parameter can also be extended to analyze surfaces, rather than particles. When examining the cross section of a surface, even the flattest and smoothest surfaces will eventually display some relief at a high enough magnification. The ridges and grooves that appear can be treated the same way as particle asperities. Jankuaskas and Kreivaitis (2007) used this method, and applied the SPQ procedure to all ridges on the cross section that showed at least 25% of the maximum height of surface. They found good (76-89%) correlation between wear rates and $SPQ_{Surface}$ parameter. Stachowiak (1998) also demonstrated the use of the SPQ parameter to describe surface roughness.

Kulu et al applied the SPQ to a study of erosion and grindability of mineral ores, and found good correlation with the wear rates of commercial steels as well as metal matrix composites. However, they found that when testing cermets, erosion did not depend as closely on particle shape. They also found that other material properties such as fracture toughness and homogeneity can play a large role in erosion and grindability.

#### 2.2.3.6.3 Texture

Masad et al., 2001, 2007; Rousan, 2004; and Little et al., 2003, all used a method to determine texture that is based on analysis of grey scale images. In a grey scale image, all pixels are assigned an intensity value from 0-255 (0 is black, 255 is white) that refers to the brightness of that pixel. By analysing the distribution of pixel intensity, a measure of texture can be determined; a larger standard of deviation of intensity within a particle refers to a rougher surface.

It has been noted by Rousan, 2004, that lighting plays an important role in image quality and determination of particle characteristics. It was found that extreme levels of brightness or darkness, surface texture values could vary significantly even when testing the same particle. It was found that maintaining a mean pixel brightness value within a particle of between 110 and 170 obtained the most accurate texture results.

It is intuitive that natural color variations within a particle would affect texture measurements when using the grey scale intensity method. However, a study by Fletcher et al. found that due to the small size of particles when fine aggregates are analyzed, color variations occur on a scale that should have little to no effect on overall texture

measurement (Fletcher et al., 2002). This conclusion appears to agree with the images used in this work for texture analysis, upon visual inspection.

Typically, black and white or grey scale images are used for texture analysis. Black and white photos require very high resolution and are not suitable for automated systems, as well as typically having less texture specific detail (Al-Rousan et al., 2007). Grey scale images can analyze more texture specific details, but those details are sometimes influenced by natural variations within the coloring of the particle (Al-Rousan et al., 2007).

##### *2.2.3.6.3.1 Angle of Repose as a Measure of Texture*

The use of the standard deviation of intensity method in this work to determine texture was a laborious task to complete, and can be prone to error based on image quality. Part of this work has focussed on a new method that will hopefully allow for much easier measurements of texture, one that utilizes the angle of repose. Angle of repose is a physical trait inherent to every aggregate material. The angle of repose for a material is dependent on the ability of the particles to create a pile, and as such is highly correlated with the surface friction properties of particles. It is believed by the author that particle texture is the largest driving factor behind the friction response of particles, and therefore texture should closely correlate with angle of repose.

### 2.2.4 Wear Resistant Materials

As discussed in section 2.1.3, operators in northern Alberta oil sands mines face significant issues with wear related issues, which can cause significant economic harm. The loss of even 2% of production at Syncrude would result in a revenue loss of around $40M (Canadian Oil Sands, 2013). From a $1.6B operating expense budget, Syncrude Canada dedicated $983M to regular maintenance in 2014 (Canadian Oil Sands, 2013). It is possible to achieve a significant decrease of these maintenance costs via the use of surface engineering. With the application of surface overlays, desirable characteristics of the bulk material used in production of a part can be preserved, while improving the wear and corrosion resistance of the surfaces in contact with oil sand (Fisher, Wolfe, and Meszaros, 2013).

Many options exist to oil sand producers to reduce the effects of wear through surface engineering including (from Harper, Gill, Hart, and Anderson, 2002):

- Welded Overlays
- Casting and Foundry Technologies
- Heat Treatment/CVD/PVD Processes
- Thermal Spray Coatings

- Brazed Overlays
- Electro-Mechanical Plating

Of these methods, welded overlays and casting technologies are the most commonly used. Welded overlays can be applied through many process including: rod and powder brazing, flux-cored arc welding, oxy fuel welding, shielded metal arc welding, gas metal arc welding (GMAW) and plasma transferred arc welding (PTAW), which is generally regarded as the most effective and economical method (Harper, Gill, Hart, and Anderson, 2002; Llewellyn, Anderson, and Chiovelli, 2003). Weld overlays have several characteristics that are desirable (from Llewellyn, 1996):

- Tough, weldable and lower cost base materials can be used
- Complex shapes can be manufactured
- Areas susceptible to attack can be protected selectively
- Worn components can be repaired more easily
- Extremely wear resistant materials that cannot be reliably cast or forged can be used

Four common classes of metallic materials exist to combat wear: iron based alloys, nickel based alloys, cobalt based alloys, and carbide containing composites (McKee and Wu, 1997). Additionally, cermet materials, a combination of ceramic/metallic alloys, exist and have found some applications, especially high temperature ones (Llewellyn and Tuite, 1995).

In terms of abrasion resistance, material hardness of both the matrix and hard phase material is the important factor, specifically that the $H_A/H_M$ ratio discussed above (section 2.1.3) remains below 1. At high temperatures, several new factors come into effect. If the matrix material cannot handle exposure to higher temperatures, the hard phase particles become inconsequential to wear resistance as they can fail out of the matrix rather than provide any effective wear protection (Winkelmann et al., 2009).

For equipment protection purposes in the oil sands, where traditional materials would be inadequate, carbide containing composites are the most common. Generally speaking, these materials are composed of a ductile matrix material which contains much harder particles embedded within it. Metal matrix composites (MMC) are a common term used to describe these carbide containing deposits (Yarmuch, Patchett, Ivey, and Anderson, 2009). For surface wear protection in oil sands production critical components, where maximum wear protection is required, most MMC's are composed of a matrix material of NiCrBSi or NiBSi, with 60 wt% tungsten carbide particles making up the hard phase (Yarmuch, Patchett, Ivey, and Anderson,

2009; Fisher, Wolfe, and Meszaros, 2013). Chromium may also be added up to 15wt% to augment the matrix strength through the formation of chrome-borides and chrome-carbides, however this may not improve overall performance as the presence of chrome accelerates the dissolution of the superior tungsten carbides (Fisher, Wolfe, Yarmuch, Gerlich, and Mendez, 2011).

Tungsten carbide hard facing is typically used for production critical components due to its increased wear resistance versus chrome carbide, which is usually used in high volume applications due to its relatively inexpensive cost (Harper, Gill, Hart, and Anderson, 2002). The hardness of the matrix material that holds the carbides ranges from 300-700 Hv, hardness for the carbides ranges from 1600-2000 Hv for the tungsten carbide, and is approximately 1700 Hv for the chrome carbide (Yarmuch, Patchett, Ivey, and Anderson, 2009; Fisher et al., 2011).

### 2.2.5 Samples Used in This Work

The samples that formed the basis for this work are a chrome carbide overlay, welded using submerged arc methods, and have graciously been provided by Wilkinson Steel and Metals in Edmonton, Alberta. They are created with powder additions, rather than metal cored wire. A base plate of 0.313" thickness is used, that after the welding process forms a ¼" chrome carbide on ¼" base sample. Sample hardness is approximately 500 Hv, as this is a hypoeutectic sample, which is often used in a thin sample such as the ones utilized in this work.

Figure 2-9 is an image of the chrome carbide samples used in this work, and was collected using a scanning electron microscope. It shows the distribution of the actual carbides (darker grey portions) among the matrix material (lighter grey portions). The harder carbides provide the greatest amount of wear resistance, whereas the softer matrix material is expected to be preferentially worn.

In the testing done for this work, the granite sand abrasive media has a fairly significant portion of its particle size distribution that falls below 100 μm, including many particles that are smaller than 10 μm. From figure Figure 2-9, it can be seen that the spacing of the carbide particles can be up to 10-15 μm in certain areas. When abrasive media particles are smaller than the mean spacing between carbides, they can be preferentially funneled against the softer matrix material and therefore greatly increase the preferential wear of the matrix

material (Fisher et al., 2013). All of the sand samples tested were expected to cause some preferential wear of the matrix material, with the granite sand expected to cause the most.

This phenomenon is of particular interest to any industry that involves the comminution of rock. When rock particles are broken down, there will always be extremely small particles that are formed. These small particles, depending on mechanical properties of the mineral constituents, may likely form very jagged edges and be particularly abrasive. In situations such as this, with extremely small and rough particles, proper carbide distribution becomes especially important to avoid much faster preferential wear of the matrix material.

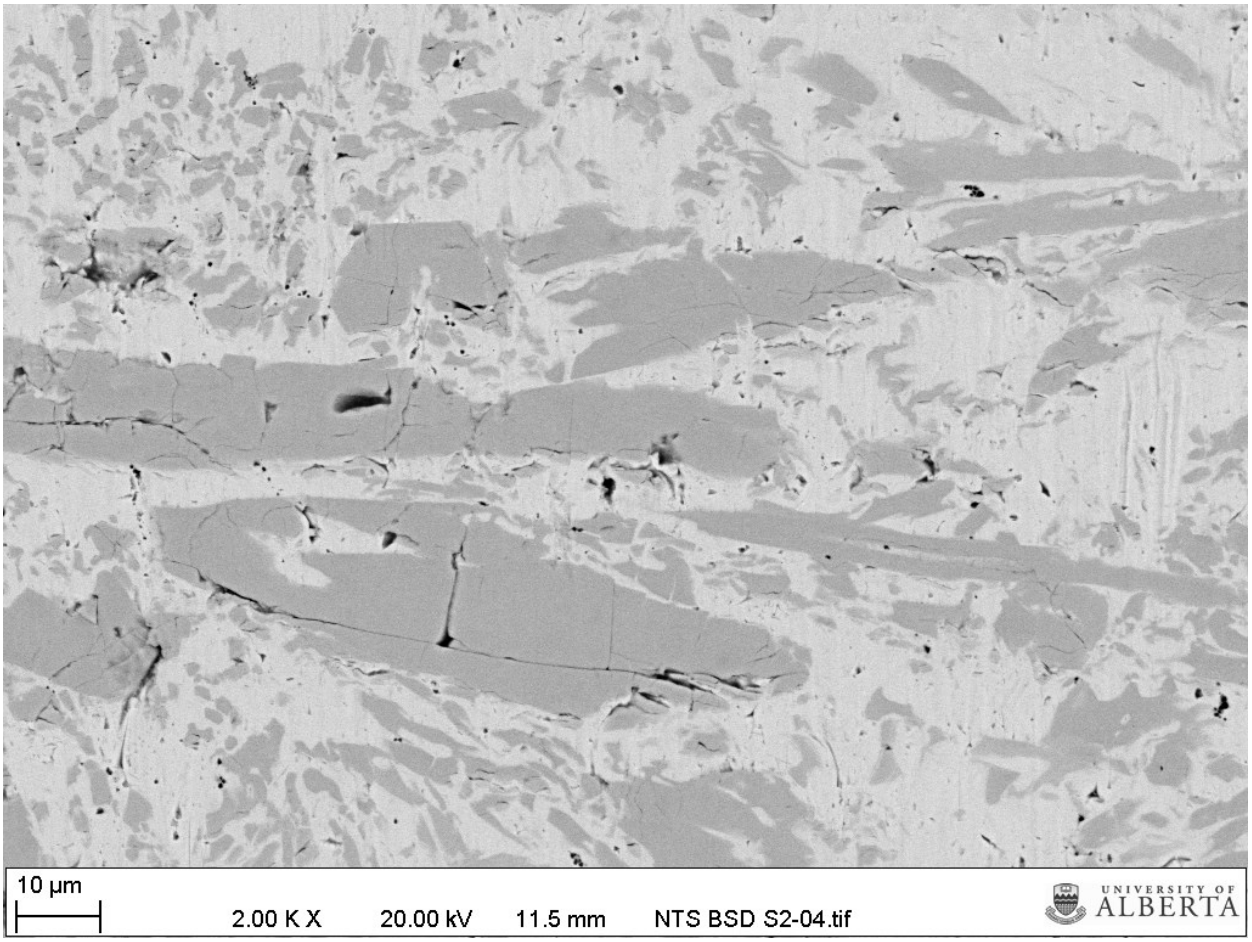


Figure 2-9: Chrome Carbide Sample

# 3 Cable Shovel Geometry

## 3.1 Introduction

In the Athabasca Oil sands the truck-and-shovel method is the main one employed for earth moving; in particular ultra-class cable shovels are used extensively. They are more flexible and reliable than many other systems, while at the same time offering one of the best unit production cost available.

There are three basic parts to a cable shovel, the upper, lower, and attachment. The digging motion of the excavator is accomplished through the use of the hoist rope and crowd mechanism. The crowd mechanism is responsible for the forward and rearward movement of the dipper handle through the saddle block, which positions the dipper for a digging cycle, and the hoist provides the massive force used to actually pull the dipper through a dig face.

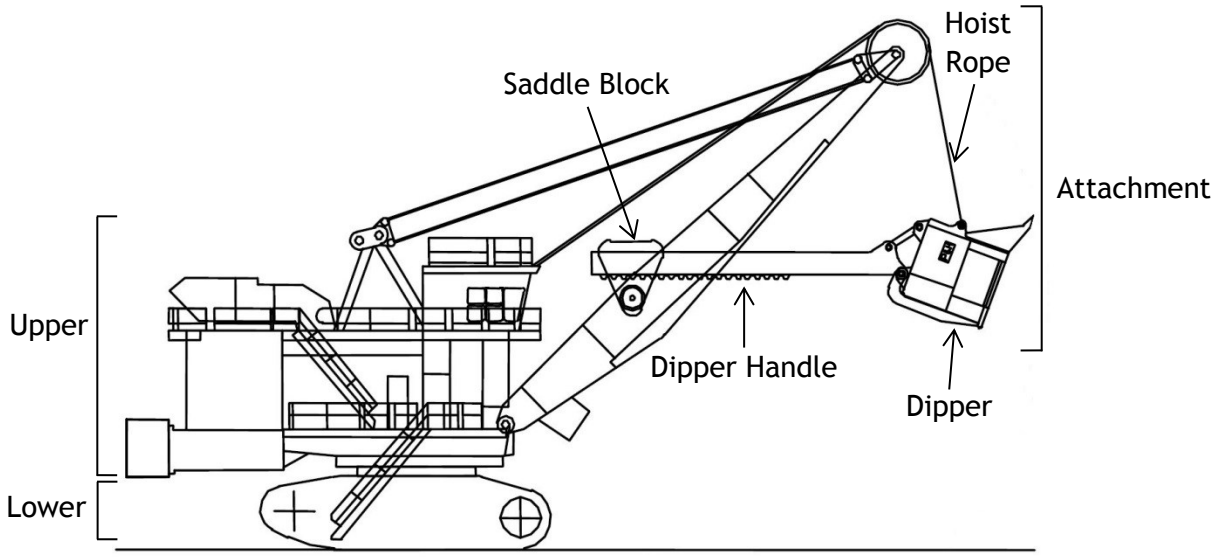


Figure 3-1: Cable Shovel Diagram (adapted from Joseph and Shi, 2011; Darling, 2011)

## 3.2 Dipper/Handle Kinematics

Joseph and Shi (2011) presented a complete consideration of the hoist and crowd motion to define the kinematics of shovel operation; the same method has been used in this work to facilitate force calculations and determine shovel bucket trajectory.

Data obtained from a P&H 4100 BOSS shovel working in the oil sands was used for calculations. The data contained information on hoist cable length, crowd extension, as well as hoist and crowd current and voltage, all of which were used in this work. An example of the data is shown in Table 3-1.

Table 3-1: Shovel Field Data

| Time (s) | Hoist Length (m) | Crowd Length (m) | Hoist v (m/s) | Crowd v (m/s) | Hoist Armature Current (A) | Crowd Armature Current (A) | Hoist Armature Voltage (V) | Crowd Armature Voltage (V) |
|---|---|---|---|---|---|---|---|---|
| 0.0 | 3.9886 | 5.5444 | 0 | 0.012991 | 865 | -46 | -4 | 12 |
| 0.1 | 3.9886 | 5.5444 | 0 | 0.012991 | 864 | -102 | 0 | 11 |
| 0.2 | 3.9886 | 5.5457 | 0 | 0.012991 | 858 | -52 | 0 | 9 |
| 0.3 | 3.9886 | 5.5483 | 0 | 0.012991 | 873 | -112 | 1 | 9 |
| 0.4 | 3.9937 | 5.5483 | 0 | 0 | 849 | -59 | 1 | 7 |
| 0.5 | 3.9937 | 5.5496 | 0 | 0 | 867 | -111 | 4 | 6 |
| 0.6 | 3.9937 | 5.5496 | 0 | 0 | 827 | -43 | 7 | 6 |
| 0.7 | 3.9937 | 5.5496 | 0 | 0 | 881 | -49 | 3 | 0 |
| 0.8 | 3.9937 | 5.5496 | 0 | 0 | 813 | -50 | 5 | 3 |
| 0.9 | 3.9937 | 5.5509 | 0 | 0 | 837 | -58 | 4 | 2 |
| 1.0 | 3.9937 | 5.5509 | 0 | 0 | 820 | -60 | 2 | 3 |
| … | … | … | … | … | … | … | … | … |
| 24.0 | 11.201 | 4.834 | -1.0043 | 0.42869 | 1951 | 954 | 529 | 402 |
| 24.1 | 11.106 | 4.8767 | -1.0043 | 0.5586 | 2773 | 1040 | 537 | 432 |
| 24.2 | 11.009 | 4.9129 | -0.97852 | 0.45468 | 2839 | 1014 | 564 | 464 |
| 24.3 | 10.909 | 4.9725 | -1.0043 | 0.54561 | 2986 | 1005 | 589 | 490 |
| 24.4 | 10.801 | 5.0281 | -1.0558 | 0.5586 | 2766 | 1020 | 573 | 514 |
| 24.5 | 10.706 | 5.0734 | -1.0558 | 0.5586 | 2604 | 1051 | 578 | 554 |
| 24.6 | 10.601 | 5.1277 | -1.0558 | 0.59757 | 2176 | 998 | 578 | 555 |
| 24.7 | 10.488 | 5.1873 | -1.0558 | 0.59757 | 1771 | 954 | 575 | 544 |
| 24.8 | 10.393 | 5.2481 | -1.0815 | 0.61057 | 1963 | 827 | 556 | 547 |
| 24.9 | 10.247 | 5.3387 | -1.0815 | 0.61057 | 2439 | 730 | 577 | 562 |
| 25.0 | 10.15 | 5.3982 | -1.0815 | 0.61057 | 2787 | 656 | 604 | 554 |

The crowd length and hoist length data recorded does not reflect the true dimension associated with these measurements, the “linkage” for each needed to also be added in. With these taken into account, a triangular relationship was established between bail point, sheave center and the saddle block center, as shown in Figure 3-2.

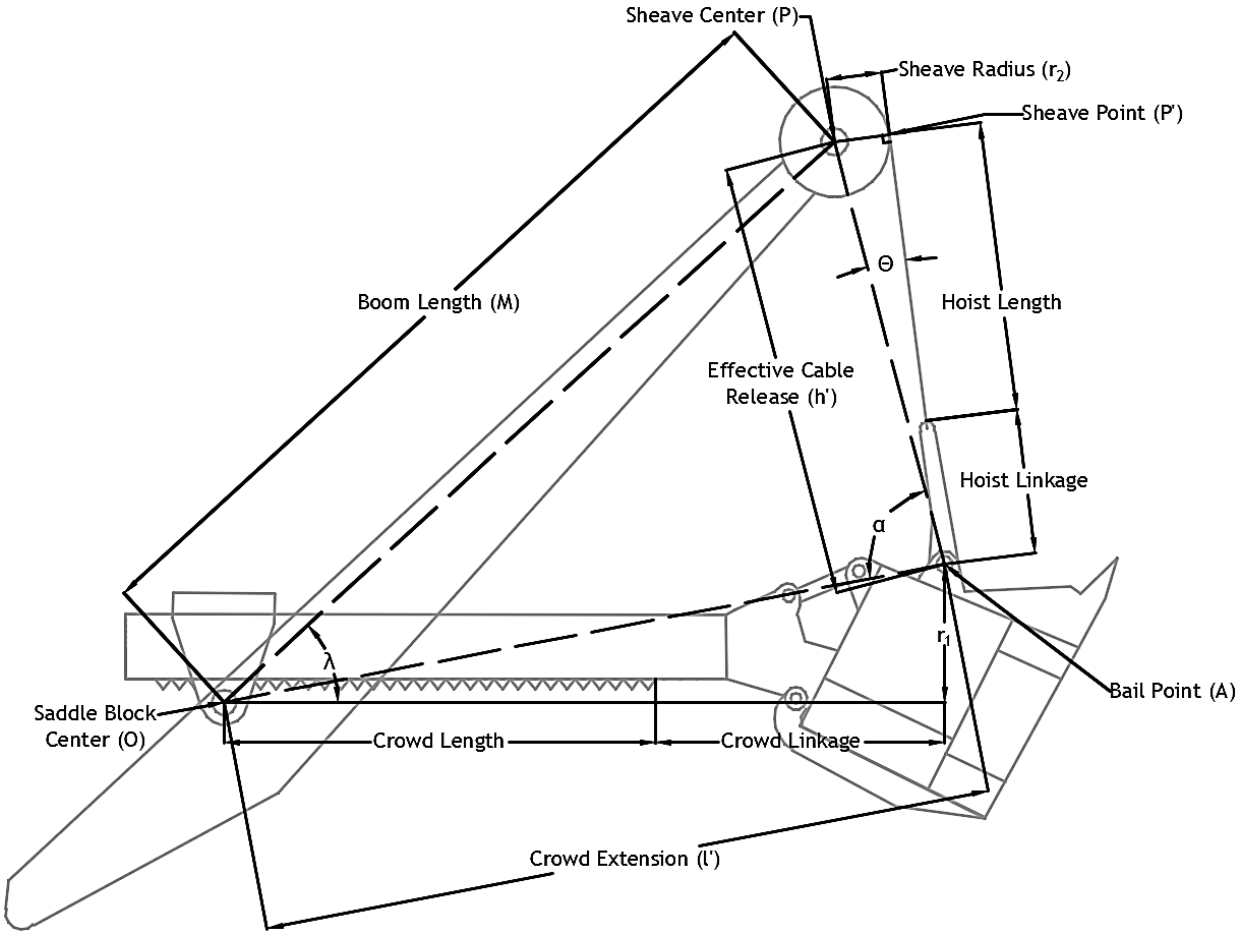


Figure 3-2: Shovel Geometry (after Joseph and Shi, 2012)

Several dimensions in this diagram are measured ones, and come from the P&H 4100 BOSS specification sheet (JoyGlobal, 2012). Measured dimensions are listed in Table 3-2.

Table 3-2: Shovel Dimensions (taken from JoyGlobal, 2012)

| | |
|---|---|
| $x_{sheave}$ (point P) | 20.0 m |
| $y_{sheave}$ (point P) | 20.5 m |
| $x_{saddle}$ | 9.0 m |
| $y_{saddle}$ | 10.1 m |
| Hoist Linkage | 2.6 m |
| Crowd Linkage | 5.7 m |
| Sheave Radius ($r_2$) | 1.3 m |
| Saddle Point-Bail Point ($r_1$) | 2.9 m |
| Boom (M) | 15.1 m |

Boom angle "λ" was determined using Equation 3-1, where $y_{sheave}$, $x_{Sheave}$, $y_{saddle}$, and $x_{Saddle}$ are with respect to the center of rotation of the shovel (see Figure 3-5); h' and l' are determined with equations 3-2 and 3-3.

$$\lambda = tan^{-1}\left(\frac{y_{Sheave} - y_{Saddle}}{x_{Sheave} - x_{Saddle}}\right) = 43° \quad \text{3-1}$$

$$Effective\ Cable\ Release = h' = \sqrt{(Hoist\ Length + Hoist\ Linkage)^2 + (r_2)^2} \quad \text{3-2}$$

$$Crowd\ Extension = \ l' = \sqrt{(Crowd\ Length + Crowd\ Linkage)^2 + (r_1)^2} \quad \text{3-3}$$

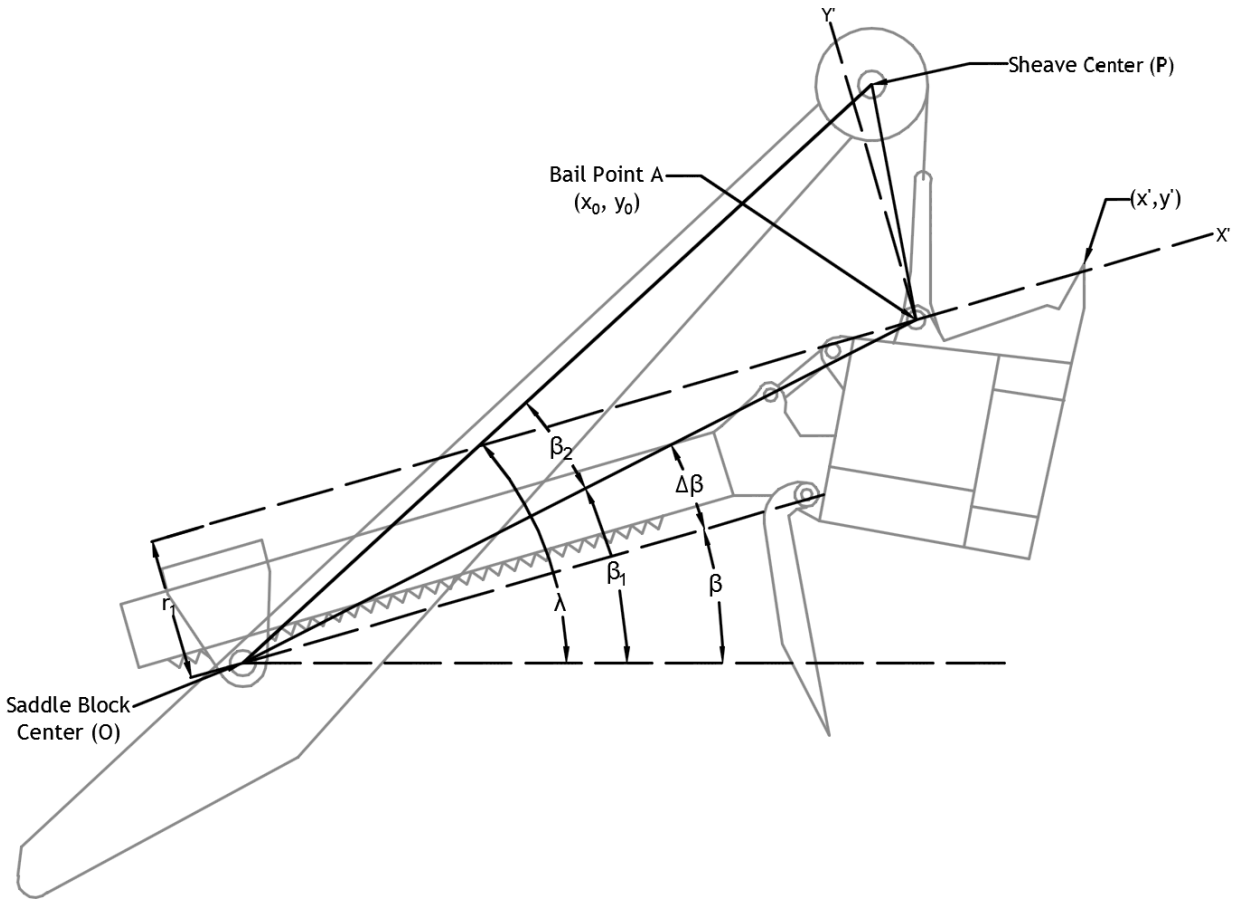


Figure 3-3: Shovel Dipper Angle Relationships (after Joseph and Shi, 2012)

Using the triangular relationship between the boom, hoist and crowd length, as well as the angle of the boom and dipper arm with respect to the horizontal, the location of the bail

point, and therefore dipper, could be found at any point in time. The angular relationship is as follows:

$$\beta_2 = cos^{-1}\left(\frac{l'^2 + M^2 - h'^2}{2 * M * l'}\right) \quad 3\text{-}4$$

$$\beta_1 = \lambda - \beta_2 \quad 3\text{-}5$$

$$\Delta\beta = \tan^{-1}\left(\frac{r_1}{l}\right) \quad 3\text{-}6$$

Where "l" refers to the combined crowd length and crowd linkage. Therefore the angle ß, which is horizontal to dipper handle, was found by equation 3-7.

$$\beta = \beta_1 - \Delta\beta \quad 3\text{-}7$$

The position of the bail point ($x_0$,$y_0$) at any point was found by equations 3-8 and 3-9.

$$x_0 = x_{saddle} + l'cos\beta_1 \quad 3\text{-}8$$

$$y_0 = y_{saddle} + l'sin\beta_1 \quad 3\text{-}9$$

The position of any point on the handle or dipper could then be extrapolated from the position of the bail point ($x_0$,$y_0$) by equations 3-10 and 3-11.

$$x = x_0 + x'cos\beta - y'sin\beta \quad 3\text{-}10$$

$$y = y_0 + x'sin\beta + y'cos\beta \quad 3\text{-}11$$

Where x' and y' are the distances from the bail point to the point of interest, measured along the new X' and Y' axis as shown in Figure 3-3. In the case of the tip of the shovel teeth for the P&H 4100 BOSS, it is 2.9m and 0.7m respectively. Equations 3-10 and 3-11 were then used to create a visualization of the path of the shovel teeth through the dig face. This visualization is shown in Figure 3-4.

Knowing the position of the shovel teeth at all times, in 0.1 second intervals, allows for a simple velocity calculation to be carried out. Velocity of the teeth through the dig face for each cycle was evaluated and averaged to obtain a velocity used in the abrasion test that formed the basis for this work.

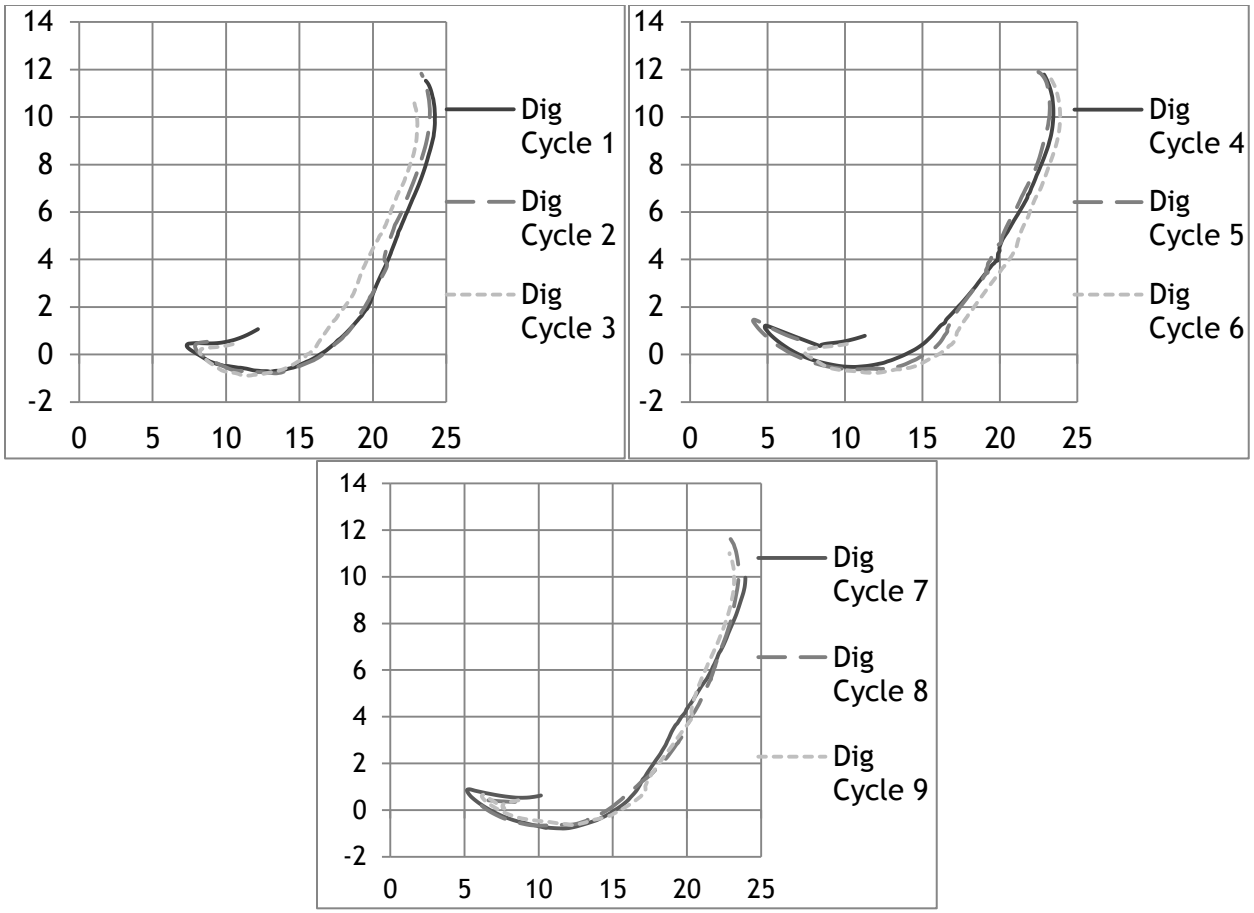


Figure 3-4: Shovel Path Visualization, axes shown are in meters with the zero reference being the axis of rotation of the shovel, at the bottom of the tracks, as shown in Figure 3-5

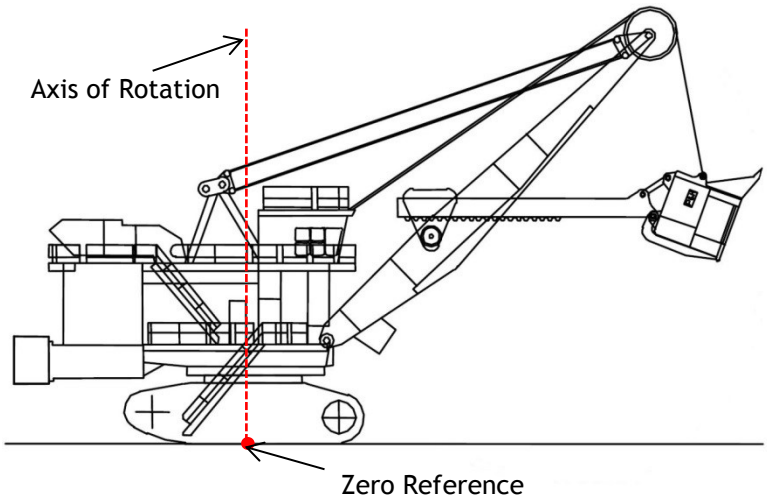


Figure 3-5: Cable Shovel Diagram Showing Axis of Rotation and Zero Reference Point for Shovel Path Visualization (after Joseph and Shi, 2011)

## 3.3 Shovel Dig Force Determination

Crowd force and hoist force were calculated from the data in Table 3-1 with the following equations:

$$F_{Crowd} = \frac{V_{Crowd} * I_{Crowd}}{v_{Crowd}} \quad 3\text{-}12$$

$$F_{Hoist} = \frac{2 * V_{Hoist} * I_{Hoist}}{v_{Hoist}} * \eta_{Hoist} \quad 3\text{-}13$$

Where $\eta_{Hoist}$ is the efficiency of the hoist mechanism, which for the P&H 4100 BOSS is 86.5%, as referenced in Joseph and Shi, 2012. This number came from a study where the efficiency of electric excavator hoist systems and effort reacted at the dipper and ground engaging tool was examined, and it was found that regardless of excavator model, the efficiency remained at 86.5% (Joseph and Shi, 2012). This held true for excavator models from the P&H 2100 up through the 4100. The constant of "2" refers to the two hoist motors on the shovel. Figure 3-6 shows the resultant forces and their associated moment arms. The moments created by each of the forces shown were summed about the saddle point to facilitate determination of the dig resistance. Crowd forces can be ignored in the moment calculations for multiple reasons including that the moment arm of that force is significantly smaller than the others, the force itself is two orders of magnitude or more less than the hoist force, and crowd forces only actually come into play in the initial positioning of the dipper at the dig face, and do not contribute greatly through the actual dig cycle.

The accumulation of oil sand mass within the dipper as it travels through the dig face must be taken into account to gain an accurate dig resistance. To do so, it was assumed that the dipper is filled to capacity with every dig cycle, and it was filled at a linear rate as it proceeded through the dig face. Using the previously determined trajectory of the teeth, the total length of the dig cycle was easily determined; this total length was then used to determine the proportion of the dig cycle the dipper had currently progressed through, and therefore the amount of oil sand in the dipper at that time.

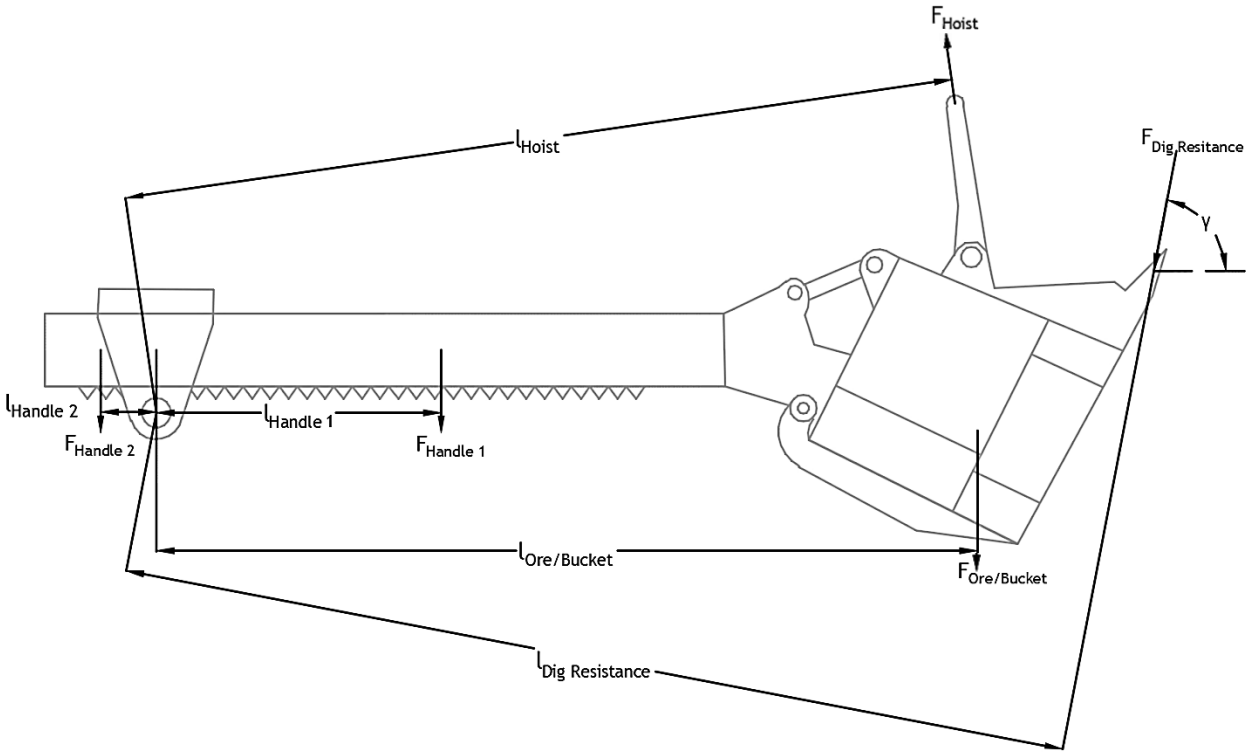


Figure 3-6: Shovel Dipper/Handle Forces (after Joseph and Shi, 2012)

The struck capacity of the dipper on a 4100BOSS is 44.3 $m^3$; taking bank density of oil sand to be 2.15 $t/m^3$, with a swell factor of 1.3 (Joseph and Shi, 2012) results in a total oil sand payload of 73.3t when completely full. Combined with the dipper mass of 80.8t, total mass when fully loaded was therefore 154.1 t. This mass was considered to act at the centroid of the dipper, as shown in Figure 3-6. The position of this resultant comes from work done by Joseph and Shi (2012). The centroid of the oil sand material mass will be changing slightly as material flows into the dipper, however these small changes have been ignored as the moment arm for this force is in the range of several meters during the dig cycle, whereas the position of the centroid changes on a much smaller scale. Formula 3-14 shows the calculation for this moment:

$$M_{Ore} = [(\phi * 73.3t) + 80.7t] * 9.81\frac{m}{s^2} * l_{Ore/Bucket} * \cos\beta \qquad 3\text{-}14$$

Where ϕ refers to the percentage of the current dig cycle that has been completed, and $l_{Ore/Bucket}$ refers to the crowd length plus the distance from the end of the crowd mechanism to the centroid of the ore and dipper.

Total mass of the handle is 38.8t (Lin, 2013), summing the moment created by this force needed the portion of the handle ahead of the saddle point as well as behind it to be taken into account. This is illustrated in Figure 3-6. The resultant moment calculation is shown in formula 3-15.

$$M_{Handle} = cos\beta * 0.5 * Unit\ Length\ Mass\ of\ Handle * (l_1^2 - l_2^2) \quad 3\text{-}15$$

To determine the moment arm for the hoist force, the angles α and θ (Figure 3-2) needed to be determined

$$\alpha = cos^{-1}\left(\frac{l'^2 + h'^2 - M^2}{2 * h' * l'}\right) \quad 3\text{-}16$$

$$\theta = sin^{-1}\left(\frac{r_2}{h'}\right) \quad 3\text{-}17$$

$$M_{Hoist} = \sin(\theta + \alpha) * l' \quad 3\text{-}18$$

Summing the moments about the saddle point, the resultant moment could be determined, and therefore the resultant force. This resultant force was the dig resistance, and while part of this force was due to the friction of the dipper face going through the ore, it was assumed that the majority of this resistance comes directly from the tooth-oil sand interaction. The calculations are shown in equation 3-19 and 3-20, while ∠OPC and ∠OCP are illustrated in Figure 3-7.

$$M_R = F_{Dig\ Resistance} * l_r = M_{Hoist} - M_{Ore/Bucket} - M_{Handle} \quad 3\text{-}19$$

$$l_r = l_o * \sin(\lambda + \angle\mathrm{OPC} + \angle\mathrm{OCP} - \gamma) \quad 3\text{-}20$$

Where the angle γ comes from the relationship between blade direction as well as the friction angle between tool and oil-sand, $\delta_{\text{Oilsand/Tooth,}}$ which is 37° (Joseph and Shi, 2012). Angle γ is given by equation 3-21, where ε is the angle between the shovel front and handle, as shown in Figure 3-8.

$$\gamma = \beta + \varepsilon + (90° - \delta_{Oilsand/Tooth}) \quad 3\text{-}21$$

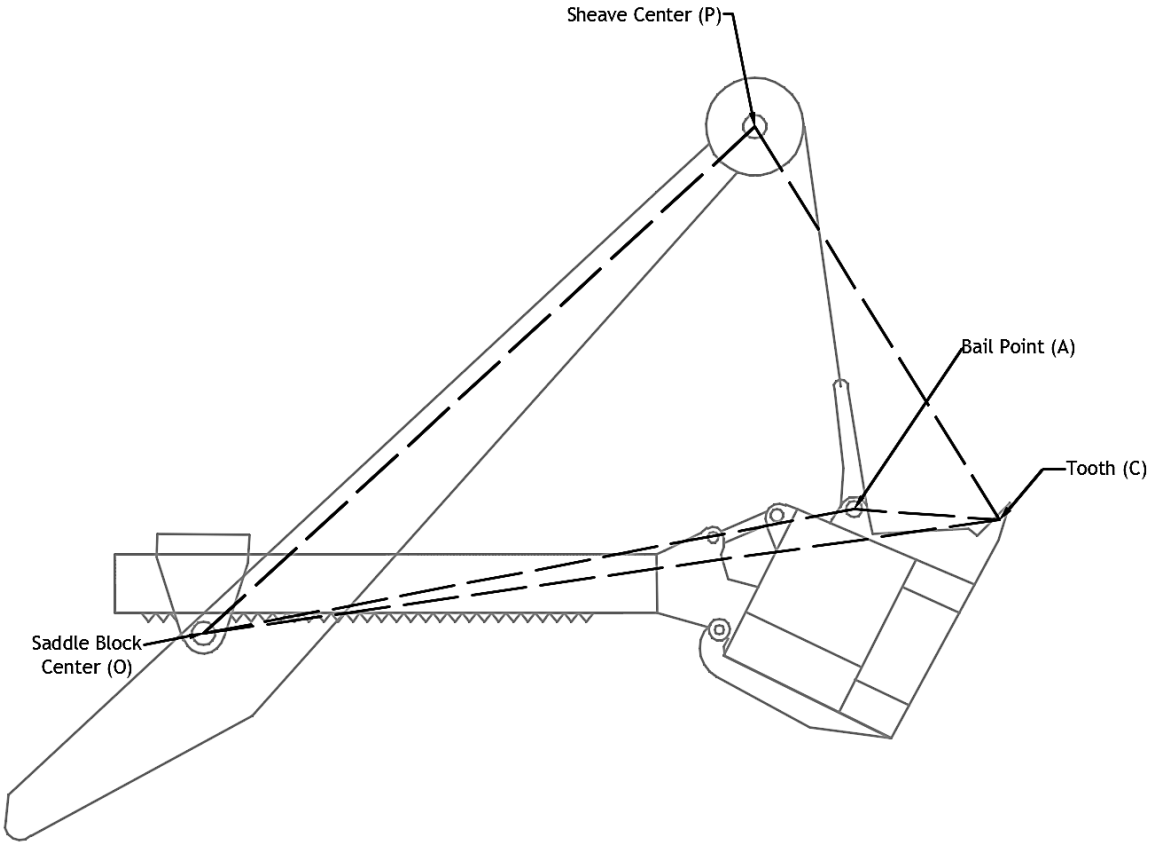


Figure 3-7: Shovel Teeth Geometry (after Joseph and Shi, 2012)

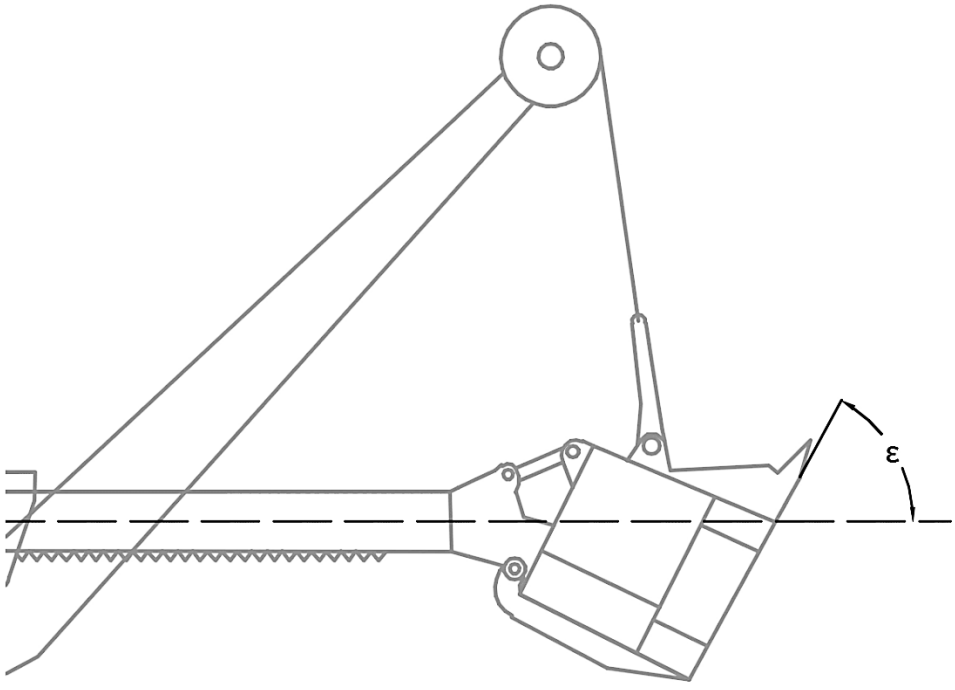


Figure 3-8: Shovel Handle/Dipper Front Angle (after Joseph and Shi, 2012)

Total dig resistance acts on the tooth at the angle γ, but for the purposes of the testing in this work, the force normal to the tooth face was required. This was determined by equation 3-22, which is illustrated in Figure 3-9.

$$F_{R\,Normal} = F_R * \sin\big(\gamma - (\beta + \varepsilon - \zeta)\big) \qquad 3\text{-}22$$

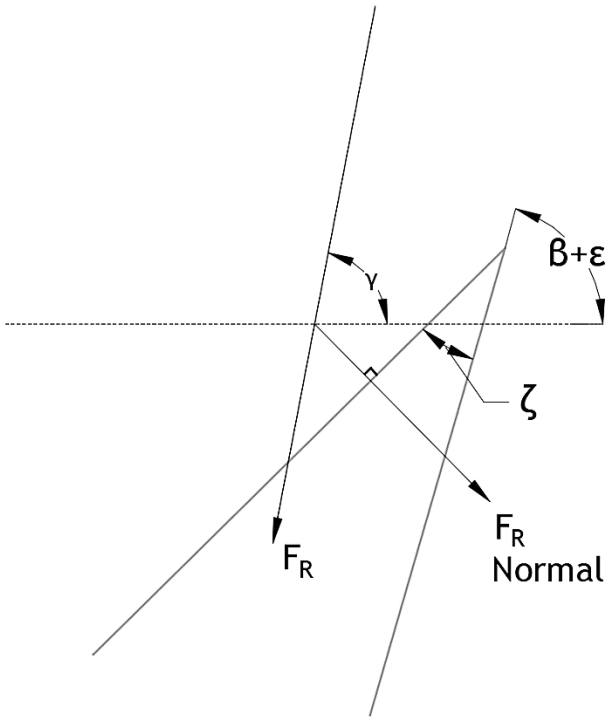


Figure 3-9: Tooth Normal Force (after Joseph and Shi, 2012)

Where ζ is the inherent angle of the shovel tooth, which in this case was found to be 17°, and was directly measured from an un-used tooth.

With the normal force acting on the teeth throughout the entire dig cycle calculated, an average was taken of the force through nine dig cycles. The results from the data used are shown in Table 3-3. The overall average force obtained through all nine dig cycles was used in designing the abrasion test that formed the basis for this work.

Table 3-3: Shovel Tooth Force Results

| Dig Cycle | Force (kN) | | |
|---|---|---|---|
| | Average | Max | Min |
| 1 | 1043.4 | 1838.0 | 72.2 |
| 2 | 1358.6 | 2993.8 | 19.4 |
| 3 | 1312.7 | 2160.2 | 3.8 |
| 4 | 1300.9 | 8931.8 | 148.6 |
| 5 | 1596.3 | 8311.8 | 5.4 |
| 6 | 1330.3 | 2232.2 | 9.0 |
| 7 | 769.2 | 1981.9 | 19.1 |
| 8 | 1430.0 | 2823.9 | 68.9 |
| 9 | 1433.5 | 6061.0 | 3.5 |
| Average | 1286.1 | 4148.3 | 38.9 |

# 4 Test Development/Methodology

When developing a new test many aspects must be taken into account. If intended for engineering purposes, the test must accurately represent most of the aspects that are experienced in the real-world application it is being designed to mimic. Materials, geometry, motion, loading, lubrication, ambient environment and heat dissipation and generation must be paid attention to (Bayer, 1994). If testing indicates a strong sensitivity to an element, that element is likely a significant one that may warrant further investigation.

Rubber wheel-type apparatus are the current standard for three-body abrasive wear tests (ASTM, 2010; 2007). The ASTM Standard G65 test is probably the most well-known test, and basically consists of a rubber wheel turning against a specimen, with a continuous flow of silica sand between the rubber wheel and specimen. It functions well as a standardized test, but tends to fall short if the intention of testing is to model field wear conditions.

The G65 test formed the basis for work by Lin (2013), which was continued in this study. The only major changes to Lin's system was the addition of a worm drive gear system to increase torque at the wheel, and the use of an electrical actuator to provide the force on the lever arm. The major differences between this modified G65 test and the standardized one is the abrasive media choice, particle flow rate, size of the wheel, applied force, rotation velocity, as well as test duration. The G65 test functions well as a standardized test, but it was hoped that the parameter changes instituted would help create a test environment that is more indicative of field conditions.

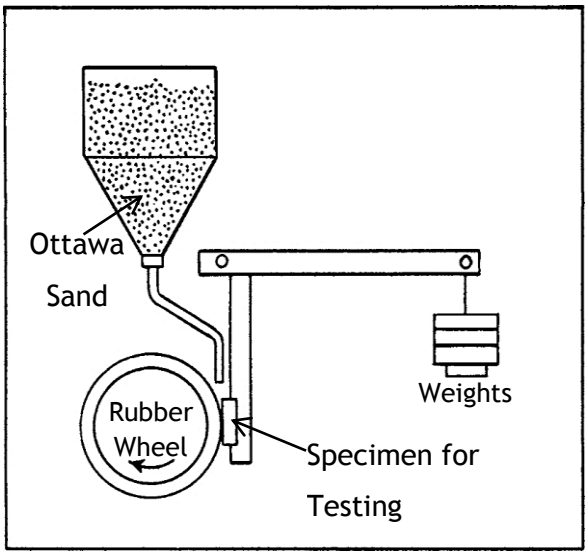


Figure 4-1: ASTM Standard G65 Testing Schematic (after ASTM, 2010)

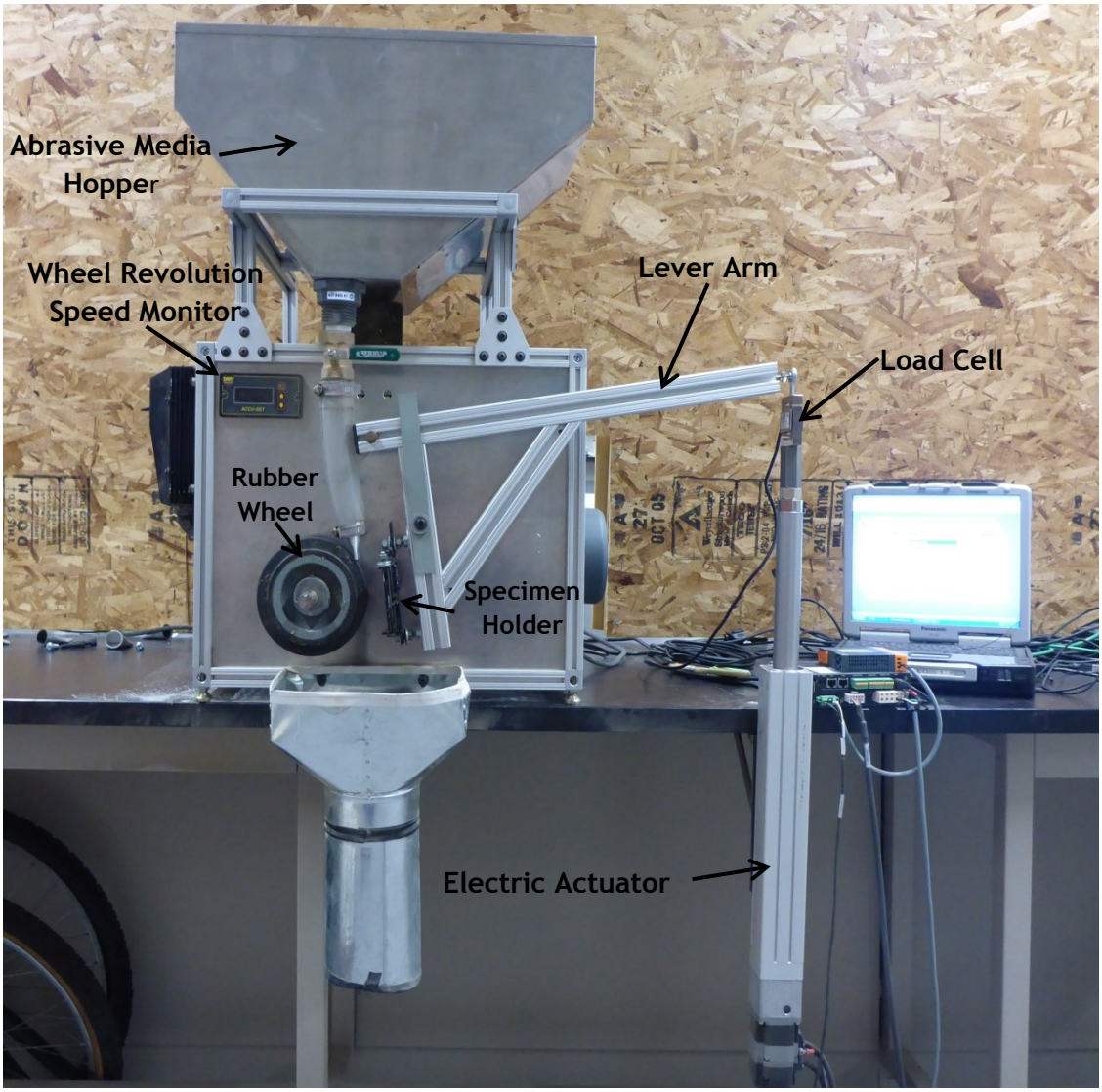


Figure 4-2: Modified Abrasion Testing Apparatus

## 4.1 Test Parameters

### 4.1.1 Abrasive Media

The abrasive media for the G65 test is rounded quartz sand, between 425 µm and 150 µm in size, with no more than 5% larger than 300µm, and no more than 5% smaller than 212µm. For the rubber wheel test used in this work, four different types of sand were used: raw oil sand with the bitumen fraction stripped (hereafter referred to as “Raw Oil Sand”), oil sand from a tailings beach source (“Tailings Beach Sand”), a rock core sample of metamorphic silicate

crushed down to the size of sand from near the Diavik diamond mine (referred to hereafter as "Granite Sand" for simplicity), and cube mould test sand ("Silica Sand"). These sands were selected to provide a range of particle shapes and hardness that could be encountered in field situations. All sand was thoroughly air dried to remove moisture before testing.

The raw oil sand and tailings beach sand exhibited similar shapes, with the tailings sand slightly more angular and significantly smaller. The granite sand exhibited the highest angularity, and the cube mould test sand the lowest angularity. Sand particle images are shown in Figure 4-3, particle size distributions are shown in Figure 4-4.

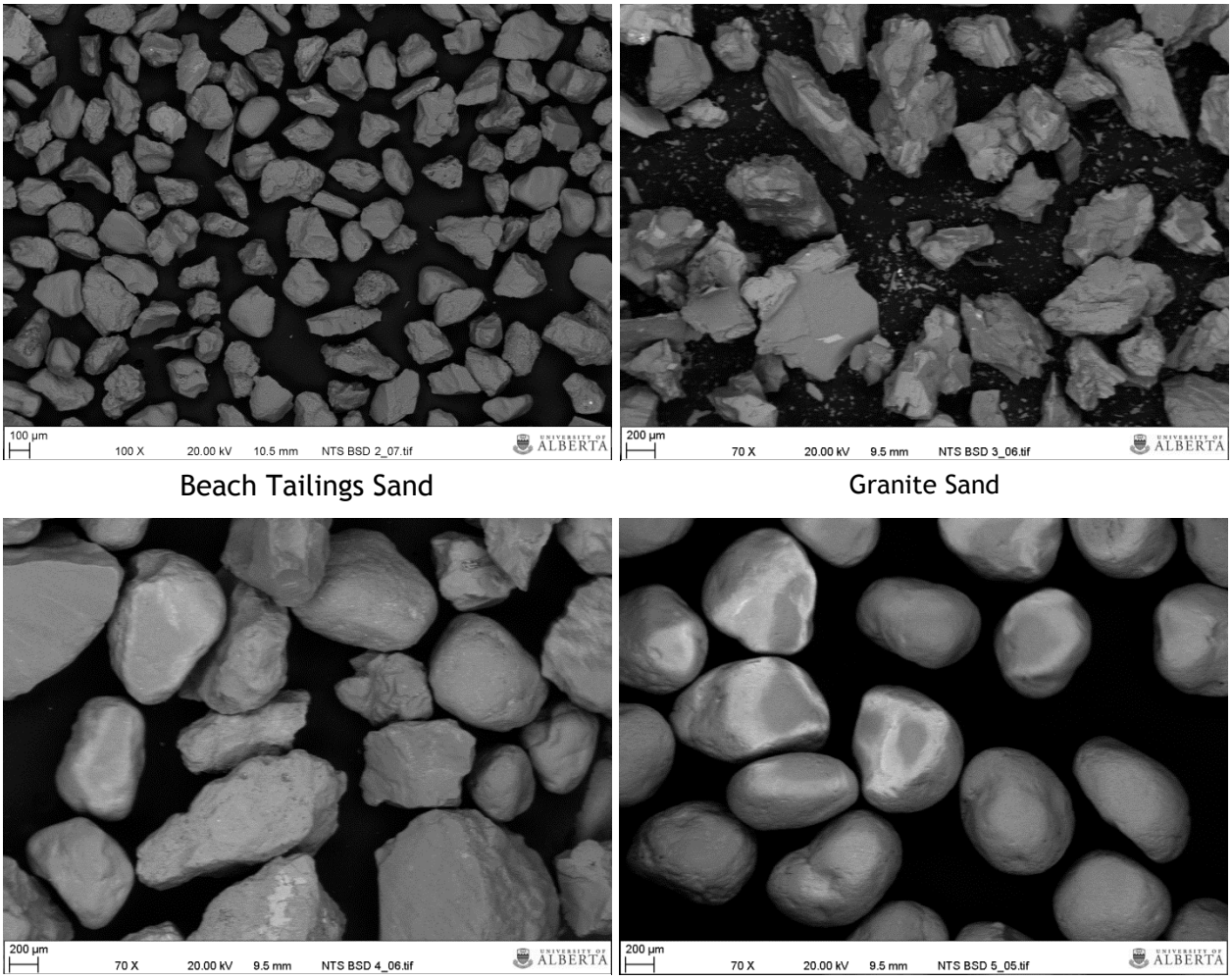


Beach Tailings Sand | Granite Sand

Raw Oil Sand | Silica Sand

Figure 4-3: SEM Images of Sand Particles

As mentioned above, the beach tailings sand and raw oil sand used in this modified abrasion test are two different types of oil sand which have had the bitumen fraction stripped. The reason for using this type of sand is to ensure that it may flow continuously in the testing

machine used; if the bitumen fraction was still present, the test would clog and not function even remotely properly.

However, it was the belief of the author that the removal of the bitumen fraction would not heavily influence actual abrasive wear. The reason for this is touched on in section 2.2.3.1, but is based on two properties of oil sand. Oil sand has no cohesion in triaxial tests (Dusseault and Morgenstern, 1978), and as such would not be expected to cause any adhesive wear. The second property is the fact that oil sand is "water wet" (Dusseault and Morgenstern, 1978), and interaction between the oil sand and specimen should be dominated by the water, rather than bitumen.

The lubricative properties of bitumen and specifically how they influence abrasive wear have not been greatly studied, and may warrant further investigation in another study.

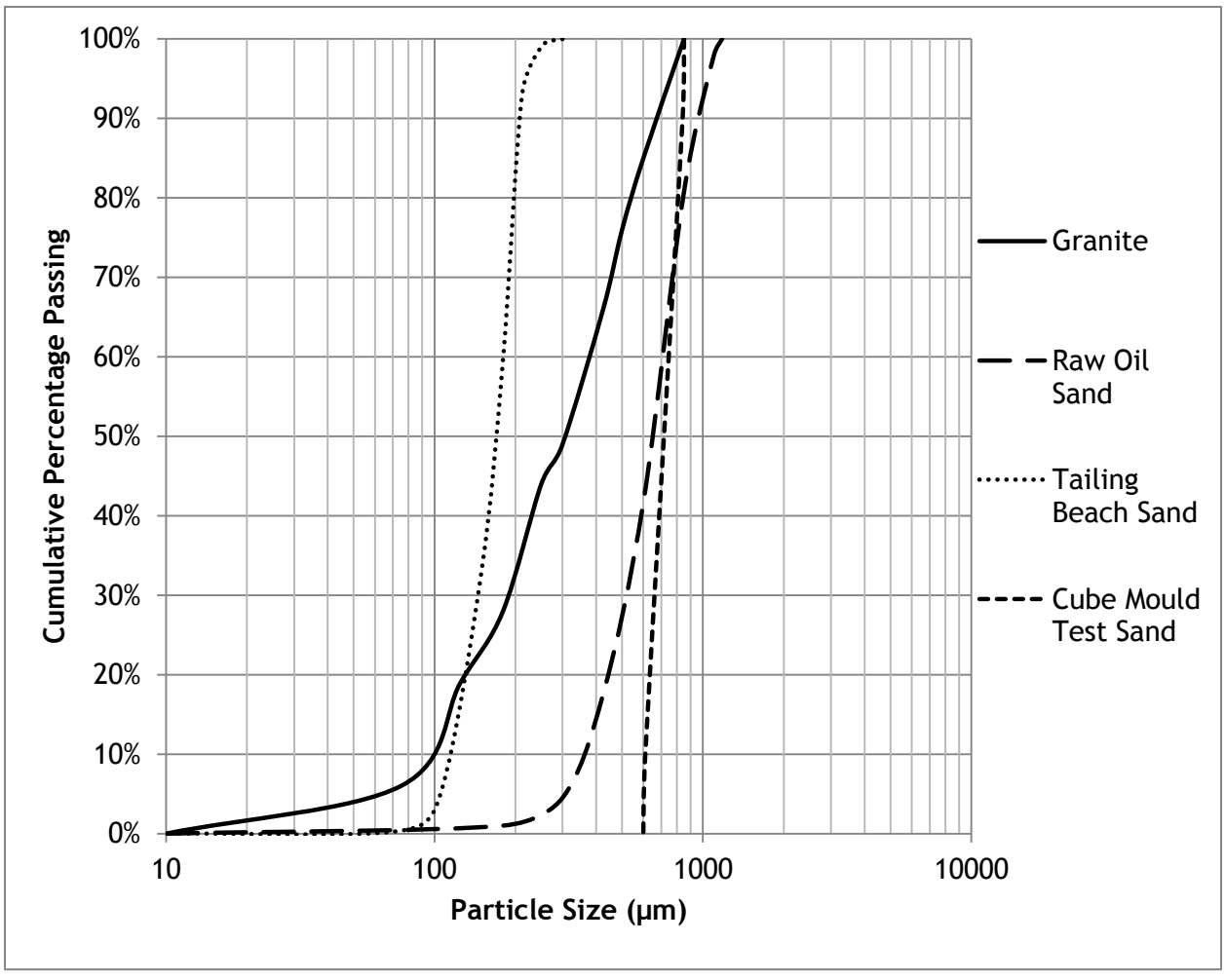


Figure 4-4: Particle Size Distribution

#### *4.1.1.1 Abrasive Media Hardness*

For the oil sand, based on Carrigy's (1966) observations on oil sand mineralogical components, the majority of minerals exhibit extremely high hardness. The vast majority of particles present in oil sand are quartz, or based on the same silicon dioxide, and exhibit hardnesses in excess of 1100 Hv, making this an appropriate assumption for the hardness of the two oil sand types.

The granite sample was ground from core samples obtained from the Diavik diamond mine, of the surrounding host rock. It is a mix of quartz, feldspar and others; hardness of a similar rock has been given as approximately 1070 Hv (Kulu, Tarbe, Kaerdi, and Goljandin, 2009)

The cube mould test sand is a natural Ottawa silica sand, which would share a very similar hardness with the quartz particles in oil sand, 1100 Hv has been deemed an appropriate estimate for this sand type as well.

### 4.1.2 Flow Rate

The G65 test specifies a flow rate of between 300-400g/minute of media. As each of the four abrasive types had different size distributions, four different nozzles were made for use in testing. The nozzles were created with opening wide enough to allow 3 of the maximum size particles to pass through at a time (ie, cube mould test sand nozzle width was 2.5mm). This ensured an even flow rate through the nozzle with a minimal amount of clogging.

The actual flow rate for each nozzle was not especially important. Nozzles were created that provided a feed consistently wider than the wheel and at a rate that ensured saturation between the sample and the wheel, which was the important aspect of flow rate. Interestingly, when the flow rate of the apparatus was tested, this method resulted in a flow rate similar to that of the G65.

### 4.1.3 Size of Wheel

The size of the wheel used in the test was six inches in diameter, by two inches wide. This was the size of wheel used by Lin (2013), and rather than switching to a nine inch diameter by half inch wide wheel as mandated by the G65 test, the same wheel was used. It is not believed that the diameter of the wheel should be a focus of abrasion testing, and therefore this six inch wheel was deemed appropriate for testing.

### 4.1.4 Applied Force

The calculations in chapter 3 focussed on the analysis of the forces experienced by a shovel as it digs through oil sand. This analysis determined that, through nine dig cycles, the average force experienced at the shovel teeth was 1290 kN. This force was used to in the development of a test that is indicative of field conditions, shown in this section.

The parts of a cable shovel bucket that typically make contact with ore in a dig cycle are known as "ground engaging tools" (GET). These parts are available in a multitude of formats and styles, but for the most part cable shovel GET consists of adapters, tips (teeth) and lip shrouds. Additional protection can be added along the sides of the bucket as needed to prevent excessive wear; these pieces are typically referred to as edge protection.

It was assumed that the dig resistance force experienced by the shovel is for the most part evenly distributed across the entire GET system. This area is illustrated in Figure 4-5.

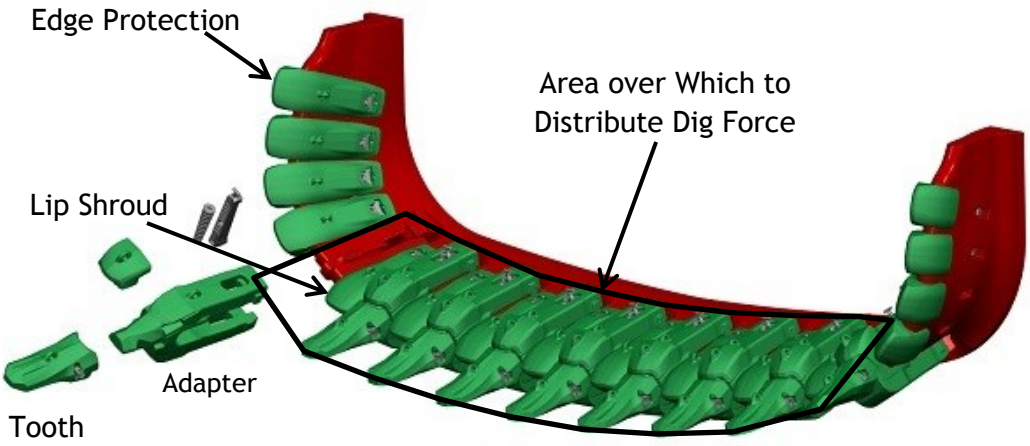


Figure 4-5: Shovel Ground Engaging Tools (adapted from ESCO, 2016)

A new and un-used electric cable shovel tooth and adapter were measured for the purposes of determining what force should be applied to the coupon during testing. The total area over which the dig force is to be distributed was calculated as follows in equation 4-1.

$$Distributed\ Load\ Area = Length_{Adapter} * Width_{Bucket} + Area_{Tooth} * \#\ of\ Teeth \quad 4\text{-}1$$

Bucket volume can be highly variable, depending on requests made by the consumer at the time of purchase, however they can generally be considered cubic in nature, so the width of the bucket is simply the cubic root of the volume. Nominal dipper capacity of the P&H 4100

BOSS is given on the company website as 44.3$m^3$, meaning a bucket width assumption of 3.54 m could be considered accurate. The length of adapter and area of the tooth were measured as discussed above, and come out to 0.45 m and 0.1196 $m^2$, respectively. The number of teeth on a P&H BOSS operating in the oil sands is nine.


Figure 4-6: Adapter and Tooth

Substituting into equation 4-1 we get an area of 2.605 $m^2$. This is the total area that the dig force experienced by the shovel can be considered to act over. When combined with the average dig force calculated earlier, a pressure of 495 kPa could be considered to act upon the shovel teeth.

Next, the wear scar produced on a chrome carbide sample was measured to determine the force required to match the pressure experienced by the shovel teeth. The wear scar was produced after undergoing an abrasion test in the machine developed for this work, for a total of 20 minutes, at a load of 300N on the sample, or 23.9lbs on the lever arm. This force was determined using the average of the entire shovel force curve and a wear scar produced by earlier testing of a regular steel sample.

The wear scar produced in this initial trial run on chrome carbide measured 1.5 cm by 4.2 cm, or 6.3 $cm^2$. To achieve a pressure of 495 kPa therefore, a force of 312 N needed be applied to the chrome carbide sample. Measurements of the lever arm determined that the lever arm ratio was 2.82, and therefore force applied by the electric actuator should be 110.6 N, or 24.8 lbs.

The apparatus used for this work can be seen in Figure 4-2. It did not employ the use of suspended weights in the same way as the standard G65 test. An electric actuator provided the force, which was measured and recorded by a load cell. This load cell did not actively adjust the force applied, so the user had to constantly monitor the test to ensure the proper load was being applied. This method was thought to be superior, as it would prevent any bouncing of the lever arm associated with the standard method used in the G65.

However, this method is subject to some errors, as the user must read from a graph what force is currently being applied. Applied forces on each sample were averaged across all 40 minutes of testing, and are summarized in Table 4-1. The recorded force from a single ten minute test (Sample 1, first 10 minute abrasion test), is shown in graphical format in Figure 4-7 as an example. It can be seen that while the force varies continuously throughout the test, it does not greatly deviate from the intended load of 24.8lbs.

Table 4-1: Average Load Applied by Lever Arm Actuator over 40 Minutes of Abrasion Test

| Sample | Average Load (lbs) |
|---|---|
| 1 | 25.12 |
| 2 | 24.95 |
| 3 | 25.26 |
| 4 | 25.09 |
| 5 | 24.74 |
| 6 | 24.75 |
| 7 | 24.80 |
| 8 | 24.79 |
| 9 | 24.66 |
| 10 | 24.70 |
| 11 | 24.87 |
| 12 | 24.84 |
| Overall | 24.88 |

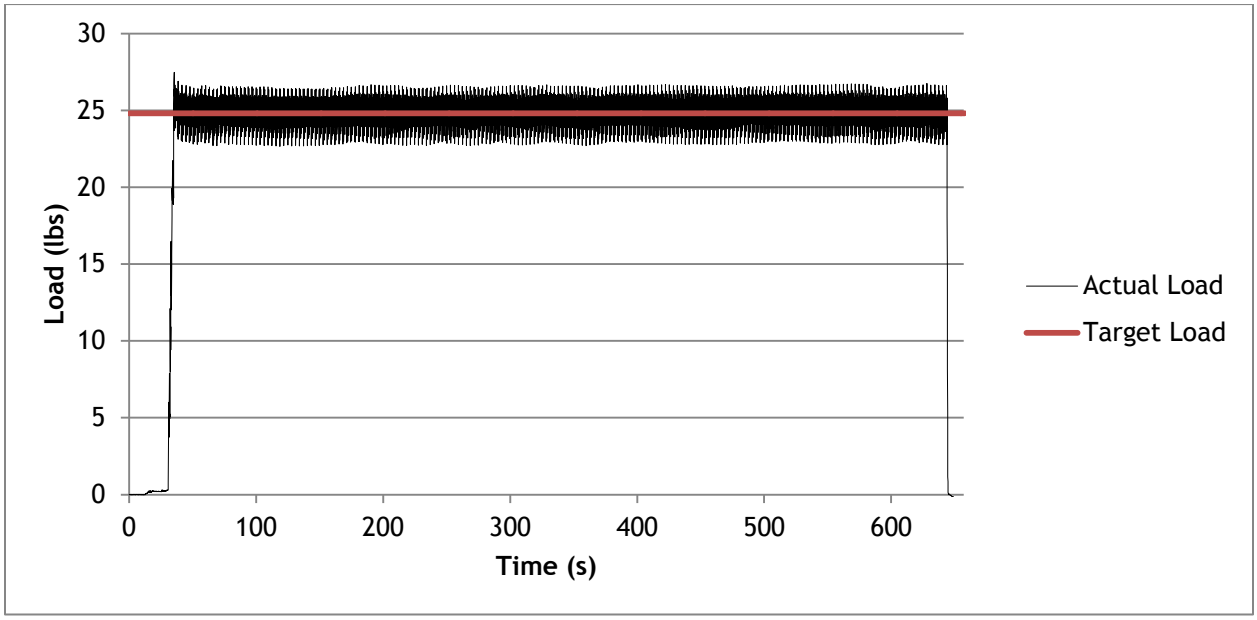


Figure 4-7: Load Data from Sample 1, First 10 Minutes of Abrasion Testing

### 4.1.5 Rotation Velocity/Test Duration

The same data analyzed to determine shovel dig forces was used to determine the shovel dipper trajectory. This trajectory was examined to determine average velocity of the shovel teeth through the dig cycle. Across nine dig cycles, the average velocity through the dig face was 0.775 m/s. No scaling factor was applied to this parameter.

The diameter of the rubber wheel used in testing was 14.8 cm in diameter. This means that to obtain a speed of 0.775 m/s, the wheel needed to operate at 100 RPM. Testing was conducted in 10 minute intervals, up to 40 minutes overall. This means that for every 10 minute interval, the sample underwent 465 lineal meters of abrasion, and 1860 meters overall for the entire 40 minutes of the test. This is similar to the Procedure B for the G65 test. Procedure B is generally used to measure materials that are in the medium to low abrasion resistance category, as they cannot stand up to the more “severe” procedures that are standardized within the G65 test.

## 4.2 Test Procedure

Testing was done indoors, at a temperature of 19°C, at a relative humidity of approximately 30%.

The test specimens began as an 8”x11” sheet of chrome carbide overlaid on base steel. This plate was cut down by water jet into testing appropriate size samples (2.5”x3”). Samples were then ground on a surface grinder down to a smooth, even finish. The testing procedure is as follows:

- Clean samples with acetone
- Record weight to extremely high accuracy (0.0001 gram)
- Place samples into holder on lever arm, secure in place
- Start wheel, allow motor time to warm up (5-10 minutes)
- When warm up time has elapsed, start flow of sand and using lever arm electric actuator adjust until sample makes contact with wheel, and load cell reads appropriate load
- Allow sample to undergo 10 minutes of abrasion
- Adjust lever arm away from wheel
- Remove sample

The above process is repeated three more times, until the sample has undergone 40 minutes of total abrasive testing. Samples were handled carefully at all times and cleaned thoroughly before each weight measurement to ensure the total mass loss was indicative of abrasive wear loss alone.

## 4.3 Power Draw and Specific Energy Calculations

Specific energy is defined as energy per unit volume, in this case applied to the energy required to remove material through wear processes. Energy per unit volume, when expressed as $N*m/m^3$, can be seen to assume units of pressure. It was expected that this energy expended per unit volume should remain constant in both the field and scale test.

In order to determine the energy expended during tests, voltage and current draw of the testing machine motor were monitored through the use of digital multimeters. Power draw of the motor during the test was compared to the steady state, unloaded operating draw of the motor to determine the energy expended during the test. Power draw curves are shown in Figure 4-8 which formed the basis for this analysis.

The area under the curve between the start of the test (t=0 minutes), and the end of the test (t=10 minutes) was multiplied by the test duration to find the energy expended during the wear process. Every effort was made to allow the machine to warm up to a steady state

power draw before testing, however in all cases it was found that no matter what amount of time was devoted to warm up, the steady state, unloaded power draw inevitably dropped in magnitude when comparing the beginning to the end of the test. This could likely be attributed to the increased load, and therefore increased operating temperature and efficiency of the motor. Regardless, this change was insignificant (less than $^{1}/_{10}^{th}$ of a watt).

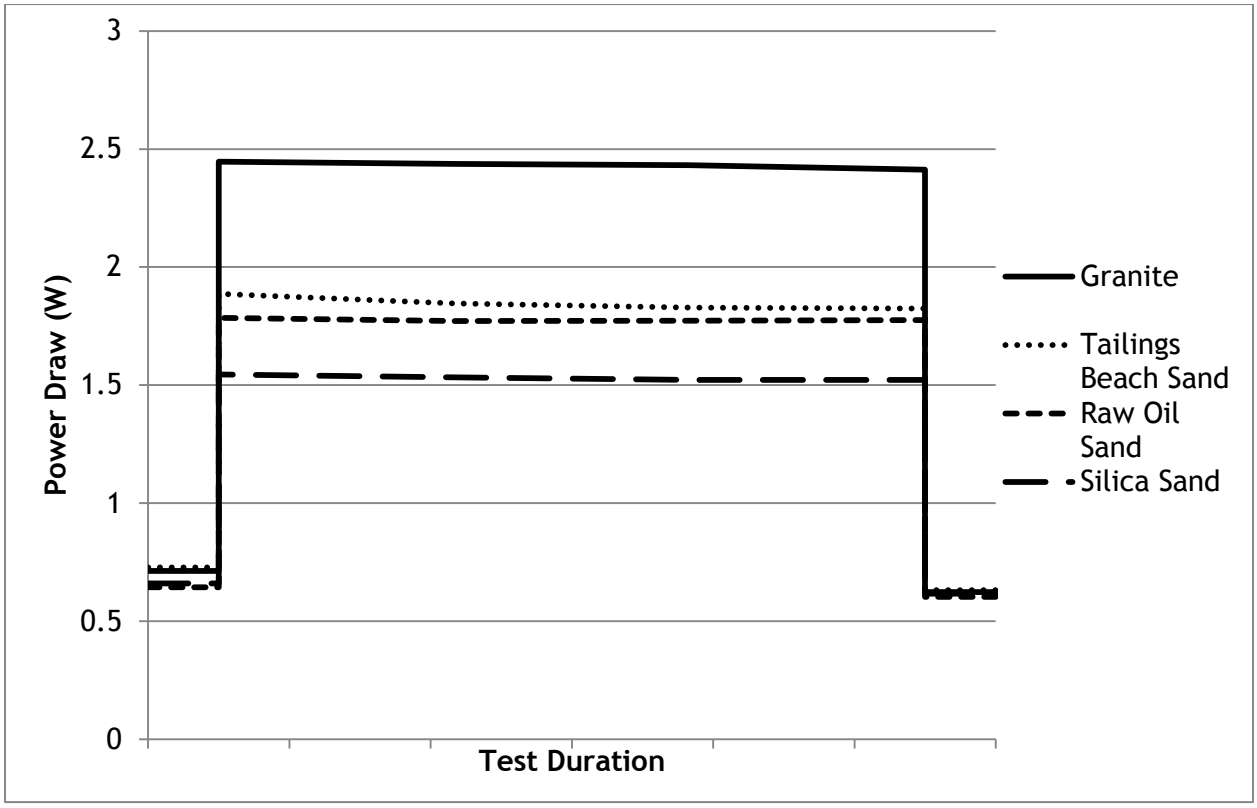


Figure 4-8: Power Draw by Material Type

Table 4-2: Power Draw and Energy Expenditure per 10 Minute Test

| | Average Power Draw During Test (W) | Energy (J) |
|---|---|---|
| Granite Sand | 1.763 | 1058 |
| Tailings Beach Sand | 1.166 | 700 |
| Raw Oil Sand | 1.152 | 691 |
| Silica Sand | 0.892 | 535 |

Specific energy is further reviewed in section 6.6.

# 5 Particle Analysis

## 5.1 Introduction

Representative samples were taken from each of the four sand types in order to facilitate particle shape analysis. These representative samples were further sampled randomly, after which a scanning electron microscope was used to collect images for shape analysis. Images were analyzed for shape parameters using programs adapted from those developed for MatLab by Stachowiak (2013), and Balideh (2015).

## 5.2 Scanning Electron Microscope

For particle analysis in this work, a Zeiss EVO MA15 scanning electron microscope (SEM) with a LaB6 electron source was utilized. This particular SEM has a resolution of approximately 100nm. Images captured for angularity and form analysis were captured at extremely high contrast in backscatter electron mode, for texture analysis by the grey scale method images were captured in secondary electron mode. An accelerating voltage of 20 kV was used.

Sand particles were mounted on one centimeter diameter round stubs with great care taken to ensure that particles did not overlap with one another. This is especially important, as overlapping particles would not be accurately recognized by the image analysis software and would lead to false results. Once sand particles were mounted on these stubs, conductive carbon coatings were applied using a Nanotek SEMprep 2 sputter to prepare for imaging.

## 5.3 Sampling

In order to gain an accurate representative sample, all four sand types were poured into the testing machine hopper and through the nozzle, with a sample being taken every 30 seconds until all material had passed through the nozzle. After this initial sampling, the cone method was used to further reduce the sample to a smaller size.

The cone method involves pouring material into a cone pile, flattening the cone, and then dividing that pile into 4 quarters. Two opposite quarters are saved, and the other two are discarded. This process was repeated several times until a suitable size sample remained for the final selection of particles.

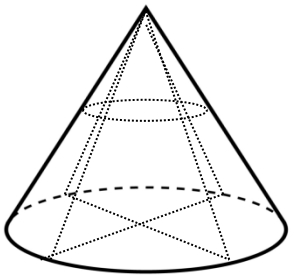

Figure 5-1: Cone Method

Even with the large amount of care taken thus far in ensuring an accurate and representative sample, the final sample of particles taken had to be done at random. This is not ideal, however when taking such a small sample (a few hundred sand particles) from such a large overall (millions or perhaps billions of sand particles), some sampling error was inevitable. Enough care was taken in this process that the sampling error is sufficiently small, and when the number of particles sampled is taken into account, a fairly accurate result should be obtained.

## 5.4 Image Analysis Process

### 5.4.1 Angularity and Form

The basic process for analysis of angularity and form is as follows: an image is read in from a file, converted to a black and white image, very small particles and imperfections are removed, any particles that are not completely within the boundaries of the photograph are removed, and finally the boundary of each particle is analyzed and stored as a set of X and Y coordinates. Using these X and Y coordinates, the different shape parameters are calculated. This process is illustrated in Figure 5-2.

Images for particle shape factor analysis were captured at extremely high contrast in backscatter electron mode in order to better ascertain the shape of each particle. Due to this, very little difference can be seen after the conversion to black and white. In the original image, each pixel was assigned a greyscale value from 0-255 (0 is black, 255 is white). After conversion to black and white, each pixel had the binary value of 0 or 1 (0 is black, 1 is white), which formed the basis for further analysis.

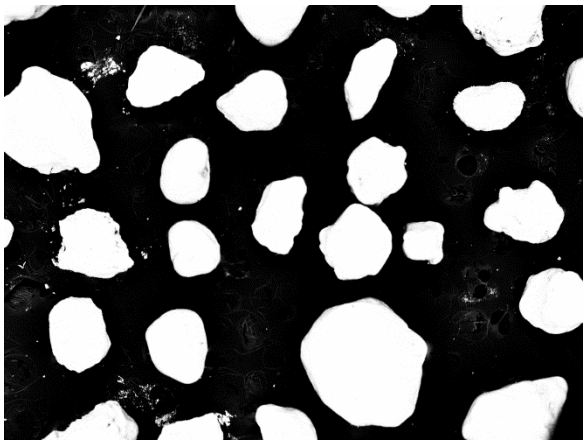

**1 – Read image into program**

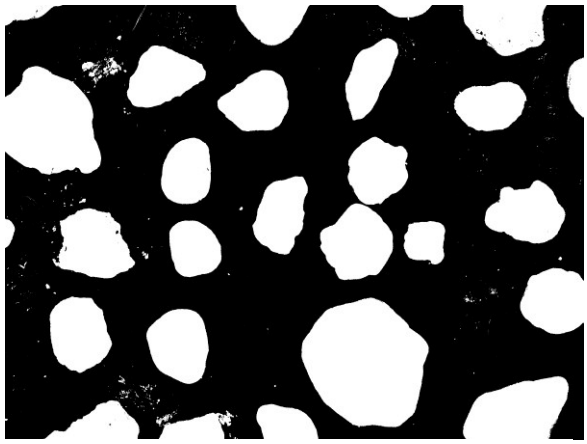

**2 – Convert from grayscale to black and white**

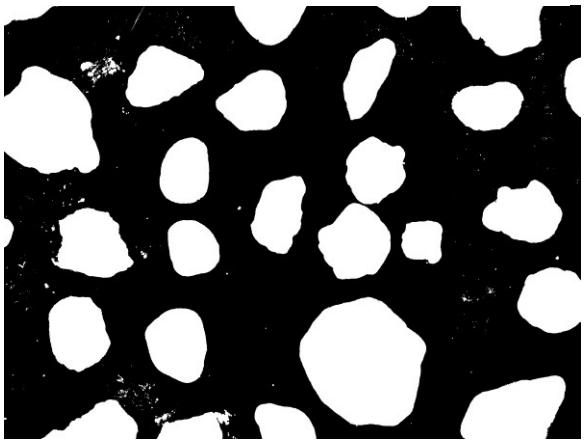

**3 – Remove "holes" from inside of objects**

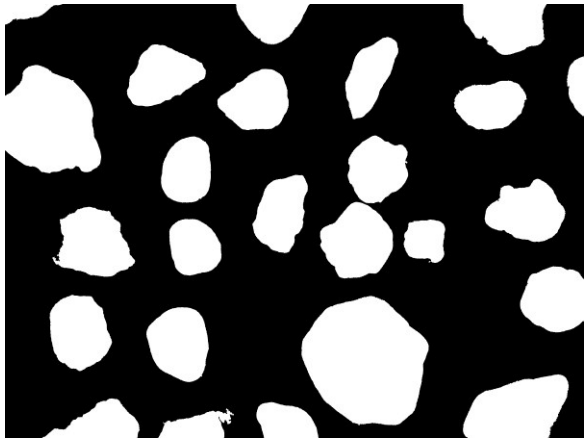

**4 – Remove very small objects**

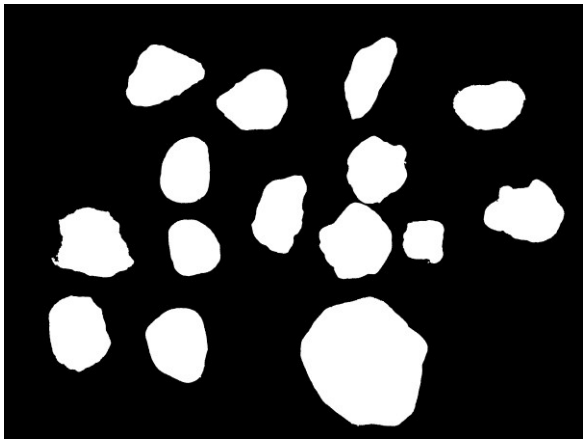

**5 – Clear borders of image**

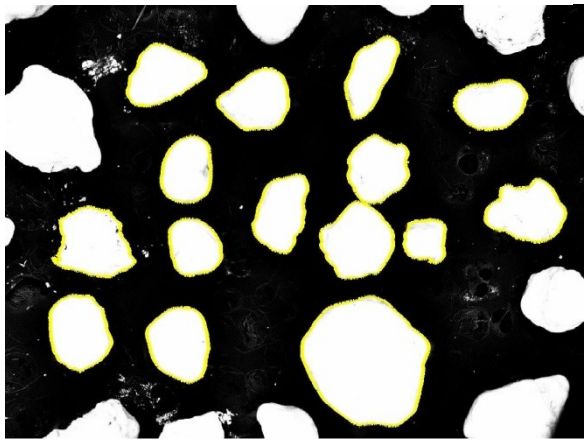

**6 – Trace borders of particles (shown on original image)**

Figure 5-2: Form/Angularity Image Analysis Process

In step 3, removal of “holes” refers to the black spots within a sand particle. However, also due to the very high contrast rates, the sand particle surfaces showed very little relief and therefore very few “holes”. Nevertheless, this step still had to be taken in order for the rest of the program to function properly. In this step, the program searched for any black pixels that could not be reached by tracing other black pixels from any point on the picture boundary.

The next step involved the removal of objects that are too small to be analyzed from the image. For the most part, this is the removal of small pieces of dust and grit that accidentally ended up on the stub. Additionally, this step also eliminates particles that are not captured at a high enough resolution for proper form and angularity analysis.

Masad et al. (2001) and Fletcher et al. (2002) both stated the need to capture images at a proper resolution; it is essential when examining particle boundaries to obtain a truly accurate estimate of the boundary, in order to ensure accurate shape factor results. Masad et al. (2001), Fletcher et al. (2002) all suggested a resolution that would ensure a minimum of 100 pixels for the smallest diameter of the particles being imaged.

To take this minimum into account, a simple calculation was used. If the minimum diameter is 100 pixels, then this equates to a particle with an area of 7850 pixels. All objects in the photo that were smaller than 7850 pixels were discarded from the analysis in step 4. This is not an exact method, as not all particles were perfectly round; however for the majority of the sand particles analyzed, this method was sufficient, as they do not differ greatly from a circular shape.

The next step of the image preparation process was the removal of sand particles not completely contained within the photo. This is of course done to avoid analyzing false shapes that are outlined by the border of the photo.

In the final step of the image analysis, the boundaries of the objects remaining in the photo were traced and saved as an array of X and Y coordinates. These X and Y coordinates were then used in the computation of the various particle shape factors.

### 5.4.2 Texture

Texture measurements are significantly more tedious, both the method to obtain images, as well as while analyzing the images within MatLab. The process started in the same way as for

angularity and form measurements, with the analysis of a high contrast image collected with the SEM detectors in backscattered electron mode. This image was analyzed to determine the boundaries of particles, which were then mapped onto a second image of the exact same frame. This second image was captured in secondary electron mode however, and contained much more detail of actual surface texture than the image captured in backscatter mode. This process is illustrated in Figure 5-3.

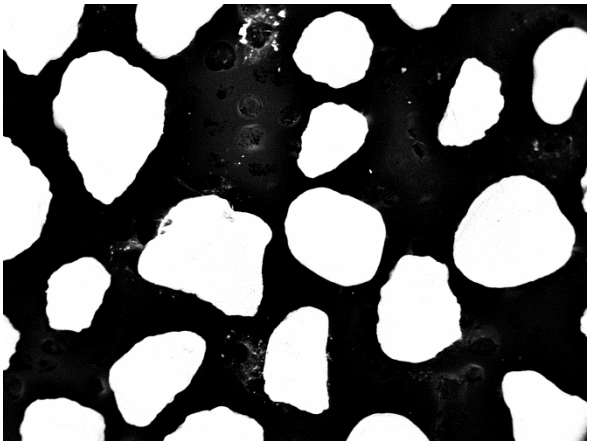

**1 – Original image captured in backscatter mode**

**2 – Processed image for boundary detection**

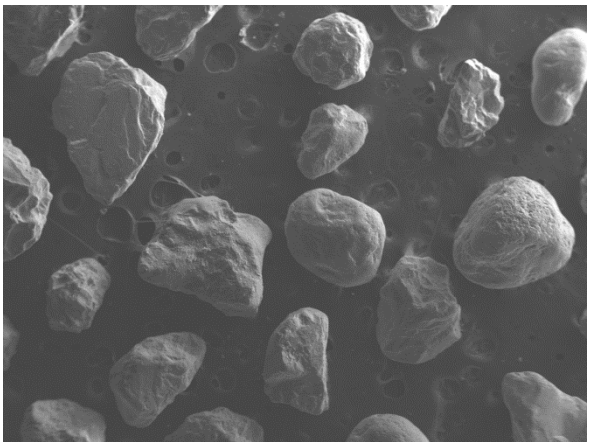

**3 – Original image captured in secondary electron mode**

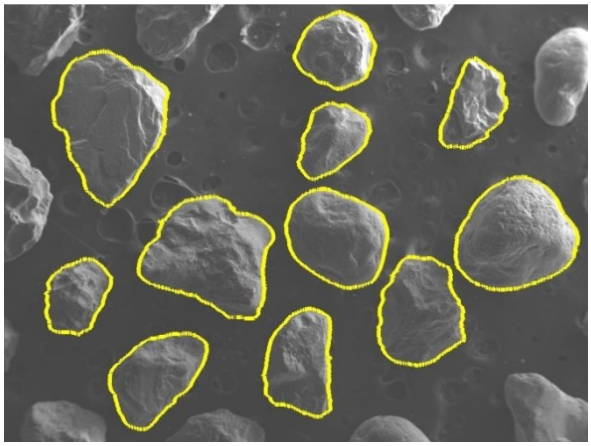

**4 – Secondary electron image with particle boundaries overlaid**

Figure 5-3: Texture Image Analysis Process

This process was tedious but it combined the best aspects of each image gathering method. Boundary detection was easy to do with images collected at very high contrast using backscattered electrons, but shows very little of the actual surface texture. Secondary electron mode allowed excellent surface detail to be gathered, but cannot easily

differentiate particle boundaries. The combination of methods allowed a reliable measure of texture.

Once the boundaries had been detected, the area contained within each particle boundary could be analyzed for texture. As discussed in section 2.2.3.6.3, each pixel within the boundary had an intensity value from 0-255 associated with it that determined the brightness of that pixel. By analyzing the distribution of intensity values within a particle, a relative measure of texture could be found. A higher standard deviation of pixel intensity for a particle equated to a more rugged texture.

### 5.4.3 Issues with Texture Measurements

In order to obtain a suitable signal to noise ratio for a clear photo, a slow scan speed was required, which could cause issues while in secondary electron mode when particles build up a charge. This is illustrated in Figure 5-4, where two sand particles, one in the lower left side and one in the upper middle exhibit bright white portions. This would drastically effect texture calculations for those particles, as the bright white would falsely increase the standard deviation of intensity, and therefore the perceived texture. These issues can be solved by integration of multiple frames captured at higher scan speeds. This method was applied by the author with some success; however the texture calculation by greyscale histogram method still is tedious and subject to errors due to lighting.

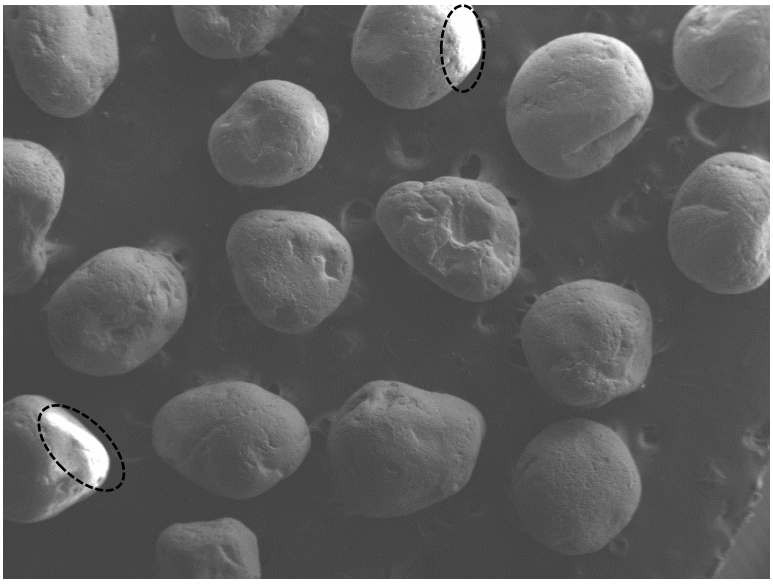

Figure 5-4: Image of Cube Mould Test Sand Particles Illustrating Particle Charge Build Up

# 6 Results & Discussion

## 6.1 Introduction

Chrome carbide samples were subjected to four, 10 minute duration abrasive wear tests for a total of 40 minutes of abrasive wear. Every effort was taken during the test to ensure measurements of mass loss would accurately reflect loss from the abrasive wear test without any external influences.

Sampled sand particles were imaged with a Zeiss EVO MA15 scanning electron microscope. Images were analyzed using programs developed with MatLab to determine form factor, form index, convexity, angularity index, angularity parameter, spike parameter quadratic fit, as well as particle texture. These parameters were analyzed to determine correlation with wear rate, as well as with angle of repose.

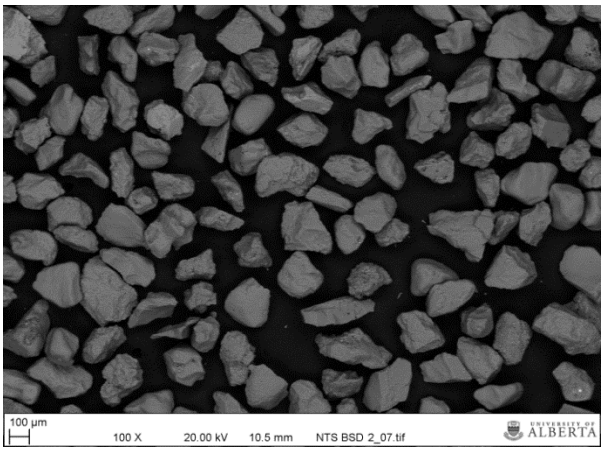


Beach Tailings Sand

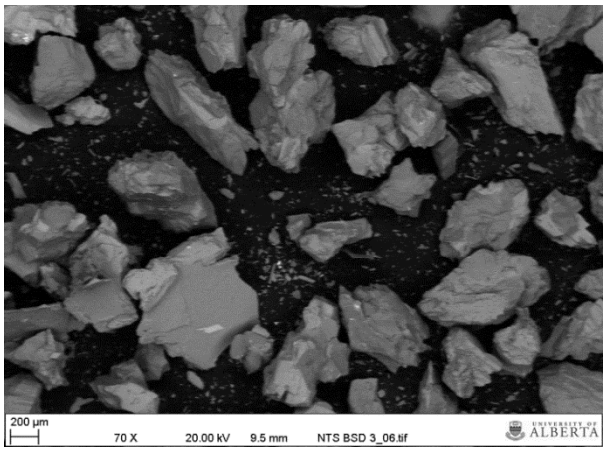


Granite Sand

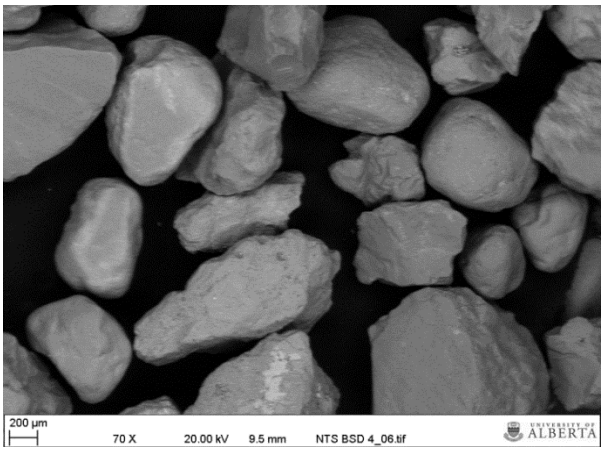


Raw Oil Sand

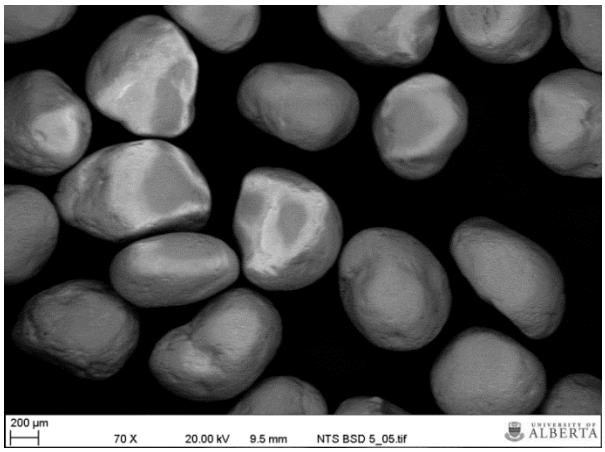


Silica Sand

Figure 6-1: SEM Images of Sand Particles

The angle of repose for each material type was measured to determine what application it may have to abrasive wear rates and texture measurements. It was thought that a good measure of overall particle 'roughness' could be estimated by how efficiently particles would stack onto each other, and therefore how steep the angle of repose would be.

Finally, energy expended by the testing apparatus motor during the test was also monitored through the duration of all tests to facilitate specific energy calculations. Specific energy was related to material and media properties, the relationship that these properties have is discussed and some shortcomings are highlighted.

## 6.2 Particle Shape Characteristics

In order to obtain an accurate average for each particle parameter despite the relatively rough sampling methods, it was attempted to analyze approximately 500 particles of sand for each type. This was not done via an exact method, but rather a rough estimation based on the average number of particles that could be prepared for imaging on a single SEM stub. Total number of each particle type form and angularity analysis is summarized in Table 6-1.

Table 6-1: Number of Particles Analyzed for Form and Angularity Parameters

| | |
|---|---|
| Tailings Beach Sand | 677 |
| Granite Sand | 524 |
| Raw Oil Sand | 685 |
| Silica Sand | 477 |

Texture analysis was a much more time consuming process however, requiring the switch back and forth between secondary electron and backscatter mode which was typically accompanied by the need to fine tune the focus and scan times with each change. For this reason, the number of particles analyzed for texture was significantly reduced; however enough particles have been included to obtain a reasonable estimate of the overall average. Number of particles imaged for texture analysis is shown in Table 6-2

Table 6-2: Number of Particles Analyzed for Texture Parameter

| | |
|---|---|
| Tailings Beach Sand | 150 |
| Granite Sand | 104 |
| Raw Oil Sand | 104 |
| Silica Sand | 93 |

Fletcher et al. recommend the use of statistical analysis of angularity distribution, rather than just the average values to gain more understanding of the relationship between

angularity and performance (Fletcher et al., 2002). For this reason a frequency line graph of the results has also been included to provide a better awareness of the complete distribution of particle shape and influences on the overall average for each of the particle characteristics measured. For the sake of clarity, additional histogram of results by individual sand type have been included in Appendix A

### 6.2.1 Form Parameters

#### *6.2.1.1 Form Factor*

Form factor is a measure of how far a particle deviates from an ideal circle. It is equal to 1 for a circle, and is increasingly less than one for increasingly "uncircular" particles. A short numerical summary for each particle type is shown in Table 6-3.

Table 6-3: Form Factor Parameter Results

| | Beach Tailings Sand | Granite Sand | Raw Oil Sand | Silica Sand |
|---|---|---|---|---|
| **Average** | 0.450 | 0.549 | 0.700 | 0.852 |
| **Standard Deviation** | 0.140 | 0.117 | 0.120 | 0.088 |
| **Maximum** | 0.846 | 0.837 | 0.958 | 0.987 |
| **Minimum** | 0.108 | 0.165 | 0.316 | 0.457 |

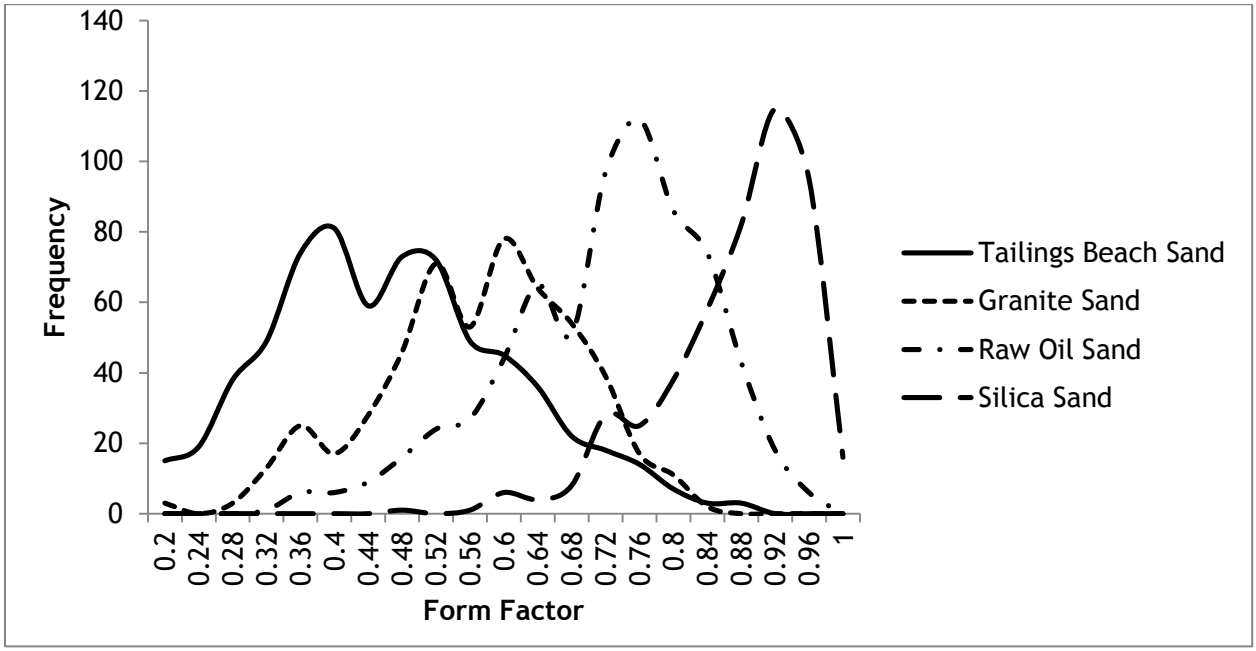


Figure 6-2: Form Factor Distribution

### *6.2.1.2 Form Index*

Form index describes the rate of change of the particle boundary at angular intervals around the entire particle. Basically the higher the number, the more irregular the overall form of the particle is. A short numerical summary for each particle type is shown in Table 6-4.

Table 6-4: Form Index Parameter Results

| | Beach Tailings Sand | Granite Sand | Raw Oil Sand | Silica Sand |
|---|---|---|---|---|
| **Average** | 2.76 | 3.64 | 2.04 | 1.34 |
| **Standard Deviation** | 0.75 | 1.09 | 0.64 | 0.42 |
| **Maximum** | 6.51 | 14.11 | 5.32 | 3.30 |
| **Minimum** | 1.08 | 1.79 | 0.60 | 0.59 |

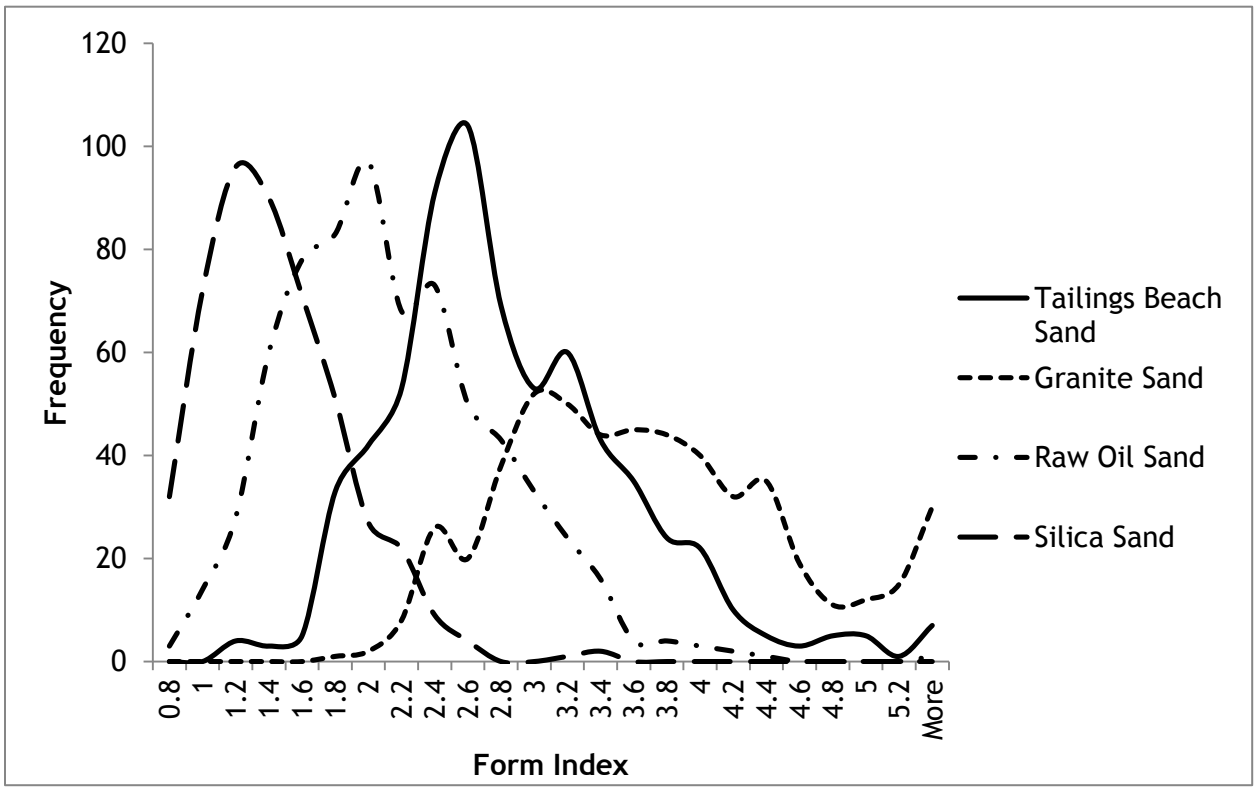


Figure 6-3: Form Index Distribution

### 6.2.2 Angularity Parameters

#### *6.2.2.1 Angularity Index*

Angularity index measures the departure of a particle boundary away from the boundary of an equivalent ellipsoid. A higher number refers to a larger departure from the idealized boundary, and therefore a more angular particle. A short numerical summary for each particle type is shown in Table 6-5.

Table 6-5: Angularity Index Parameter Results

| | Beach Tailings Sand | Granite Sand | Raw Oil Sand | Silica Sand |
|---|---|---|---|---|
| **Average** | 54.34 | 58.95 | 45.45 | 18.32 |
| **Standard Deviation** | 29.64 | 26.22 | 28.77 | 8.01 |
| **Maximum** | 252.61 | 166.56 | 257.86 | 51.79 |
| **Minimum** | 10.48 | 15.93 | 6.57 | 5.76 |

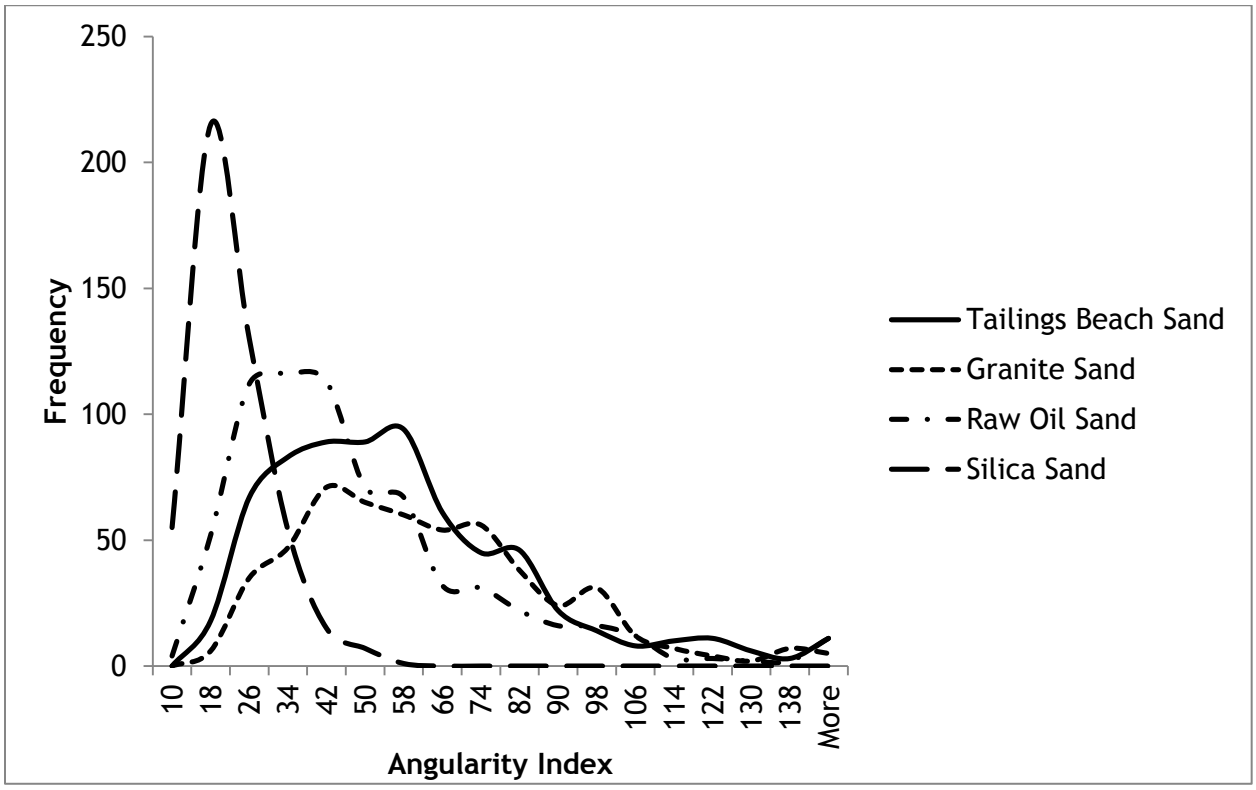


Figure 6-4: Angularity Index Distribution

### *6.2.2.2 Convexity*

Convexity is another measure of particle angularity that relies on the departure of a particle from an idealized boundary; for the convexity parameter this idealized shape is the convex polygon. A smaller convexity corresponds to a more angular particle. A short numerical summary for each particle type is shown in Table 6-6.

Table 6-6: Convexity Parameter Results

| | Beach Tailings Sand | Granite Sand | Raw Oil Sand | Silica Sand |
|---|---|---|---|---|
| **Average** | 0.965 | 0.948 | 0.981 | 0.992 |
| **Standard Deviation** | 0.014 | 0.019 | 0.010 | 0.003 |
| **Maximum** | 0.992 | 0.981 | 0.995 | 0.996 |
| **Minimum** | 0.896 | 0.862 | 0.934 | 0.974 |

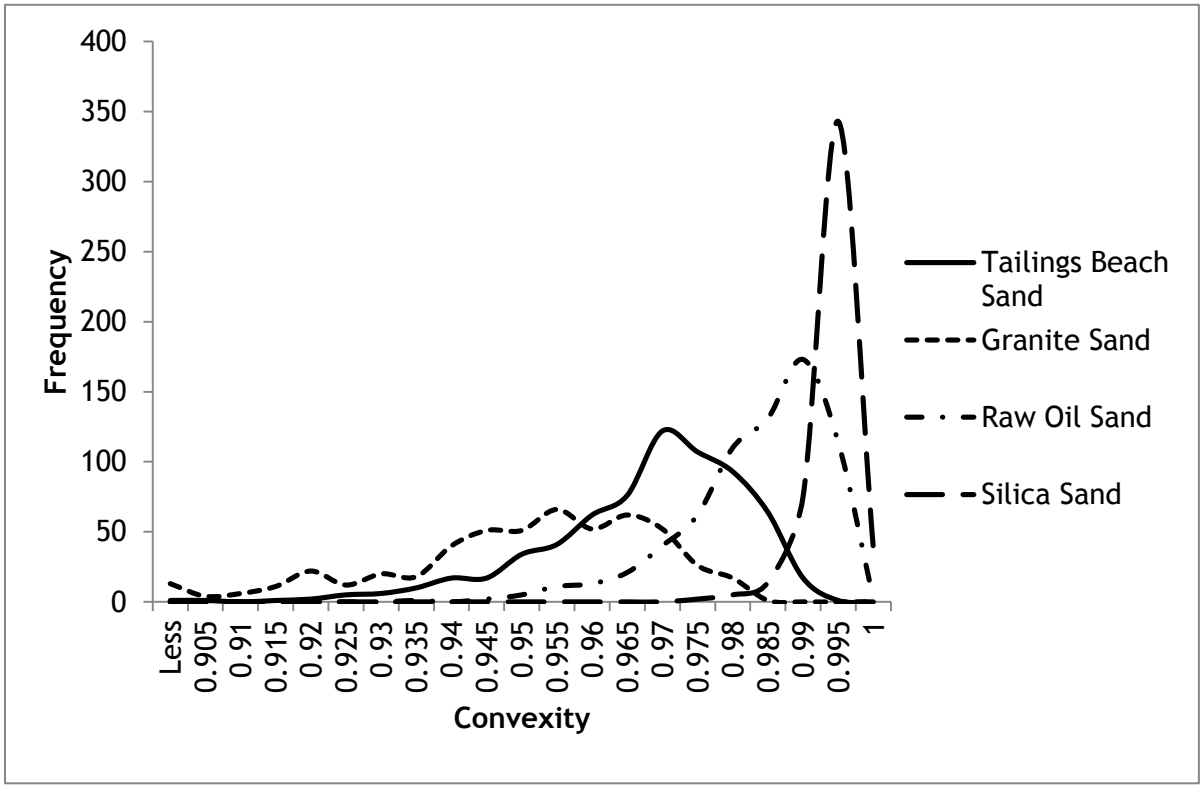


Figure 6-5: Convexity Parameter Distribution

### *6.2.2.3 Angularity Parameter*

Angularity parameter relies on the relationship between the convex polygon and the equivalent ellipsoid. A perfectly circular particle would have an angularity parameter of one, and would increase with increasing angularity. A short numerical summary for each particle type is shown in Table 6-7.

Table 6-7: Angularity Parameter Results

| | Beach Tailings Sand | Granite Sand | Raw Oil Sand | Silica Sand |
|---|---|---|---|---|
| **Average** | 1.097 | 1.127 | 1.061 | 1.027 |
| **Standard Deviation** | 0.035 | 0.045 | 0.028 | 0.009 |
| **Maximum** | 1.289 | 1.358 | 1.174 | 1.063 |
| **Minimum** | 1.030 | 1.001 | 1.007 | 1.009 |

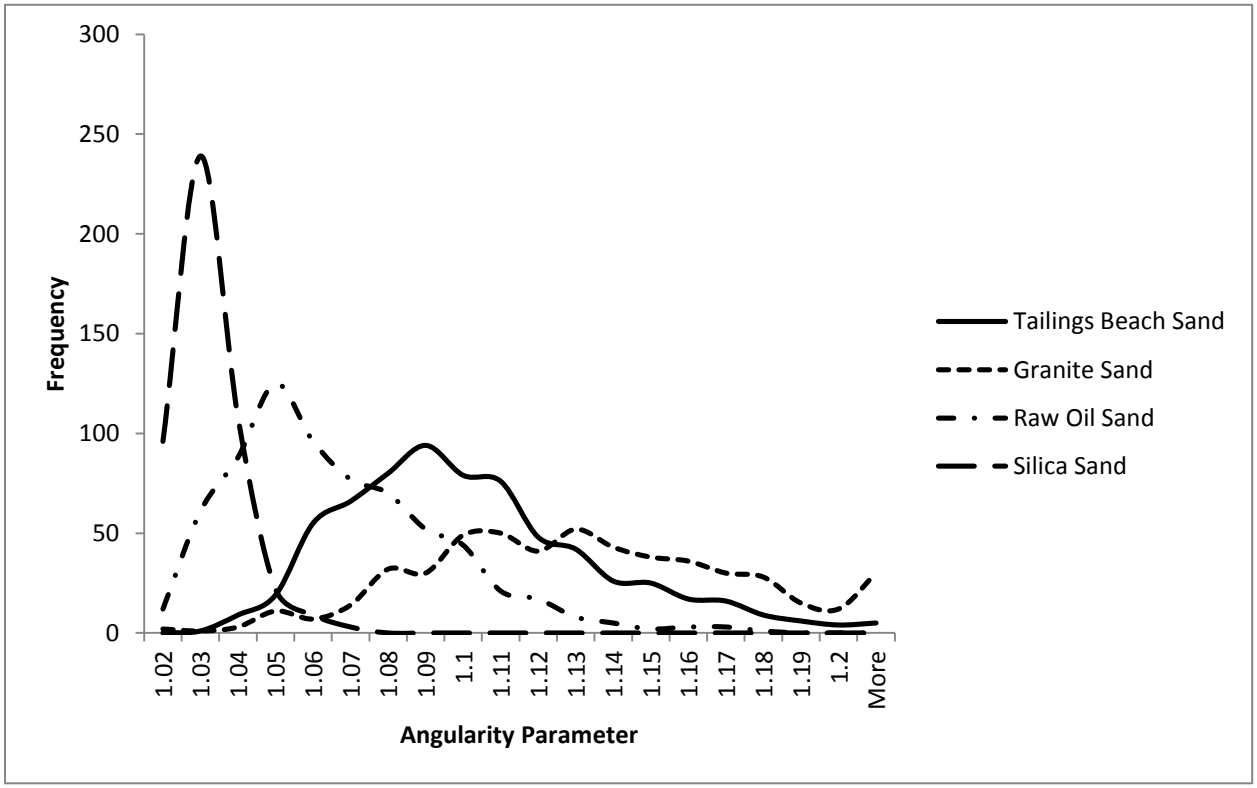


Figure 6-6: Angularity Parameter Distribution

#### *6.2.2.4 Spike Parameter Quadratic Fit*

The spike parameter, quadratic fit, relies on the protrusions of the particle outside of an equivalent circle to determine particle angularity. The angle formed by each protrusion is the basis for the parameter; the sharper the point of the protrusion, the higher the spike parameter. A short numerical summary for each particle type is shown in Table 6-8

Table 6-8: Spike Parameter Quadratic Fit Parameter Results

| | Beach Tailings Sand | Granite Sand | Raw Oil Sand | Silica Sand |
|---|---|---|---|---|
| **Average** | 0.362 | 0.505 | 0.244 | 0.104 |
| **Standard Deviation** | 0.163 | 0.165 | 0.143 | 0.060 |
| **Maximum** | 0.864 | 0.945 | 0.756 | 0.562 |
| **Minimum** | 0.023 | 0.062 | 0.018 | 0.005 |

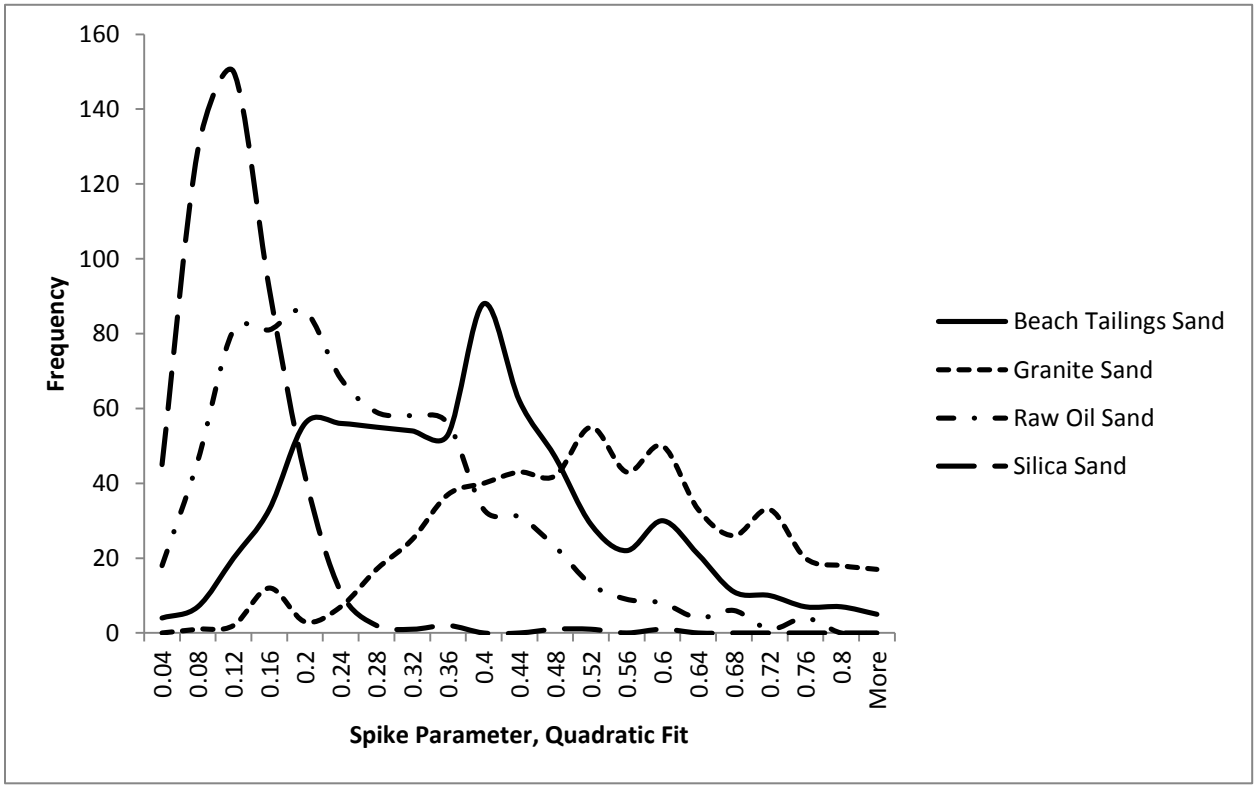


Figure 6-7: Spike Parameter Quadratic Fit Distribution

### 6.2.3 Texture

#### *6.2.3.1 Standard Deviation of Intensity*

To determine texture, the lighting intensity (on a scale of 0-255) of each pixel within a particle was analyzed. The standard deviation within a sand particle of the pixel intensity is taken as a measure of the texture of the particle; a larger standard deviation corresponds with a rougher texture. A short numerical summary for each particle type is shown in Table 6-9.

Table 6-9: Standard Deviation of Intensity (Texture) Parameter Results

| | Beach Tailings Sand | Granite Sand | Raw Oil Sand | Silica Sand |
|---|---|---|---|---|
| **Average** | 29.10 | 42.20 | 33.48 | 29.95 |
| **Standard Deviation** | 7.43 | 13.08 | 14.21 | 14.94 |
| **Maximum** | 43.34 | 72.73 | 86.15 | 67.03 |
| **Minimum** | 10.56 | 11.10 | 9.28 | 5.85 |

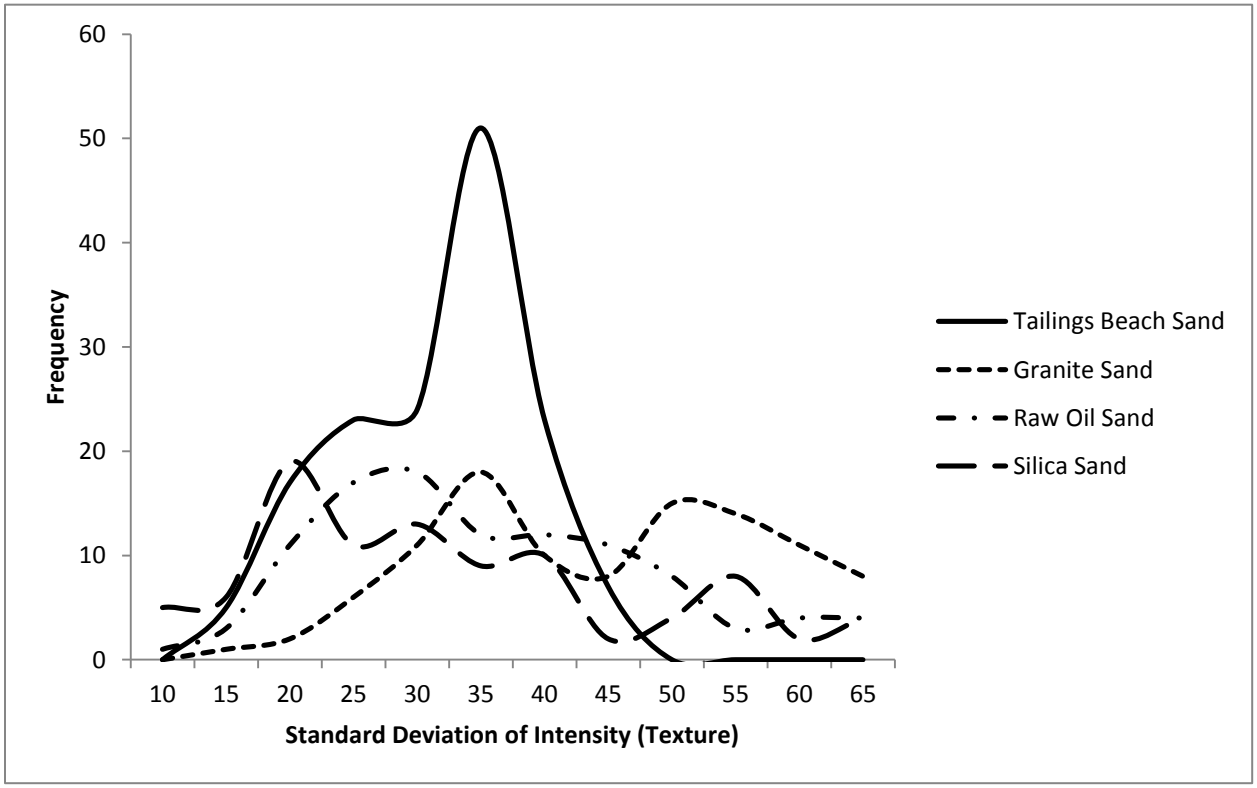


Figure 6-8: Standard Deviation of Intensity (Texture) Distribution

### 6.2.4 Summary of Particle Characteristics

It could be seen from the histograms of each shape parameter that granite sand tends to have the broadest distribution of values within each parameter, and silica sand the tightest distribution. This was to be expected as the granite sand was prepared in the lab by grinding core samples, and has not been subjected to any sorting or grading, whereas the other three types of sand have. The silica sand especially had been heavily sorted to obtain homogenous sand for scientific purposes and as such shows a very small variation within each parameter.

The raw oil sand and tailings beach sand showed, expectedly, a very similar distribution within each parameter. However, not expected was the fact that when examining angularity, the beach tailings sand exhibited higher angularity than the raw oil sand. It was thought that perhaps after undergoing refining, beach tailings sand would have lost much of its angularity to erosion, however, perhaps during the refining process the oil sand particles undergo a good deal of fracture, resulting in a more angular particle at the end of the process.

All parameters exhibited appropriate distributions to gain a good understanding by examining the averages; no parameter was greatly affected by a small number of extreme outliers.

In order to illustrate the distribution of parameters on a single graph, the averages for each parameter were converted to a normal score and separated by sand type to produce Figure 6-9. This figure basically illustrates how rough each sand type is in comparison to the other three. If a parameter falls above normal score of zero for a sand type, then the particle has above normal rugosity, according to that parameter.

The normal scores of each parameter by sand type are found using the average and standard deviation for all 2363 particles (this includes all four sand types). The process for calculating the normal scores for form factor is covered here:

1. Calculate average and standard deviation of form factor for all 2363 particles imaged (677 beach tailings sand, 524 granite sand, 685 raw oil sand, 477 silica sand particles); average=0.625, standard deviation=0.191
2. Calculate average form factor by sand type:

| | |
|---|---|
| Beach Tailings Sand | 0.450 |
| Granite | 0.549 |
| Raw Oil Sand | 0.700 |
| Silica Sand | 0.852 |

3. Determine normal score for each sand type, using the average and standard deviation calculated in step 1:

| | |
|---|---|
| Beach Tailings Sand | -0.919 |
| Granite | -0.401 |
| Raw Oil Sand | 0.391 |
| Silica Sand | 1.184 |

4. Invert the normal scores to take into account the fact that as form factor gets smaller, particle rugosity increases

| | |
|---|---|
| Beach Tailings Sand | 0.919 |
| Granite | 0.401 |
| Raw Oil Sand | -0.391 |
| Silica Sand | -1.184 |

5. Plot normal scores on a graph:

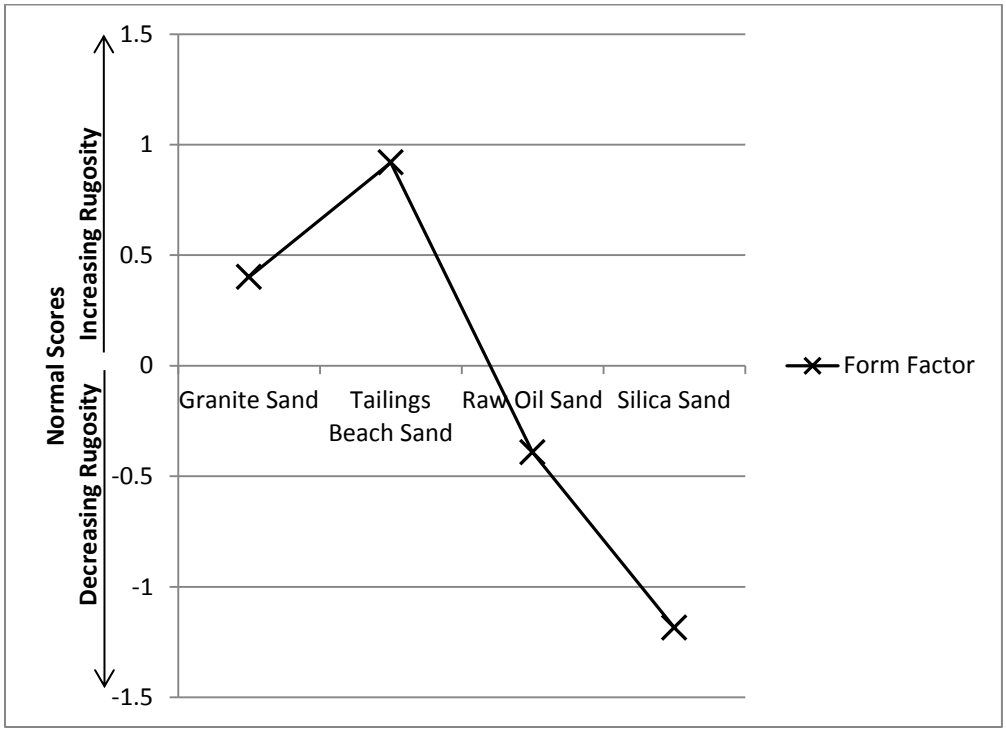


The normal scores for both form factor and convexity were inverted to take into account that as they get lower than the average, the particle rugosity generally increases. The rest of the particle parameters were calculated in the same way as steps 1-3, as they did not require inversion; Figure 6-9 illustrates how particle types rank against each other in terms of rugosity.

With the exception of form factor, all the parameters follow the same general trend. Granite sand tends to all around be the roughest, followed by tailings beach sand, raw oil sand and finally silica sand. This is consistent with visual observation, shown in Figure 6-1. It should also be noted that the images in Figure 6-1 were not used for image analysis, but rather were taken to provide a clear view of the particles themselves. Additional images taken for this purpose can be found in Appendix B

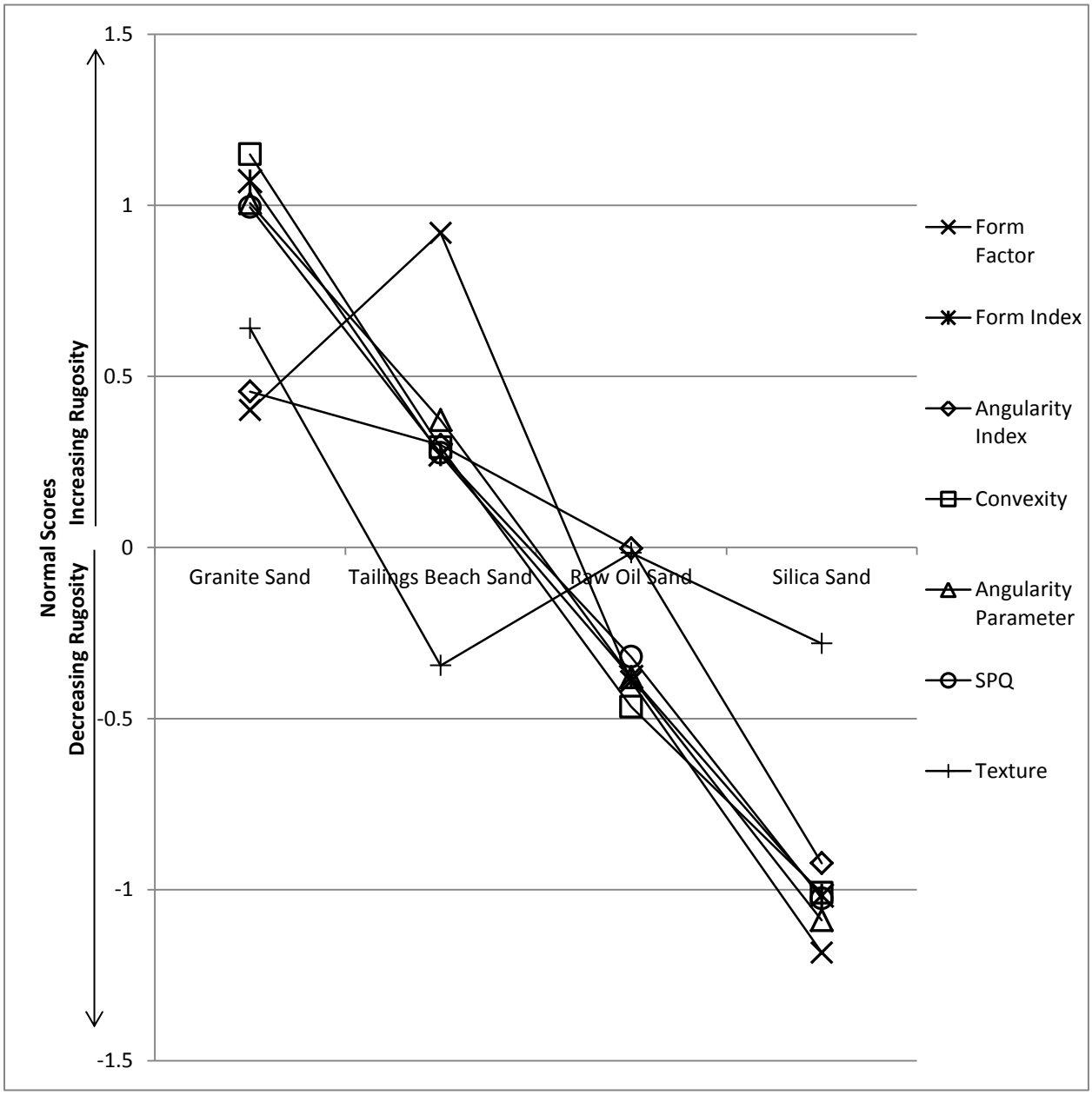


Figure 6-9: Particle Shape Parameter Normal Scores

## 6.3 Wear Tests

Chrome carbide samples were subjected to four, 10 minute long abrasion tests in the modified G65 type machine described in Chapter 4. At the end of every 10 minute test, the samples were cleaned and weighed to determine mass loss. This mass loss over time is summarized in Table 6-10 and is shown graphically in Figure 6-10. A full break down of the mass loss by sample over time can be found in Appendix C

### 6.3.1 Mass Loss

Table 6-10: Average Mass Loss of Chrome Carbide (g) During Testing, By Abrasive Material

| | | Abrasion Time (mins) | | | |
|---|---|---|---|---|---|
| | | 10 | 20 | 30 | 40 |
| Abrasive Material Type | Tailings Beach Sand | 0.0235 | 0.0404 | 0.0368 | 0.0619 |
| | Granite Sand | 0.1556 | 0.2860 | 0.4141 | 0.5241 |
| | Raw Oil Sand | 0.1124 | 0.1970 | 0.2657 | 0.3746 |
| | Silica Sand | 0.0539 | 0.0905 | 0.1491 | 0.1912 |

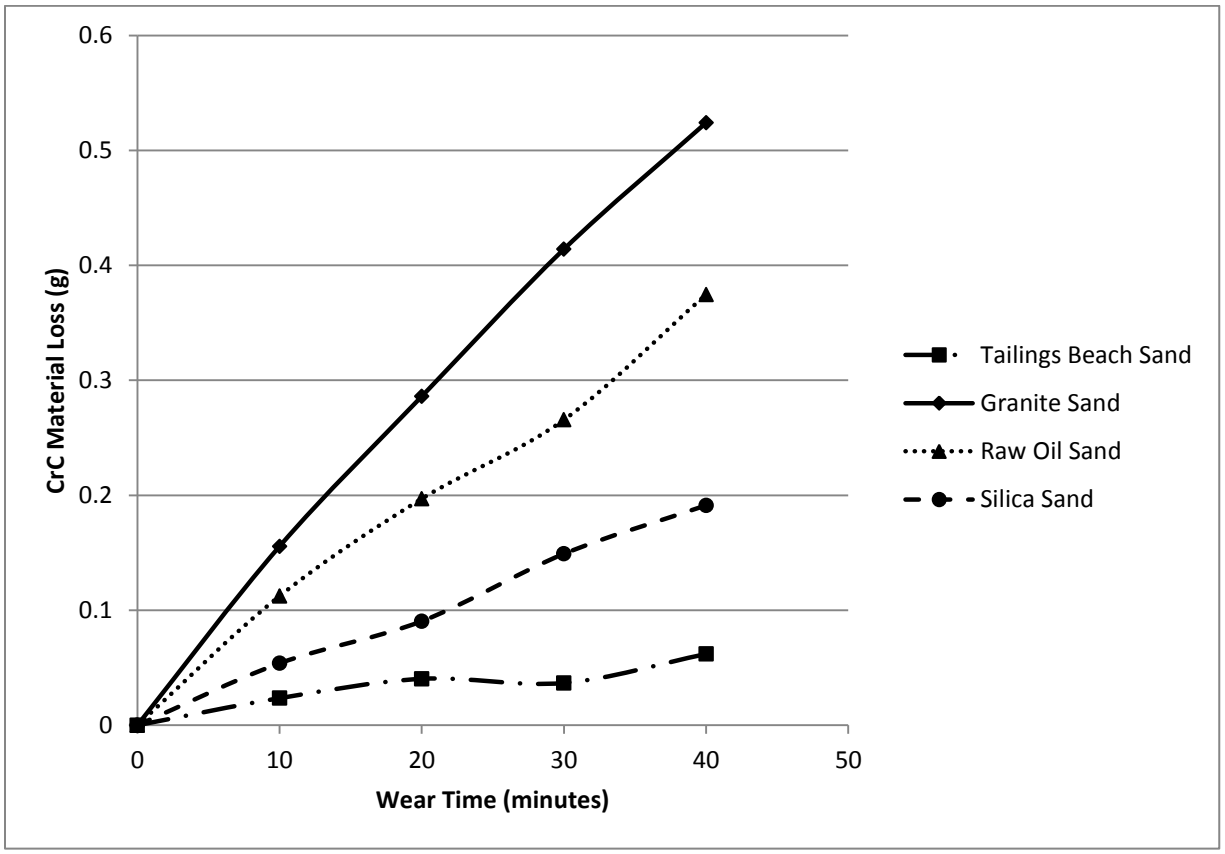


Figure 6-10: Chrome Carbide Mass Loss by Abrasive Material Type

The G65 standard test requires material loss to be described in terms of volume lost to facilitate correlation between materials of different mass. As the density of the actual chrome carbide portion of the sample that is subject to abrasion depends on dilution, which is heavily dependent on welding parameters, an estimation of 6.87 grams/$cm^3$ has been used to calculate volume loss, shown in Table 6-11.

Table 6-11: Chrome Carbide Volume Loss by Abrasive Material Type, 40 Minutes of Abrasion

| | Chrome Carbide Material Loss ($mm^3$) |
|---|---|
| Tailings Beach Sand | 0.901 |
| Granite Sand | 7.621 |
| Raw Oil Sand | 5.447 |
| Silica Sand | 2.781 |

In terms of rugosity, the wear scars produced during the testing closely follow the abrasive loss graph, with granite producing the roughest scar, followed by the raw oil sand. The silica sand and tailings beach sand both produced very minimal wear scars, doing little more than polishing the samples. Wear scars can be seen in Figure 6-11.

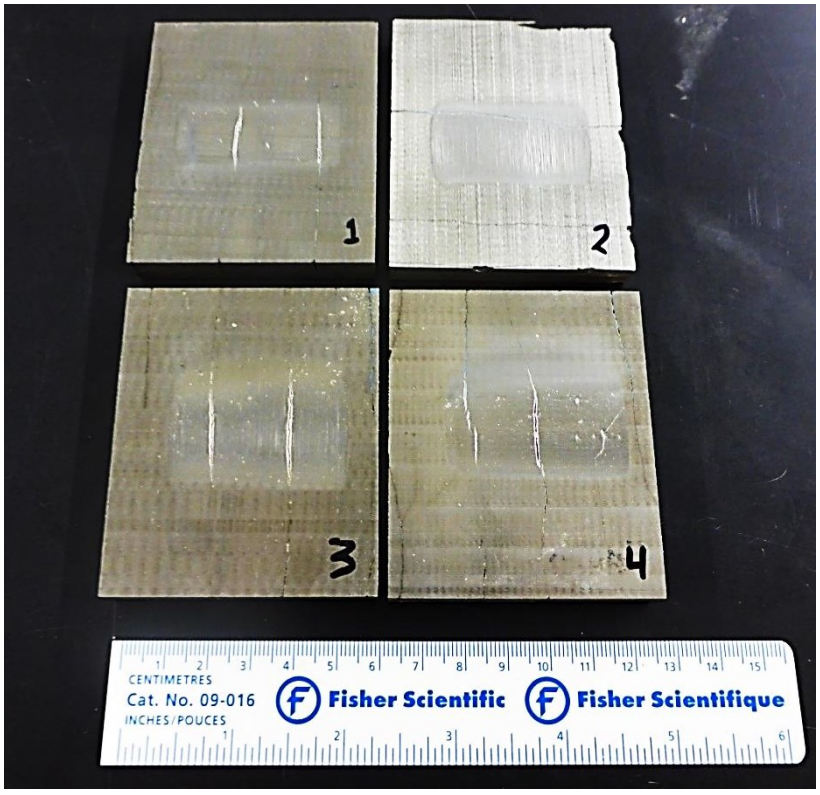


Figure 6-11: Wear Scars;Sample 1-Beach Tailings Sand, Sample 2-Granite Sand, Sample 3-Raw Oil Sand, Sample 4-Silica Sand

### 6.3.2 Wear Scar Analysis

When the actual wear scars were examined, it became clear that two of the mechanisms of abrasive wear were present: cutting and grain pull-out. Full page images of the wear scars for each type of abrasive, taken with a standard camera can be found in Appendix C

In the more abrasive media (granite and raw oil sand), relatively deep cutting was clearly present. Additionally, large pits could be seen with the naked eye, likely representing a spot where a carbide particle was pulled out from the matrix material. As discussed in section 2.2.5 granite sand was expected to cause the largest amount of preferential wear of the matrix material. This preferential wear of the matrix material would increase the likelihood of grain pull-out occurring, explaining why that failure mode is so prevalent in the samples abraded by granite sand. In the sample abraded with silica sand, only extremely faint striations were present to suggest that the abrasive mode of cutting was involved. Much more prevalent is fairly significant pitting of the surface, suggesting that grain pull-out was the mode responsible for much of the actual mass loss in samples abraded by silica sand.

Even in the samples from tests of the least abrasive material type (tailings beach sand), extremely small pits were still visible. When viewed with the help of a SEM, it became clear that the majority of these pits are formed on the carbide portions of the sample. Figure 6-12 and Figure 6-13 are provided as a sample images of a chrome carbide sample abraded with tailings beach sand for 40 minutes. This image was captured with the SEM in backscatter mode, which clearly shows the carbides (darker portions). Figure 6-13 is an image of the same frame as Figure 6-12, but with the SEM in secondary electron mode. This provided a better view of the surface topography of the sample, post testing. It can clearly be seen that fractures in the carbide particles provided a foundation that allowed for grains to pull out. Additionally, though not clearly visible, preferential wear of the matrix material surrounding carbides is visible in Figure 6-13, which if tests were conducted for longer periods of time would likely lead to much larger grains detaching from the matrix material.

Also visible in Figure 6-13 are small striations caused by the cutting action of the tailings beach sand grains. These striations were hardly visible to the naked eye, but this result suggests that the abrasion mode of cutting may still have been present in samples abraded by silica sand.

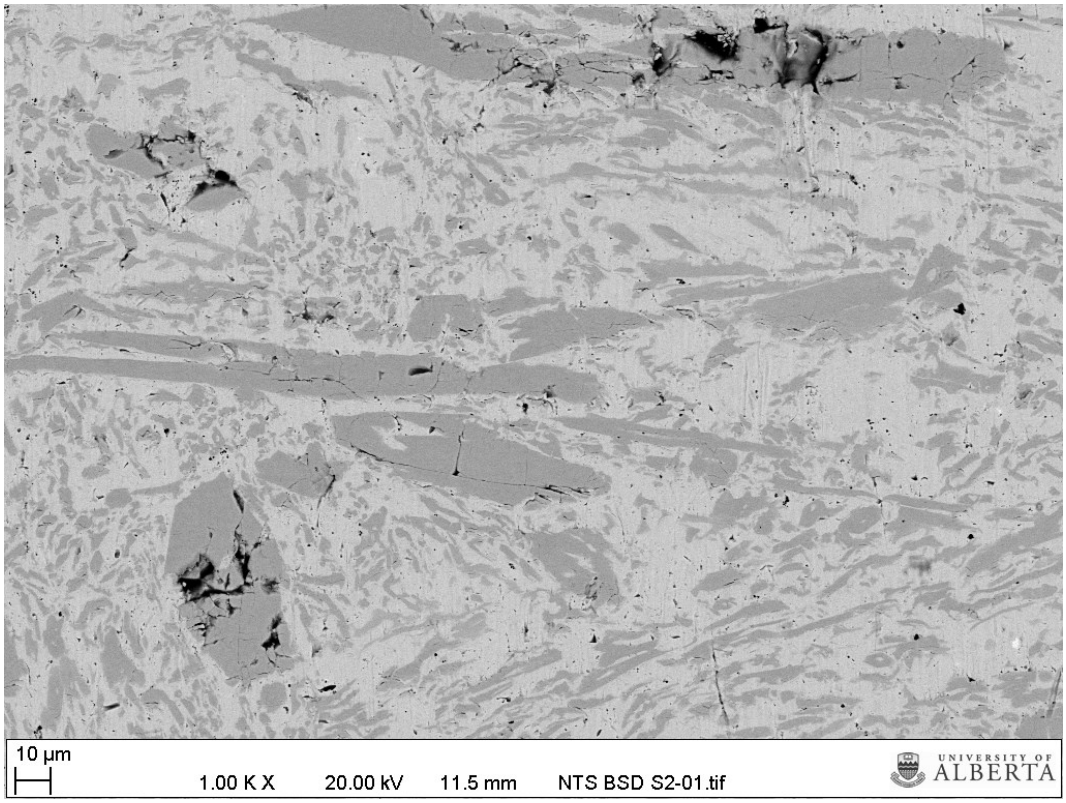


Figure 6-12: Backscattered Electron Image Illustrating Distribution of Carbides

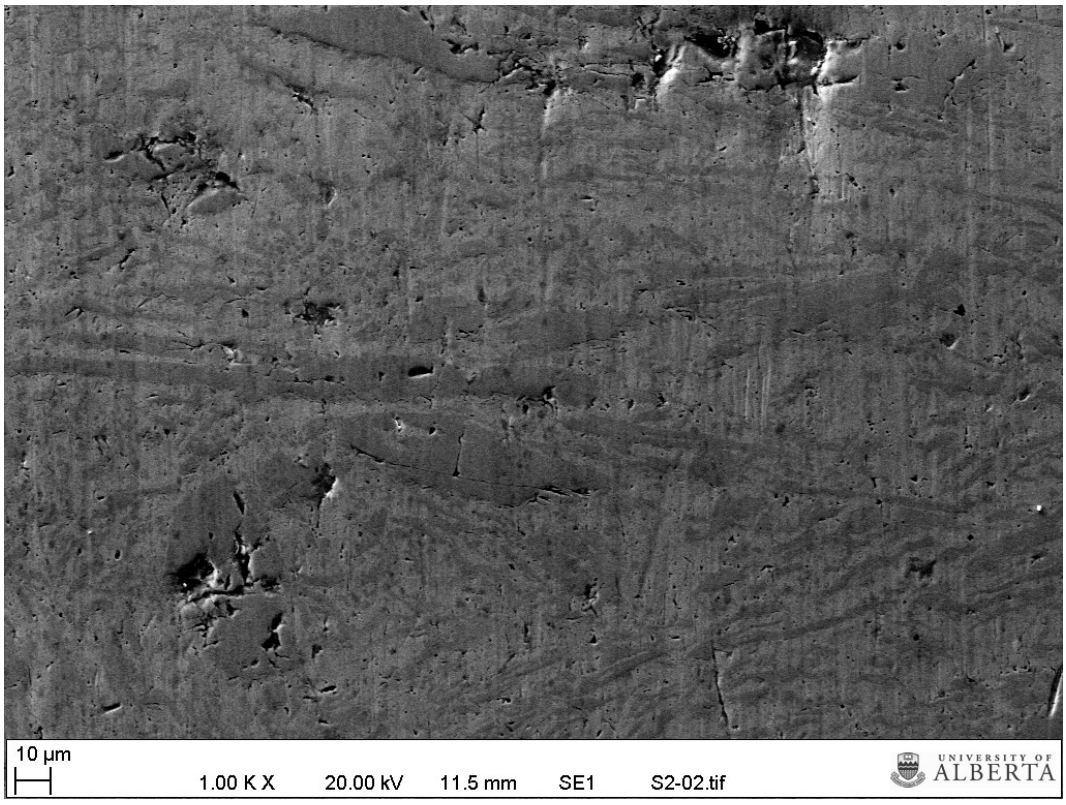


Figure 6-13: Secondary Electron Image of Chrome Carbide Sample Illustrating Grain Pull-out

### 6.3.3 Summary of Wear Tests

The granite sand, raw oil sand and silica sand all followed the general trend expected when particle shape is taken into account; the more angular the particle, the higher the abrasive wear rate. However, the tailings beach sand did not follow this same relationship. In nearly every category of particle shape measurement, tailings beach sand was the second most rugged, and yet it still produced by far the lowest wear rate. The raw oil sand and tailings beach sand consisted of the same mineralogical constituents, the only real difference being particle size and shape. No other parameters were changed, so this unexpected low abrasive wear mass loss result was likely due to some intrinsic particle property, which in the author's opinion was likely the particle size effect, as discussed in section 2.2.3.2.

#### *6.3.3.1 Influence of the Particle Size Effect on Testing*

While some sources state the particle size effect only begins to reduce wear rates at particle sizes under 100 μm, it has however has been noted to still have an effect (albeit reduced) in erosion to austenitic steel (Coronado, 2009) at sizes of up to 200 μm, which has been added to the particle size graph below as a red line. The majority of the tailings beach sand particles fell well below this "critical size" line, and as such could be suspected of reduced wear rates due to this.

In Coronado's work, particle size change from 150 μm to 200 μm showed less change in mass loss rate than they did from 50 μm to 100 μm, however they were still noticeable. Work done by Clark, 1991, also showed evidence of the particle size effect in the range of 150 μm to 180 μm when examining erosion rate for sand and oil slurries.

Coronado's work utilized austenitic steel, and Clark's used four different types of casing steels. These types of steel do not especially closely represent chrome carbide; however, they are closer to chrome carbide than the softer materials often used in abrasive tests that have investigated particle shape properties. It is very plausible that the particle size effect is heavily influenced by material hardness, and in the chrome carbide samples used for these tests perhaps the critical particle size was higher than normally reported. Additionally, the chrome carbide samples used in these tests were ground smooth before testing through the use of a surface grinding machine; this may have created a work hardened layer before abrasive testing began that further compounded the effect of the abrasive particle size.

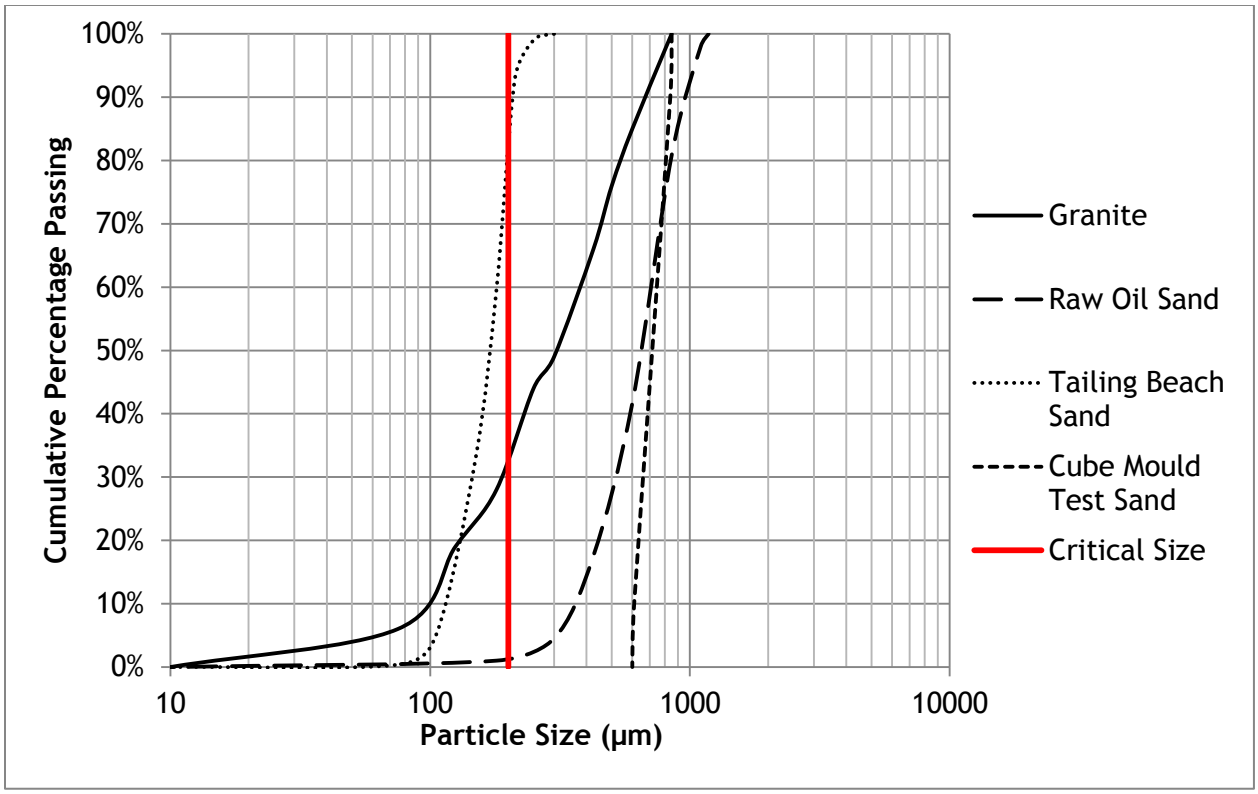


Figure 6-14: Particle Size Distribution Showing "Critical Particle Size"

## 6.4 Angle of Repose

The method to quantify texture of particles through the use of SEM images by the author was tedious, required highly specialized and expensive equipment, and even then was subject to errors from lighting conditions or focus. It was hoped that a more simple way to determine an estimate of surface texture could be found by measuring the angle of repose for each material type. Angle of repose measurements were conducted with thoroughly air-dried sand, at a temperature of 19°C, and relative humidity of approximately 30%.

It should be noted that in the field, with the bitumen content intact, oil sand would display significantly higher angles of repose. In fact, all materials would display vastly different angles of repose, depending upon field conditions such as moisture content. However, the purpose of measuring angle of repose in this situation was to replace texture type direct particle measurements with an easier, indirect method. In order to measure actual inter-particle frictional forces, which were thought to be directly proportional to surface texture, meant that all other influences needed to be avoided including the bitumen fraction of oil sand.

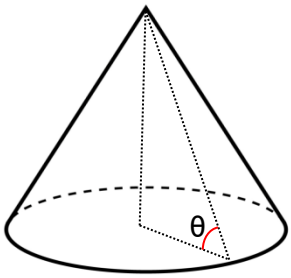


Figure 6-15: Angle of Repose

The angle of repose was found by pouring each sand type through a funnel in order to form a cone of known diameter. The height of the cone was measured, and the angle of repose determined for each sand type. Table 6-12 shows the average angle of repose, taken as an average of measurements from three different trials.

Table 6-12: Angle of Repose of Abrasive Material

| | Angle of Repose (°) |
|---|---|
| Beach Tailings Sand | 29.9 |
| Granite Sand | 36.9 |
| Raw Oil Sand | 31.7 |
| Silica Sand | 30.1 |

## 6.5 Correlation

The main goal of this work was to determine what, if any, correlation existed between measured particle shape parameters and abrasive wear rates in a situation that was representative of actual field abrasive conditions. Additionally, it was hoped that simply using the angle of repose of a material would be another method to quantify the shape of a particle. The focus of this section is determining which parameters performed best as indicators of abrasive wear and determining what, if any, correlation existed between angle of repose and particle shape parameters.

The following sub-section illustrates correlation between shape factors and abrasive wear rate. Shape factors for all four sand types have been included, however it can quickly be seen that very little correlation exists.

### 6.5.1 Abrasive Wear and Shape Factors

The correlation of only two shape factors, form factor and angularity parameter (Figure 6-16 and Figure 6-17) are shown below as an example. The remainder of the shape factor

correlations can be found in Appendix E but all showed a similar low correlation between shape parameters and abrasive wear rate. Interestingly, the texture parameter measured showed a reasonable correlation with abrasive wear rate, as shown in Figure 6-18.

In all cases with low correlation, it appeared that the lowest abrasive mass loss value (the one associated with tailings beach sand) is the major outlier. If this parameter is discounted as an outlier, all shape factors became much better predictors of abrasive wear, as shown in section 6.5.2.

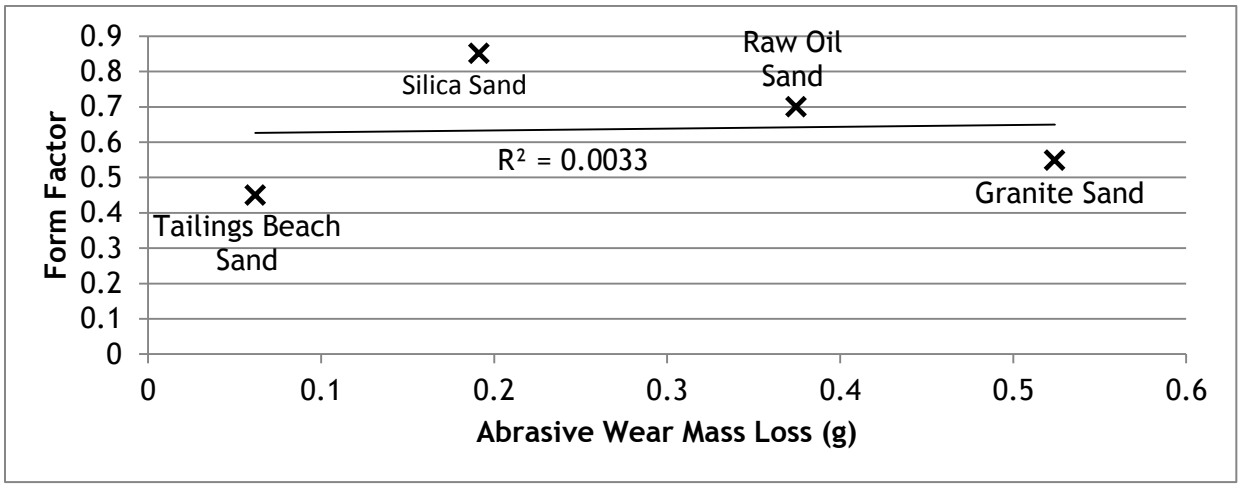


Figure 6-16: Form Factor vs Abrasive Wear Mass Loss and Correlation

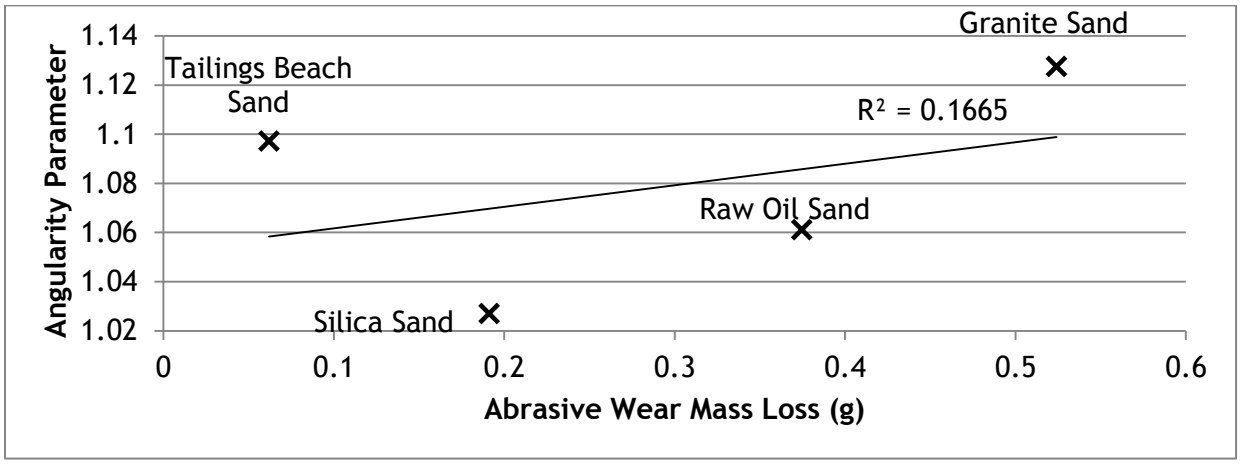


Figure 6-17: Angularity Parameter vs Abrasive Wear Mass Loss and Correlation

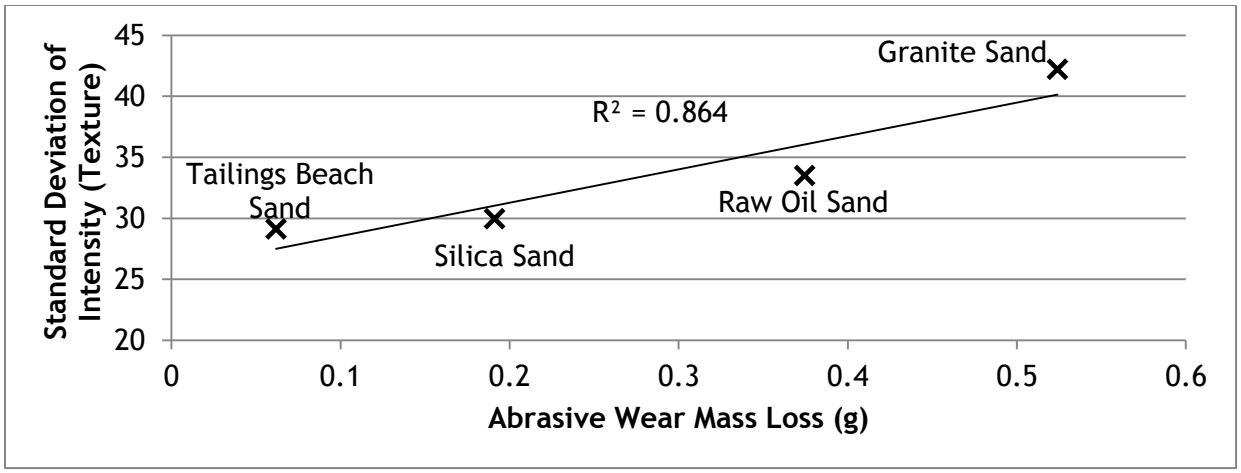


Figure 6-18: Standard Deviation of Intensity (Texture) vs Abrasive Wear Mass Loss and Correlation

### 6.5.2 Abrasive Wear and Shape Factors after Discounting Tailings Beach Sand

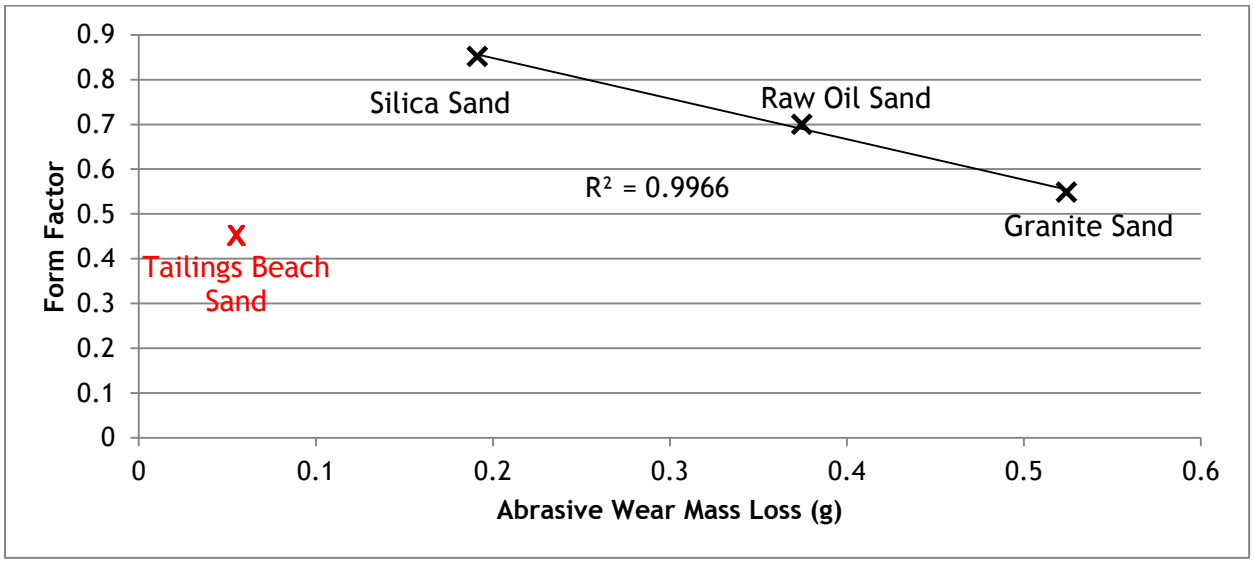


Figure 6-19: Form Factor vs Abrasive Wear Mass Loss and Correlation after Eliminating Tailings Beach Sand

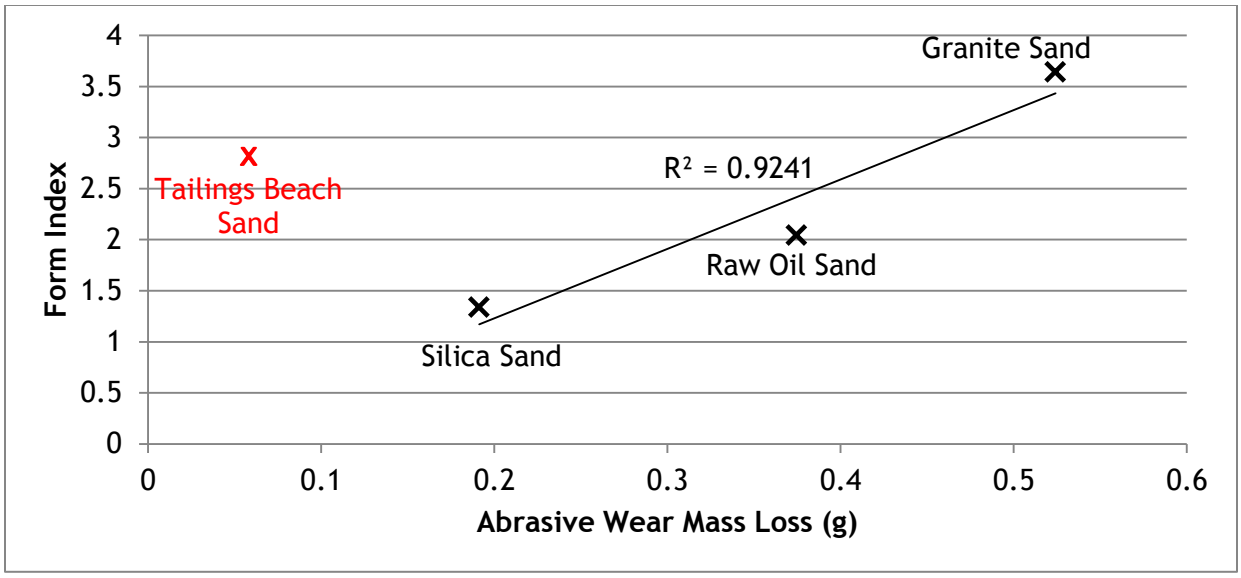


Figure 6-20: Form Index vs Abrasive Wear Mass Loss and Correlation after Eliminating Tailings Beach Sand Data

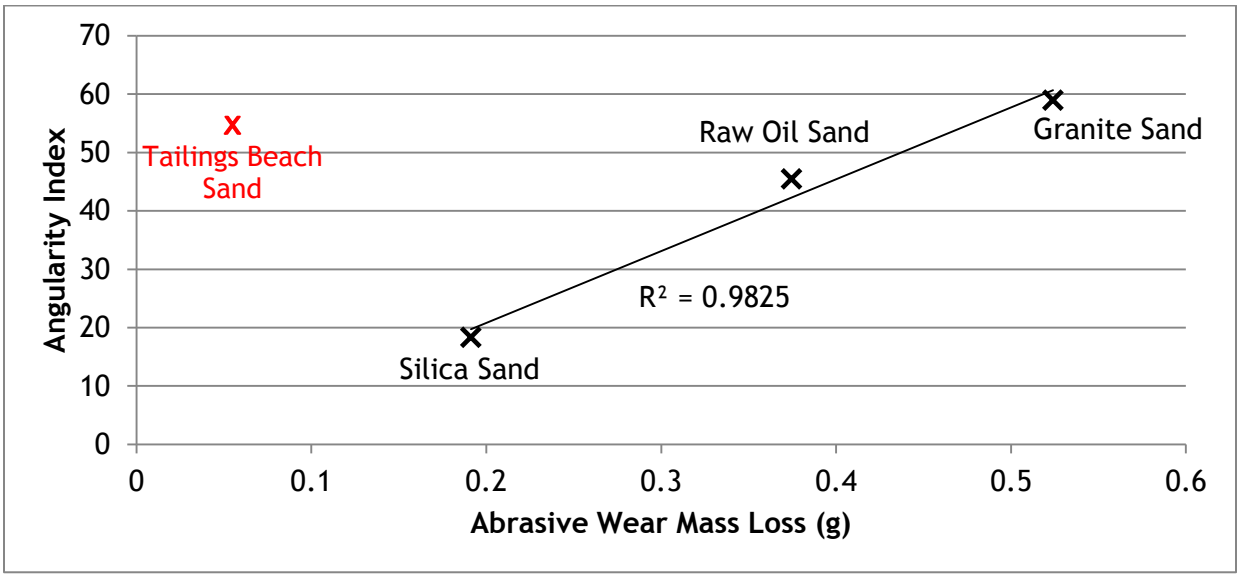


Figure 6-21: Angularity Index vs Abrasive Wear Mass Loss and Correlation after Eliminating Tailings Beach Sand Data

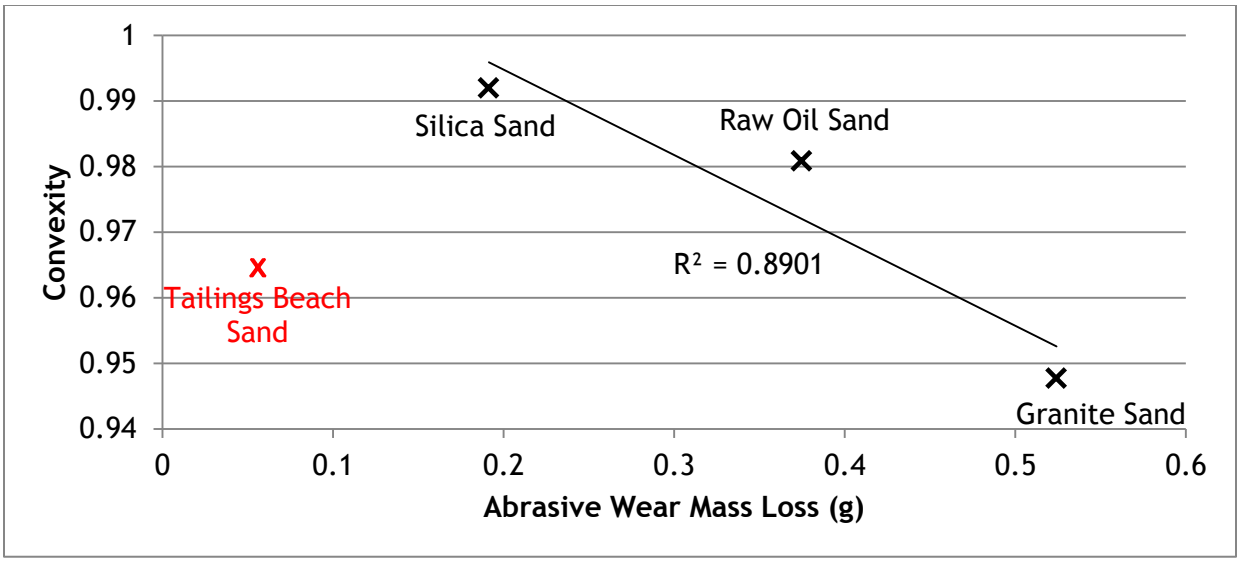


Figure 6-22: Convexity vs Abrasive Wear Mass Loss and Correlation after Eliminating Tailings Beach Sand Data

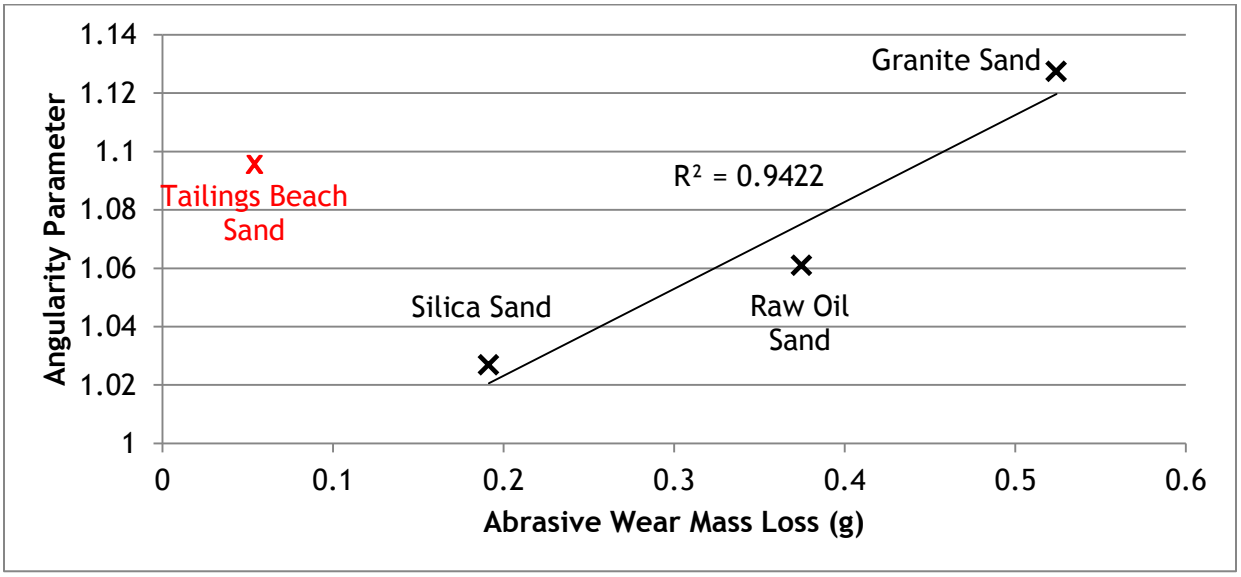


Figure 6-23: Angularity Parameter vs Abrasive Wear Mass Loss and Correlation after Eliminating Tailings Beach Sand Data

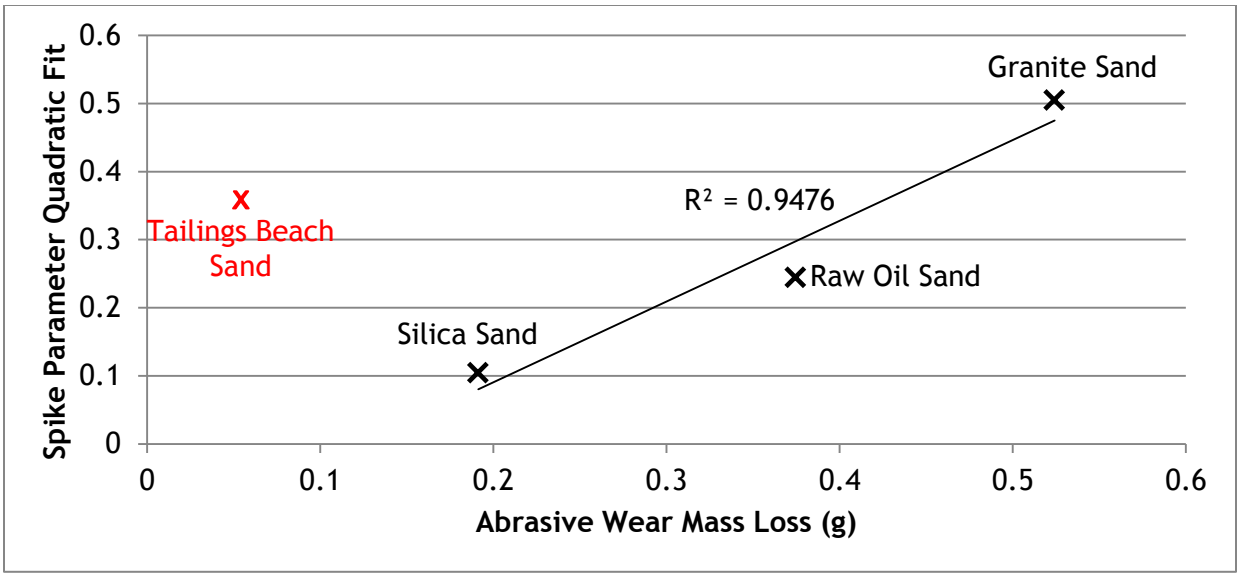


Figure 6-24: Spike Parameter Quadratic Fit vs Abrasive Wear Mass Loss and Correlation after Eliminating Tailings Beach Sand Data

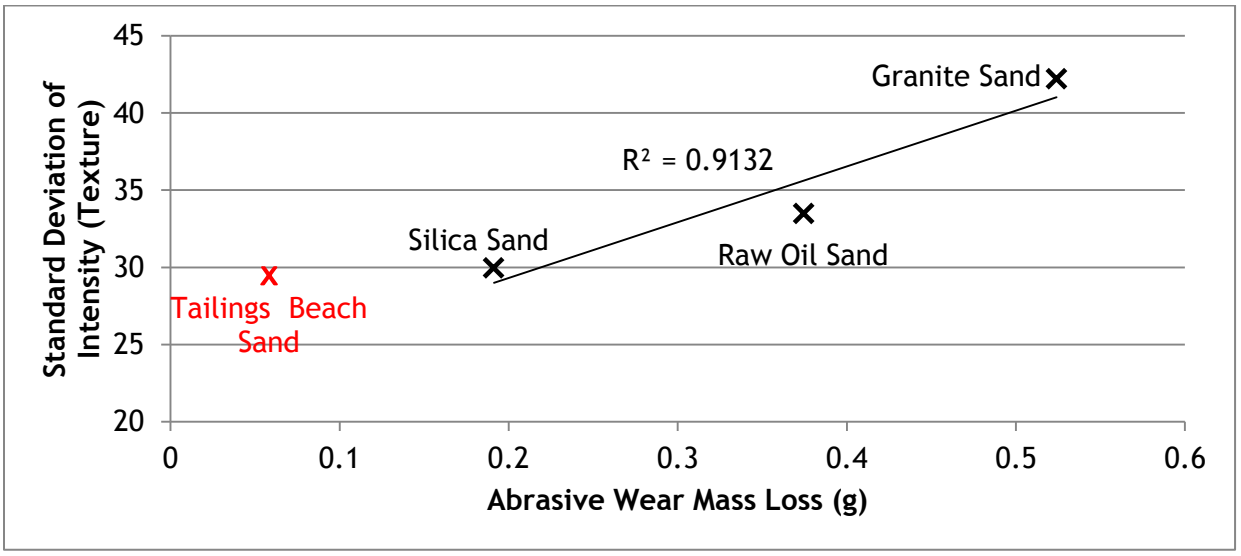


Figure 6-25: Standard Deviation of Texture vs Abrasive Wear Mass Loss and Correlation after Eliminating Tailings Beach Sand Data

Correlation coefficients are summarized in Table 6-13.

When the abrasive wear mass loss results from the tailings beach sand were discounted, all shape factors became much better predictors of abrasive wear. In particular, form factor and angularity index were especially good predictors, with coefficients of determination of 0.9966 and 0.9825 respectively. The angularity parameter and spike parameter quadratic fit followed closely behind and still provided an excellent correlation with wear rates.

Table 6-13: Coefficient of Determination between Measured Shape Parameters and Abrasive Wear Rate

| | $R^2$ Coefficient |
|---|---|
| Form Factor | 0.9966 |
| Form Index | 0.9241 |
| Angularity Index | 0.9825 |
| Convexity | 0.8901 |
| Angularity Parameter | 0.9422 |
| Spike Parameter Quadratic Fit | 0.9476 |
| Texture | 0.8778 |

Form factor, despite its name, does not truly represent only the form of the particle. Rather, it is more of an overall indicator of all three particle characteristics (form, angularity and texture) which likely is why it functioned so well as an indicator of abrasive wear potential.

One of the major drawbacks of parameters such as the form factor ($^{4\pi A}/_{P}$), which utilized the true particle boundary, is that they were extremely susceptible to image focus. When measuring dimensions at a pixel level, boundary length could quickly be exaggerated if images were not properly focussed. For this work, images were captured at extremely high contrast, resulting in a well-defined line between the particle and background. Additionally, the electron microscope used had an excellent ability to sharply focus images that resulted in good quality images.

Form index required a further analysis before the results could be truly appreciated. Recall from equation 2-7 that form index is the measure of change in five degree increments around the entire particle. This means that regardless of resolution the image was gathered at, form index is based on an angular measurement and therefore measures changes on the scale of $1/72^{th}$ of the circumference. Depending on the size of the particle, the scale of features being measured would change greatly.

For sand particles of approximately the same size as the larger raw oil sand particles, texture features have been found to be on the scale of approximately 15 μm, and angularity up to approximately 75μm (Masad and Button, 2000). The particles used in this Masad and Button study were retained on a 600μm sieve, passing an 1180μm sieve.

As an example, consider a slightly above average size raw oil sand particle, say 600 μm in diameter. Form index measures in five degree increments, which for this particle size equates

to a 26 μm arc length. The scale of features being measured by form index on a particle this size therefore is well in the range of texture or angularity, rather than form.

At the upper end of the size distribution for the Masad and Button (2001) study, a 1180μm particle would have a five degree arc length of 49μm. While this is closer to the size range that would represent form, it is still well in the range of an angularity type feature, assuming the particles used in this work share similar characteristics to those in the Masad and Button study.

It seemed reasonable to the author that as particle size changes linearly, the scale at which each of the different types of features occurs would also change linearly, especially when considered in the context of abrasive wear of a surface. If a particle was scaled to a different size, but identical shape, the interactions between the particle and surface would still occur in the exact same fashion, at the exact same particle features.

As the scale of features being measured by form index is based upon an angular measurement, the features being measured will decrease equally with particle size. Therefore, if the argument presented in the previous paragraph can be considered true, form index should provide a consistent measurement of a single particle shape type (form, angularity, texture) through any particle size, as long as the angle used for measurement is kept constant. In the case of the five degree angle used in this work, it was the author's opinion that form index was truly measuring angularity, rather than form.

This conclusion agreed with the results, as the form index results closely resembled the results of the other angularity measurements, when ranking sand in terms of rugosity (see Figure 6-9). The author was led to believe by the literature that form index should be an accurate measurement of form, without being influenced by angularity. However, if the argument presented above regarding form index is correct, the majority of shape parameters presented in this work measured angularity, with the only exceptions being form factor parameter and the standard deviation of brightness (texture) parameter.

As referenced in section 2.2.3.4, angularity is generally considered to be the most important factor for engineering purposes, so more factors aimed at measuring this type of feature were already included in this work. These factors (angularity index, convexity, angularity parameter and spike parameter quadratic fit) all displayed excellent correlation with abrasive wear rates, with $R^2$ coefficients ranging from 0.89 to 0.98.

Texture measurements represented the least amount of correlation with abrasive wear out of all shape parameters. However, with an $R^2$ coefficient of 0.88, it still displayed a significant relationship and can be considered an accurate predictor of potential abrasive wear.

### 6.5.3 Angle of Repose

It was thought while conducting particle shape parameter measurements that an easier method could be developed, particularly for texture measurements which were significantly more time consuming to accomplish. A common parameter encountered in the mining and geotechnical engineering world is the "angle of repose", or the angle formed against the horizontal when a material is piled without slumping. It was thought that this parameter would be closely related to particle shape, as more rugged particles would create higher angles of repose due to the increased inter-particle friction response and ability of these particles to interlock. Interestingly, the angle of repose was found to correlate almost exactly with the texture measurements, shown in Figure 6-26 below.

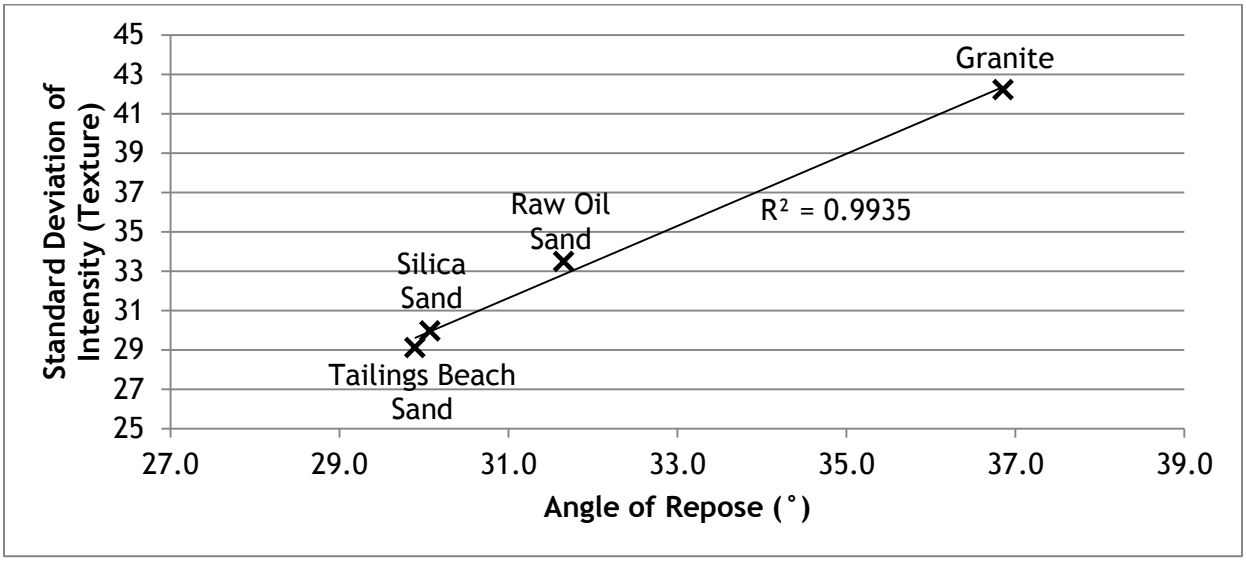


Figure 6-26: Material Angle of Repose vs Texture Parameter Correlation

While the angle of repose correlated very closely with the texture parameter measurements, the same could not be said for the other shape parameters measured. Correlation coefficients of the relationship between shape parameters and the angle of repose are summarized in Table 6-14, and graphs showing the relationships are shown in Appendix F

Table 6-14: Coefficient of Determination between Measured Shape Parameters and Angle of Repose

| | $R^2$ Coefficient |
|---|---|
| Form Factor | 0.0749 |
| Form Index | 0.5936 |
| Angularity Index | 0.3153 |
| Convexity | 0.5959 |
| Angularity Parameter | 0.5107 |
| Spike Parameter Quadratic Fit | 0.5710 |
| Texture | 0.9935 |

It is interesting to note that angle of repose also did display some correlation with abrasive wear mass loss, even when the tailings beach sand data was not omitted, as shown in Figure 6-27. When the tailings beach sand was dropped once again, the $R^2$ correlation coefficient between angle of repose and abrasive wear mass loss jumped from 0.80 to 0.88, suggesting that angle of repose may also be an accurate predictor of abrasion.

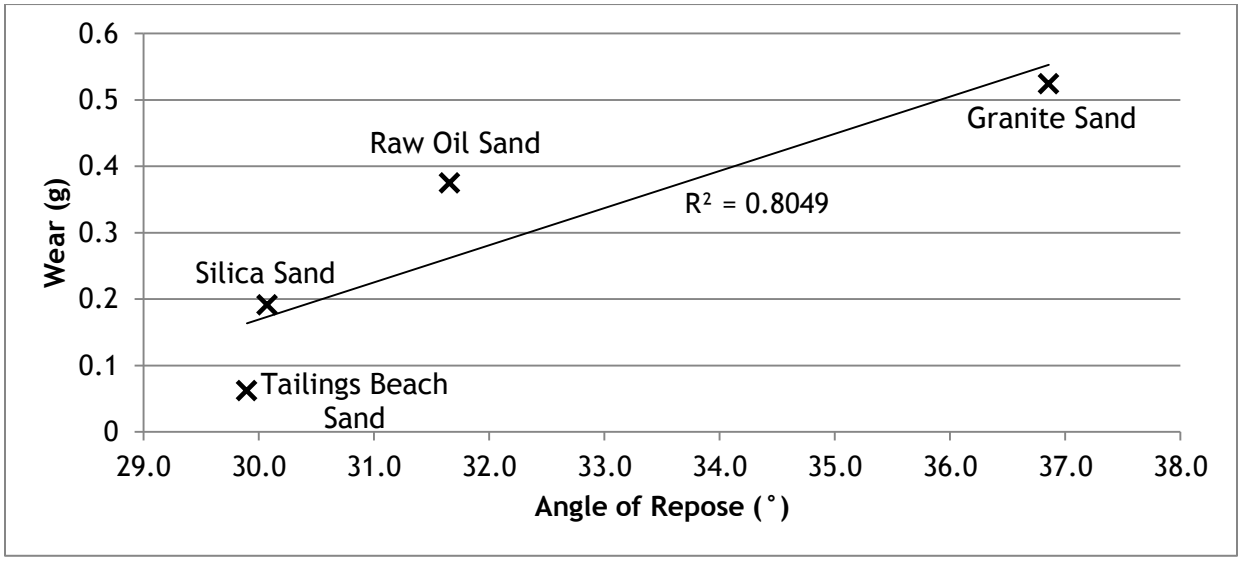


Figure 6-27: Material Angle of Repose vs Abrasive Wear Mass Loss Correlation

## 6.6 Specific Energy

Specific energy, by definition, is energy per unit volume. For the purposes of this work, it has been applied to the volume loss caused by abrasive wear. Refer to **Error! Reference source not found.** to see power draw curves. The average power draw during the unloaded portion of the test was subtracted from the average power draw of the loaded portion to determine the average power expended by wear processes. This average power draw is then multiplied

by the total time over which abrasive testing was conducted to determine energy expended by the abrasion.

This was not an exact correlation however, as a portion of this energy would be lost to any number of sources such as heat, sound, or as energy expended in the fracture of abrasive particles. Power draw and energy expended by type of abrasive is summarized in Table 6-15, as well as abrasive wear volume loss and specific energy. To calculate the volume wear loss, a chrome carbide unit weight of 6.87 g/cm$^3$ was used.

As Vickers hardness can be converted to units of Pascals, it was thought that the Vickers hardness of a material may also be directly proportional to its specific energy. Jacobson et al. state that for very sharp cutting tools, the specific energy is close to equal to the hardness of the workpiece. However, for multiple abrasive grits, only a very small number would achieve this idealized type of wear and the relationship does not show such a direct correlation.

While hardness of the material may be directly proportional to the specific energy, it was not the only factor that needed to be considered. The broad spread of specific energy presented

Table 6-15: Average Power Draw during Entire Abrasive Wear Test, Energy Expended by Test, Wear Loss and Specific Energy, by Abrasive Media Type

| | Average Power Draw (W) | Energy (J) | Wear loss (g) | Wear Loss (m$^3$) | Specific Energy (GPa) |
|---|---|---|---|---|---|
| Granite | 1.763 | 4232 | 0.5241 | 7.621E-08 | 55.53 |
| Tailings Beach Sand | 1.166 | 2798 | 0.0619 | 9.006E-09 | 310.71 |
| Raw Oil Sand | 1.152 | 2765 | 0.3746 | 5.447E-08 | 50.77 |
| Silica Sand | 0.892 | 2141 | 0.1912 | 2.781E-08 | 77.01 |

in Table 6-15 illustrated another important point when comparing Vickers hardness to specific energy: the energy required to cause a certain amount of volume loss is proportional not only to the hardness of the material, but also the abrasive efficiency of the media.

It was the opinion of the author that this particle abrasivity efficiency in this test was the result of two main factors: particle size and shape. Particle size was responsible for the extremely low wear rate of the tailings beach sand, and therefore the very high specific energy. Raw oil sand and silica sand, with very similar particle size, showed different specific

energy due to particle shape. The much more rugged oil sand was a more efficient abrasive than the very rounded silica sand, and as such required less energy per unit volume lost.

The granite sand, however, was much more difficult to accurately explain. It represented the most rugged of all the sand types, however did not appear to be the most efficient abrasive. It is the hypothesis of the author that this paradox is likely two-fold. First, while a large number of particles fell above the "critical particle size" (refer to section 2.2.3.2 and 6.3.3), there was still approximately 30% of the grain size distribution below 200 μm. Smaller particles abrade less, and this could have resulted in higher energy expenditures for the same amount of volume loss. Second, the granite sand used in this work was ground in the lab from rock core samples. A large number of particles may still have been undergoing breakage throughout the test, which would have resulted in higher energy losses to this phenomenon than the other sand types. If the sand was re-used to do multiple tests, it may have become evident through either particle size or shape analysis that breakage was occurring.

Stachowiak et al. (2006) used the fact that particle fracture is expected in high stress abrasion, but not low stress, to determine which abrasion type the test method being developed fell into through the SPQ analysis of particles before and after testing. Large changes in the SPQ value were seen as being due to particle fracture. This method could be extended to possibly be used in determination of the amount of particle fracture occurring, which may provide valuable insight into how much abrasive energy is truly being expended to cause wear, and how much is being expended through the fracture of particles.

### 6.6.1 Field Data Specific Energy

Data obtained from a P&H 4100 BOSS shovel operating in an oil sands mine was discussed and analyzed in Chapter 3 to determine the resistance to digging that a cable shovel experienced in an average pass through the dig face. This dig force was analyzed to determine the total energy expended that could be expected to be directly responsible for causing abrasion of shovel GET components. As discussed in section 3.2, the position of the shovel teeth at 0.1 second intervals in the dig cycle was found, from which the speed of the teeth could be determined. The power draw required to overcome dig resistance was found by multiplying instantaneous dig force by the instantaneous velocity as shown in equation 6-1. Energy expended was then be found by summing the area under the power-time graph, an example of which is shown in Figure 6-28.

$$Instantaneous\ Dig\ Power\ Draw = Dig\ Force * Velocity \quad (6\text{-}1)$$

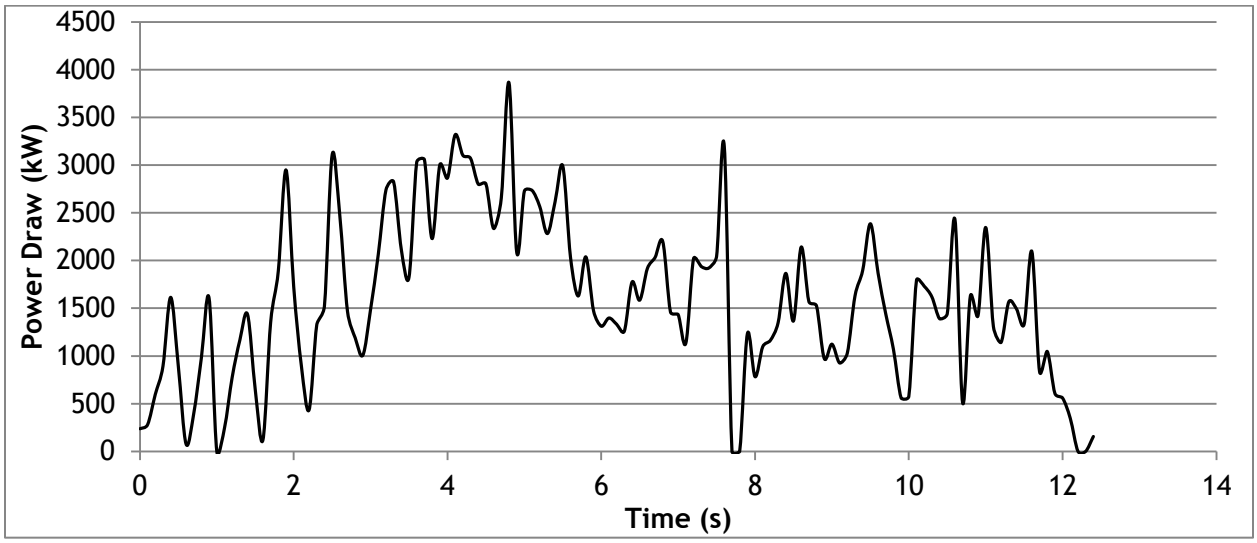


Figure 6-28: Power Draw of Dig Cycle 1

Figure 6-28 illustrates the power draw required to overcome only the dig resistance, and did not include any of the power required to lift the handle, dipper or ore. By summing the area under the curve, dig energy was determined, which is summarized in Table 6-16.

Table 6-16: Power Draw and Dig Energy Consumption of P&H 4100 BOSS

| | Average Power (kW) | Time (s) | Energy (kJ) |
|---|---|---|---|
| Dig Cycle 1 | 1583 | 12.5 | 19800 |
| Dig Cycle 2 | 1947 | 9.9 | 19277 |
| Dig Cycle 3 | 1944 | 11.1 | 21575 |
| Dig Cycle 4 | 2200 | 13.1 | 28822 |
| Dig Cycle 5 | 2010 | 13.5 | 27139 |
| Dig Cycle 6 | 2042 | 12.1 | 24707 |
| Dig Cycle 7 | 1661 | 10.5 | 17438 |
| Dig Cycle 8 | 1984 | 11 | 21829 |
| Dig Cycle 9 | 2029 | 11.9 | 24149 |

Taking into account the energy of all dig cycles gave an average energy expenditure of 22 748 kJ, per dig cycle. This energy however needed to be considered to be distributed across the entire shovel GET, whereas for the purposes of this study only the energy that is expended per single tooth was desired. Recall that the area of a single tooth is 0.1196 $m^2$, and the

surface area of the entire GET system is 2.605 $m^2$. Assuming the energy was distributed evenly, a single tooth should receive 0.1196/2.605 = 4.32% of this energy, or 983 kJ.

As a basis for comparing wear, a shovel tooth that had been in service for 18 hours was utilized. This tooth had undergone a large amount of wear, losing 36.5 kg of steel in 18 hours. A picture of the tooth is shown in Figure 6-29. Knowing the average energy per dig cycle, as well as the mass and therefore volume loss of the tooth, the only aspect left to determine specific energy of the abrasion associated with this tooth was the number of dig cycles it underwent. Not knowing exactly what the service life of the tooth was, several assumptions had to be made. The following time losses would likely occur per 12 hour shift:

- 2x15 minute overlap with previous/following shift
- 2x15 minute coffee break
- 30 minute lunch break

Therefore, in an 18 hour time frame, there could easily have been 2.25 hours of lost time. Using an average cycle time of 45 seconds, with availability and utilization of the shovel set to 80%, gives 806 dig cycles. With the average dig energy per cycle, per tooth, of 983 kJ found earlier, the specific energy associated with the wear of the tooth in question was determined.

Figure 6-29: Tooth after 18 Hours of Service (Left) and New Tooth (Right)

$$Specific\ Energy = \frac{983\ {}^{\frac{kJ}{Cycle}}/_{Tooth} * 806\ cycles}{0.00464\ m^3 Steel\ Loss} = 170.7 \frac{GJ}{m^3} \quad \text{6-2}$$

This 170.7 GJ/m$^3$ can also be expressed as 170.7 GPa. It should be noted at this time that this 170 GPa is highly variable. If the 18 hours this tooth was in service had higher than average downtime, bringing utilization of the shovel down to say 65%, the specific energy decreases to 139 GPa. On the other end, if the service life of this tooth was particularly efficient, and brought utilization and availability both up to say 95%, specific energy would rise to 240 GPa. Without knowing more about the actual nature of the service life of this tooth we can only estimate.

# 7 Conclusion

Chrome carbide samples were subjected to 40 minutes of abrasion testing, at a normal force of 25.lbs, with an abrasive grit to surface interaction speed of 0.775 m/s, meaning that samples underwent 1860m of lineal abrasion. Total mass loss of the samples was measured and reported. To go with the abrasive testing, three other main results were obtained and examined further in this work. Shape parameters, abrasive media angle of repose and specific energy of the wear tests were obtained in an attempt to provide valuable insight into the mechanisms of abrasive wear.

The main conclusions of this work can be summarized as:

- Form factor, form index, angularity index, convexity, angularity parameter, spike parameter quadratic fit and texture have all been shown to correlate very closely with abrasive wear rates, in a test that is indicative of field conditions
- Angle of repose acts as an excellent predictor of texture parameters
- Specific energy cannot be estimated solely by the material hardness, but rather must take into account a multitude of other factors that contribute to abrasive efficiency

The first main result that warrants further discussion is the extremely low wear rates obtained by the tailings beach sand (85% less than the raw oil sand). The tailings beach sand and raw oil sand in particular were so similar in all aspects other than size, yet produce such drastically different abrasive wear rates that it seemed appropriate to associate this difference with the particle size effect. As abrasive wear began on the samples, a work hardened layer formed which could not be penetrated by the majority of the small tailings beach sand particles. However, the larger media types succeeded in penetrating this layer and therefore induced higher wear rates in the bulk material below.

In addition to the work hardening done by abrasive wear, the surface grinder utilized to prepare the samples for testing likely induced some work hardening in the sample that contributed to the formation of this layer. This result highlighted the need to factor particle size into consideration when designing an abrasive wear test, even when dealing with broad particle size distributions.

When the extremely low tailings beach sand abrasive wear rate was discarded, all shape parameters then become extremely accurate predictors of wear. The fact that the remaining three types of abrasive media displayed such a direct correlation between abrasive wear and

particle shape parameters, despite slight variations in other factors normally associated with abrasive wear, lent credence to the particle size argument.

This correlation of shape parameters and abrasive was expected, but not perhaps to the extremely high levels that it was found to be. Other studies have investigated the role of particle shape in abrasive wear rates; however many of these studies utilized extremely soft materials with much harder media in order to ensure the only influence on abrasive wear rate was that of particle shape. It was unknown whether the same principles shown in the other studies would hold true when testing chrome carbide. This work showed that when testing a situation indicative of field conditions, particle shape can still be an accurate predictor of media abrasivity potential.

Though angle of repose correlated closely with texture measurements, it did not display any meaningful correlation with the other shape parameters. This suggested that the frictional properties associated with the stacking ability of sand particles (and therefore angle of repose) were dominated by texture type features, rather than angularity or form features. Particle texture has never generally been associated closely with abrasivity of particles; however in situations where the feature of interest in a study is texture, angle of repose may provide an easy and accurate solution.

The fact that angle of repose displayed moderate correlation with the abrasive wear rate of all four sand types was not insignificant, however it needed to be interpreted with a grain of salt as it may be no more than a coincidence. With only four samples to draw correlation from, and no other previous studies conducted on the matter, it was impossible to conclude angle of repose could accurately predict wear in situations when the particle size factor plays a role in abrasion rates.

There was a belief at the beginning of this work that the Vickers hardness of the material being abraded and the specific energy of the abrasion would share a very close relationship. This is still believed to be an accurate assumption, however many other factors must be taken into account to gain an accurate prediction of actual abrasive wear, including many abrasive media characteristics.

It was not entirely clear the effect on specific energy caused by media shape, hardness, size, as well as the other normal influences on abrasive wear. However, one fact that was exceedingly clear at the end of this work is the need to undertake a comprehensive review of

the various physical parameters associated with an abrasive media type before any sort of accurate conclusions can be drawn regarding specific energy.

There was a definite relationship that existed between particle shape, size, and specific energy of the wear it induced. However these are not the only pieces to the puzzle. Other physical properties of the abrasive media must be taken into account such as hardness, fracture toughness, and what types of cleavage planes may exist within a particle. If the abrasive media undergoes high stress abrasion and is prone to fracture, energy that may normally be expended as abrasive wear would be channelled into the fracture of particles. Along the same lines, if a particle undergoes fracture, the cleavage planes within the mineral will likely control the shape of the new particles that are formed, which may greatly increase angularity. Based on the conclusions of this work, an increase in angularity would result in increased abrasion efficiency, and therefore higher wear rates, provided comminuted particle size did not decrease to the point where the particle size effect begins.

It was hoped that through the use of specific energy, correlation could be drawn between lab tests and field data. Despite the variety of abrasive media used for tests, specific energy of the field data did not appear to closely align with the results from the lab tests. It was expected that the chrome carbide samples, due to increased hardness over a standard shovel tooth, would exhibit a much higher specific energy. However, the opposite appears to be true. This could be due to any number of reasons, and without further testing into the matter it is hard to determine what the main cause may be. It is the opinion of the author that the bitumen fraction of oil sand played an important role in abrasion of shovel GET, and perhaps acted as a boundary layer lubricant that prevents contact between some sand particles and the shovel parts. Energy normally directed towards causing abrasion was dissipated by the bitumen, which caused a reduction in the actual wear experienced, and resulted in a much higher specific energy calculated for the field conditions.

Regardless, it was heartening to see that the specific energy found in lab tests and field data was well within an order of magnitude of each other. This suggested that while not entirely useful in this work, with further research into the matter, specific energy can likely still play a useful role in the prediction of wear.

At the conclusion of this work, with a further insight into many of the aspects that influence abrasive wear, several of the factors that contribute to such high wear rates in the Alberta oil sands have become clear. First, the presence of extremely hard minerals, especially in the oil

rich parts of the McMurray deposit, display hardness greatly in excess of materials typically used in ground engaging tools. Secondly, the sheer volume of material being moved creates extremely high stresses experienced at the ground engaging tool/ore interface. Finally, the angularity of the coarser sand particles typically experienced in oil sands ore is very high, and contributes to the ability of that sand to abrade surfaces very efficiently. The energy generated at the ground engaging tool/ore interface is effectively utilized when it comes to abrading surfaces, contributing to increased abrasive wear.

# 8 Recommendations for Future Work

The work completed thus far has made a good step towards a better understanding of the abrasivity of media due to particle shape, and a possible method to extrapolate lab abrasive wear testing results to field conditions, but many pitfalls still existed. The lab results for specific energy did not closely mimic those of the field analysis, but many possible issues regarding this may be reconciled through improved collection of field data.

The shovel tooth that formed the basis for the analysis of field wear conditions was provided without much insight as to the actual digging conditions it faced. The only known fact was that the tooth had been used for 18 hours, without any knowledge as to how consolidated the face material was, what sort of downtime had been associated with the shovel in that period, how effectively the shovel had been utilized, or even what sort of digging the shovel had been used for. For example, if this particular shovel had been progressing parallel to a dig face, the teeth on the inside would experience much more wear than those on the outside.

More information should be obtained regarding digging conditions in the field for any tooth samples obtained. Qualitative input from experienced operators would be key, regarding the ease of digging experienced throughout the life of the tooth. Along the same lines, additional dig force data should be obtained to better estimate the overall average throughout the life of a tooth. Ideally this digging resistance data would come from the same dig cycles that a tooth selected for comparison had been used for. It was assumed that all of the energy expended by the shovel to overcome dig resistance was directly translated to abrasive energy, however this argument needs some additional thought. While it is clear that some dig energy must be expended as abrasion on the shovel tooth, a good deal of energy may also be lost to any number of other factors, the proportions of which are unknown. This may have been a key factor in the discrepancy of specific energy between field data and lab results

Additionally, the lab results for specific energy relied upon the power draw of the entire testing machine motor to determine energy expended by abrasion. Perhaps with the addition of a dynamic torque sensor to the driveshaft, a more accurate estimate of abrasion energy could be obtained through calculations.

The testing method presented in this work also has the potential to assess the performance of a multitude of other material types of almost any hardness, provided the hardness of the material being tested remains lower than the hardness of the abrasive media. Any material

sample of a similar size used in this work could be loaded in the testing machine, and any abrasive media could be used, provided proper flow through a nozzle could be established. If this testing machine was used in the testing of another type of material used in different conditions than a shovel tooth, obviously this would require a whole new set of both qualitative and quantitative inputs to ensure the test accurately mimics field conditions.

The ability to test a multitude of other material types also brings with it another interesting possibility. It has been shown in this work that the specific energy of abrasion can vary greatly between abrasive media of different particle shapes, even while abrading the same material. It is not a stretch to say that using one type of abrasive media to abrade a variety of different materials of varying hardness would also bring with it great variation in the abrasive efficiency, and therefore specific energy of those situations. This suggests that there may be a relationship that exists between the hardness of material and media, and specific energy. It is the author's opinion that if testing was done on this subject, a direct correlation between the specific energy of abrasion and the ratio of hardness ($H_M/H_A$) would be evident.

While the machine used in this work is an effective method of testing abrasion, it is limited to only using dry sands as abrasive media. In order to accurately mimic digging conditions it may be important to include the bitumen fraction of oil sand. To the author's knowledge, there has not been any testing thus far on the effect that the bitumen fraction has on abrasion. A study into this subject may prove the bitumen plays a much more important role than previously thought.

Finally, the use of angle of repose to predict particle shape parameters is another thought-provoking result. While it is highly unlikely that the angle of repose would be an accurate predictor of shape parameters for all media types, and will not replace the direct measurement of particles, it still presented a useful, easy and quick method to obtain a very accurate estimate of the texture parameter in this study.

## Bibliography


Al Rousan, T. (2004). Characterization of Aggregate Shape Properties Using a Computer Automated System. *PhD Dissertation*. College Station: Texas A&M University.

Alberta Energy Regulator. (2014). *Alberta's Energy Reserves 2013 and Supply/Demand Outlook 2014-2023*. Calgary: Alberta Energy Regulator.

Al-Rousan, T., Masad, E., Tutumluer, E., & Pan, T. (2007). Evaluation of Image Analysis Techniques for Quantifying Aggregate Shape Characteristics. *Construction and Building Materials*, 978-990.

ASTM. (2001). *Standard Terminology Relating to Wear and Erosion, Standard G-40-01*. West Conshohocken: American Society for Testing and Materials.

ASTM. (2007). ASTM G105. *Standard Test Method for Conducting Wet Sand/Rubber Wheel Abrasion Tests*. American Society for Testing and Materials.

ASTM. (2010). Standard Test Method for Measuring Abrasion Using the Dry Sand/Rubber Wheel Apparatus. American Society for Testing and Materials.

Backer, W., Marshall, E., & Shaw, M. (1952). Size Effect in Metal Cutting. *Trans ASME*, 61-72.

Balideh, S. (2015). *Influence of Particle Shape and Texture on Broken Sandstone Strength Behaviour (PhD Dissertation)*. Edmonton: University of Alberta.

Barrett, P. (1980). The Shape of Rock Particles, A Critical Review. *Sedimentology*, 291-303.

Batchelor, A., & Stachowiak, G. (2013). Fundamentals of Contact Between Solids. In A. Batchelor, & G. Stachowiak, *Engineering Tribology, 4th Edition* (pp. 475-524). Oxford: Butterworth Heinemann Ltd.

Bayer, R. (1994). *Mechanical Wear Prediction and Prevention*. New York: Marcel Dekker Inc.

Berthier, Y. (2005). Third-Body Reality - Consequences and Use of the Third-Body Concept to Solve Friction and Wear Problems. In G. Stachowiak, *Wear - Materials, Mechanisms and Practise* (pp. 291-316). Chichester: John Wiley and Sons.

Canadian Oil Sands. (2013, 12 09). *Canadian Oil Sand*. Retrieved 12 10, 2014, from Canadian Oil Sands Website: http://www.cdnoilsands.com/Media-

Centre/PressReleaseDetails/2013/Canadian-Oil-Sands-2014-Budget-Major-Capital-Projects-Nearing-Completion/default.aspx

Carrigy, M. (1959). The Significance of a Grain Size Classification of the Sands of The McMurray Formation, Alberta. *Proceedings of the 5th World Petroleum Congress* (pp. 575-590). New York: World Petroleum Congress.

Carrigy, M. (1966). *Lithology of the Athabasca Oil Sands*. Edmonton: Research Council of Alberta.

Clark, H. (1991). A Comparison of the Erosion Rate of Casing Steels by Sand-Oil Suspension. *Wear*, 217-230.

Coronado, J. (2009). Partcile Size Effect on Abrasion Resistance of Motttled Cast Iron with Different Retained Austenite Contents. *Wear*, 2077-2082.

Darling, P. (2011). *SME Mining Engineering Handbook*. Society for Mining, Metallurgy and Exploration.

De Pellegrin, D., & Stachowiak, G. (2002). Assessing the Role of Particle Shape and Scale in Abrasion Using 'Sharpness Analysis', Part I. *Wear*, 1016-1025.

De Pellegrin, D., & Stachowiak, G. (2004). Sharpness of Abrasive Particles and Surfaces. *Wear*, 614-622.

Dusseault, M., & Morgenstern, N. (1978). Shear Strength of Athabasca Oil Sands. *Canadian Geotechnical Journal*, 216-238.

ESCO. (2016, April 22). *ESCO Corporation*. Retrieved from Whisler Lip System: http://www.escocorp.com/EN/Products/Pages/whisler-lip-system.aspx

Eyre, T. (1976). Wear Characteristics of Metals. *Tribology International*, 211.

Fisher, G., Wolfe, T., & Meszaros, K. (2013, June). The Effects of Carbide Characteristics on the Performance of Tungsten Carbide Based Composite Overlays, Deposited by Plasma Transfered Arc Welding. *Journal of Thermal Spray Technology, 22*(5), 764-771.

Fisher, G., Wolfe, T., Yarmuch, M., Gerlich, A., & Mendez, P. (2011, 05 11). *The Use of Protective Weld Overlays in Oil Sands Mining*. Retrieved 11 24, 2014, from Candadian

Center For Welding and Joining, Publications: https://www.ualberta.ca/~ccwj/publications/Papers/Journal(Not%20Refereed)/Wear%20Resistance/Fisher%20-%20The%20Use%20of%20Protective%20Weld%20Overlays%20in%20Oil%20Sands%20Mining.pdf

Fletcher, T., Chandan, C., Masad, E., & Sivakumar, K. (2002). *Aggregate Imaging System (AIMS) for Characterizing the Shape of Fine and Coarse Aggregates*. Washington, DC: Transportation Research Board.

Fletcher, T., Chandan, C., Masad, E., & Sivakumar, K. (2002). Measurement of Aggregate Texture and its Influence on Hot Mix Asphalt Permanent Deformation. *Journal of Testing and Evaluation*, Vol. 30, No. 6.

Gane, N., & Cox, J. (1970). The Micro-Hardness of Metals at very Low Loads. *Philosophical Magazine*, 881-891.

Graham, D., & Baul, R. M. (1972). An Investigation Into the Mode of Metal Removal in the Grinding Process. *Wear*, 301-314.

Hamblin, M., & Stachowiak, G. (1995). A Multi-Scale Measure of Particle Abrasivity. *Wear*, 225-233.

Hamblin, M., & Stachowiak, G. (1995). A Multi-Scale Measure of Particle Abrasivity and its Relation to Two-Body Wear Abrasive Wear. *Wear*, 190-196.

Hamblin, M., & Stachowiak, G. (1996). Description of Abrasive Particle Shape and its Relation to Two-Body Abrasive Wear. *Tribology Transactions*, 803-810.

Harper, D., Gill, M., Hart, K., & Anderson, M. (2002). Plasma Tranferred Arc Overlays Reduce Costs in Oil Sands Processing. *International Thermal Spray*.

Hokkirigawa, K., & Kato, K. (1988). The Effect of Hardness on the Transition of the Abrasive Wear Mechanisms of Steel. *Wear*, 241-251.

Hussainova, I., Pirso, J., Antonov, M., Juhani, K., & Letunovits, S. (2007). Erosion and Abrasion of Chromium Carbide Based Cermets Produced by Different Methods. *Wear*, 905-911.

Hutchings, I. (2005). The Challenge of Wear. In G. Stachowiak, *Wear - Materials, Mechanisms and Practise* (pp. 1-7). Chichester: John Wiley and Sons.

Jacobson, S., Wallen, P., & Hogmark, S. (1988). Fundamental Aspects of Abrasive Wear Studied by a New Numerical Simulation Model. *Wear*, 207-223.

Jankauskas, V., & Kreivaitis, R. (2007). Study of Wear Prediction by Applying Surface Microgeometric Parameters. *Mechanika*, 65-70.

Janoo, V. (1998). *Quantification of Shape, Angularity, and Surface Texture of Base Course Materials*. Hanover, NH: US Army Corps of Engineers.

Joseph, J., & Shi, N. (2011). Modelling Cable Shovel Geometry and Kinematics. *CIM Journal*, 107-116.

Joseph, T. G., & Shi, N. (2012). A Revised Dipper-Ground Equilibrium Derivation for Shovels Operating in Oil Sand and Soft Ground. *CIM Journal*, 47-53.

JoyGlobal. (2012). *Joy Global Products: 4100 BOSS*. Retrieved July 8, 2015, from Joy Global Mining: http://www.joyglobal.com/product-details/4100c-boss

Kandhal, P., Motter, J., & Khatri, M. (1991). *Evaluation of Particle Shape and Texture: Manufactured vs. Natural Sands*. Auburn, AL: National Center for Asphalt Technology.

Kato, K. (2002). Classification of Wear Mechanisms/Models. *Proceedings of the Institution of Mechanical Engineers*, 349-355.

Kayaba, T. (1986). Analysis of the Abrasive Wear Mechanism by Successive Observations of Wear Processes in a Scanning Electron Microscope. *Wear*, 419-430.

Kaye, B. (1984). Fractal Description of Fine Particle Systems. In J. Beddow, *Particle Characterization in Technology, Vol. 1: Applications and Microanalysis* (pp. 81-100). Boca Raton: CRC Press.

King, H. (2014). *Geology*. Retrieved 12 16, 2014, from Mohs Hardness Scale: http://geology.com/minerals/mohs-hardness-scale.shtml

Kulu, P., Tarbe, R., Kaerdi, H., & Goljandin, D. (2009). Abrasivity and Grindability Study of Mineral Ores. *Wear*, 1832-1837.

Kuo, C., & Freeman, R. (2000). *Imaging Indices for Quantification of Shape, Angularity, and Surface Texture of Aggregates*. Washington, DC: Transportation Research Board.

Levy, A., & Chik, P. (1983). The Effects of Erodent Composition and Shape on the Erosion of Steel. *Wear*, 151-162.

Lin, Z. (2013). *Abrasive Wear of Shovel Teeth in Oil Sand (MSc. Thesis)*. Edmonton: University of Alberta.

Little, D., Button, J., Jayawickrama, P., Solaimanian, M., & Hudson, B. (2003). *Quantify Shape, Angularity and Surface Texture of Aggregates Using Image Analysis and Study Their Effect on Performance*. College Station: Texas Transportation Institute.

Llewellyn, R., & Tuite, C. (1995, March). Hardfacing Fights Wear in Oil Sands Operation. *Welding Journal*, 55-60.

Llewellyn, R., Anderson, M., & Chiovelli, S. (2003). The Use of Tungsten Carbide Materials for Oilsand Wear Applications. *Thermal Spray*, 509-518.

Masad, E., & Button, J. (2000). Unified Imaging Approach for Measuring Aggregate Angularity and Texture. *Computer-Aided Civil and Infrastructure Engineering*, 273-280.

Masad, E., Al-Rousan, T., Button, J., & Little, D. (2007). *Test Methods for Characterizing Aggregate Shape, Texture, and Angularity*. Washington, DC: National Cooperative Highway Research Program.

Masad, E., Olcott, D., White, T., & Tashman, L. (2001). *Correlation of Fine Aggregate Imaging Shape Indices with Asphalt Mixture Performance*. Washington, DC: Transportation Research Board.

McKee, B., & Wu, J. (1997, July). An Overview of Wear Resistant Alloys for the Mining Industry. *CIM Bulletin*, 71-74.

*Minerals Zone World Mineral Exchange*. (2014). Retrieved 12 16, 2014, from Quartzite: http://www.mineralszone.com/stones/quartzite.html

Misra, A., & Finnie, I. (1981). On the Size Effect in Abrasive and Erosive Wear. *Wear*, 359-373.

Moore, M., & King, F. (1980). Abrasive Wear of Brittle Solids. *Wear*, 123-140.

Mossop, G. D. (1980, January 11). Geology of the Athabasca Oil Sands. *Science, 207*(4427), 145-152.

Mulhear, T., & Samuels, L. (1962). The Abrasion of Metals: A Model of the Process. *Wear*, 478-498.

Neville, A., & Morina, A. (2005). Wear and Chemistry of Lubricants. In G. Stachowiak, *Wear - Mechanisms, Materials and Practise* (pp. 71-94). Chichester: John Wiley & Sons.

Osacky, M., Geramian, M., Ivey, D., Liu, Q., & Etsell, T. (2013). Mineralogical and Chemical Composition of Petrologic End Members of Alberta Oil Sands. *Fuel*, 148-157.

Rousan, T. M. (2004). *Characterization of Aggregate Shape Properties Using a Computer Automated System (PhD Dissertation)*. College Station: Texas A&M University.

Russ, J. (1995). *The Image Processing Handbook, 2nd Edition*. Boca Raton, FL: CRC Press.

Sasada, T., Oike, M., & Emori, N. (1984). The Effect of Abrasive Grain Size on the Transition Between Abrasive and Adhesive Wear. *Wear*, 291-302.

Stachowiak, G. (1998). Numerical Characterization of Wear Particles Morphology and Angularity of Particles and Surfaces. *Tribology International*, 139-157.

Stachowiak, G. (2000). Particle Angularity and it's Relationship to Abrasive and Erosive Wear. *Wear*, 214-219.

Stachowiak, G. (2005). *Wear - Materials, Mechanisms and Practise*. Chichester: John Wiley & Sons.

Stachowiak, G. (2013). Abrasive, Erosive and Cavitation Wear. In G. Stachowiak, *Engineering Tribology* (pp. 525-576). Kidlington: Elsevier.

Stachowiak, G. (2013). Appendix. In G. Stachowiak, *Engineering Tribology* (pp. 809-821). Kidlington, Oxford: Elsevier.

Stachowiak, G. (2013). Introduction. In G. Stachowiak, *Engineering Tribology* (pp. 1-10). Kidlington, Oxford: Elsevier.

Stachowiak, G., & Podsiadlo, P. (2001). Characterization and Classification of Wear Particles and Surfaces. *Wear*, 194-200.

Stachowiak, G., & Podsiadlo, P. (2006). Towards the Development of an Automated Wear Particle Classification System. *Tribology International*, 1615-1623.

Stachowiak, G., Stachowiak, G., & Brandt, J. (2006). Ball-Cratering Abrasion Tests with Large Abrasive Particles. *Tribology International*, 1-11.

Stachowiak, G., Stachowiak, G., & Podsiadlo, P. (2008). Automated Classification of Wear Particles Based on their Surface Texture and Shape Features. *Tribology International*, 34-43.

Swanson, P., & Vetter, A. (1985). The Measurement of Abrasive Particle Shape and Its Effect on Wear. *American Society of Lubrication Engineers Transactions*, 225-230.

Tafesse, S., Fernlund, J., Sun, W., & Bergholm, F. (2013). Evaluation of Image Analysis Methods used for Quantification of Particle Angularity. *Sedimentology*, 1100-1110.

Torrance, A. (1981). An Explanation of the Hardness Differential Needed for Abrasion. *Wear*, 263-266.

Torrance, A. (2005). Modelling Abrasive Wear. *Wear*, 281-293.

*University of Minnesota*. (2009, 01 09). Retrieved 12 16, 2014, from Mineral Web Pages: http://www.esci.umn.edu/courses/1001/minerals/potassium_feldspar.shtml

US EIA. (2014, 09 30). *U.S. Energy Information Administration*. Retrieved 12 10, 2014, from U.S. Energy Information Administration Website: http://www.eia.gov/countries/cab.cfm?fips=CA

Wadell, H. (1932). Volume, Shape and Roundness of Rock Particles. *The Journal of Geology*, 443-451.

*Web Mineral*. (2012, 9 15). Retrieved 12 16, 2014, from Choloritoid Mineral Data: http://webmineral.com/data/Chloritoid.shtml#.VJHvVyvF9Bb

Winkelmann, H., Varga, M., & Badisch, E. (2009). Wear Mechanisms at High Temperatures: Part 2: Temperature Effect on Wear Mechanisms in the Erosion Test. *Tribology Letters*, 167-175.

Yarmuch, M., Patchett, B., Ivey, D., & Anderson, M. (2009). Effect of Welding Parameters and Gas Composition on PTAW Behaviour. *Trends in Welding Research, Proceedings of the 8th International Conference* (pp. 705-714). Pine Mountian, Georgia: ASM International.

Zikin, A., Hussainova, I., Katsich, C., Badisch, E., & Tomastik, C. (2012). Advanced Chromium Carbide-Based Hardfacings. *Surface and Coatings Technology, 206*, 4270-4278.

## Appendix A - Breakdown of Shape Parameter Factor Histograms by Material Type

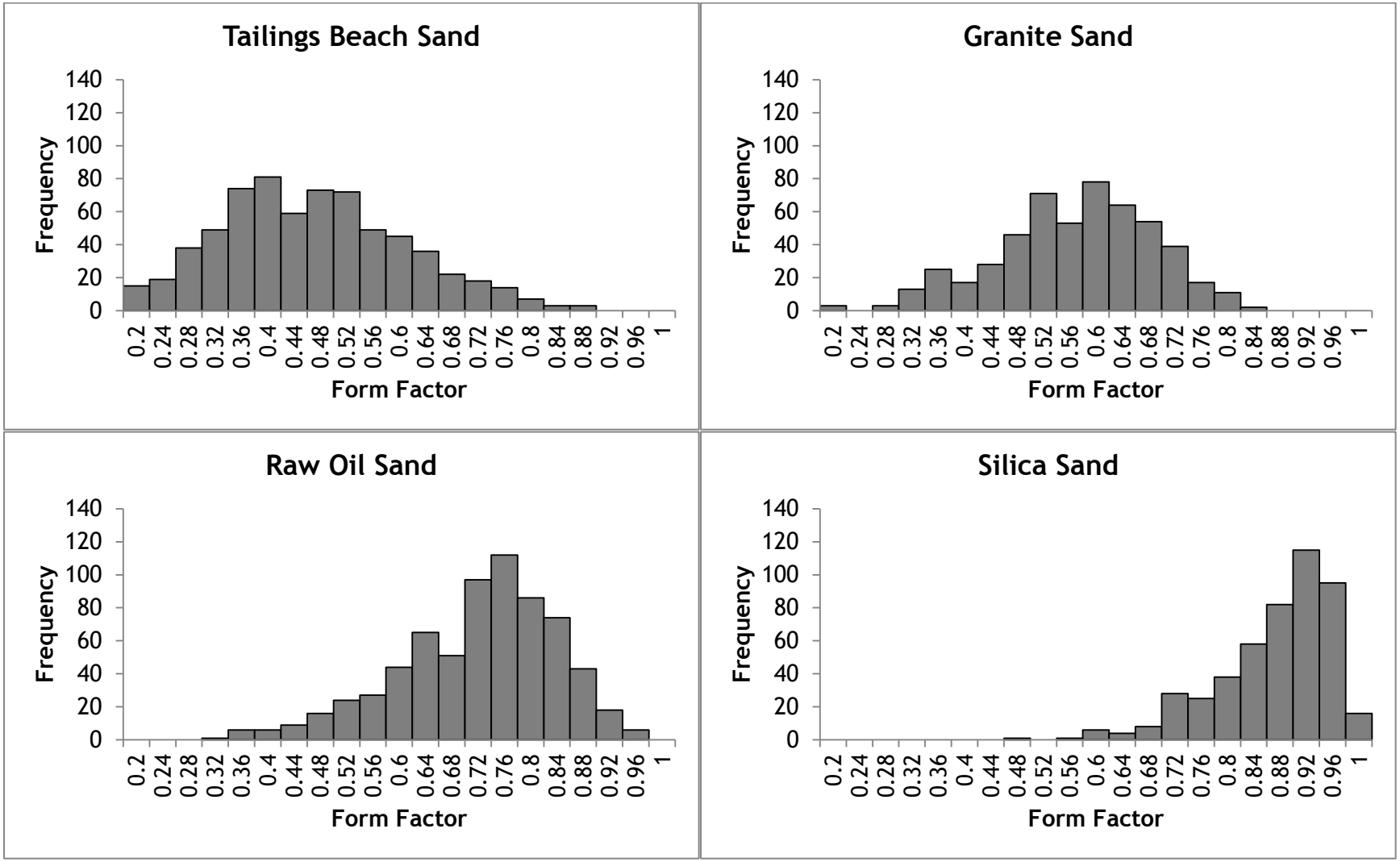


Distribution of Form Factor Parameter, Broken Down by Material Type

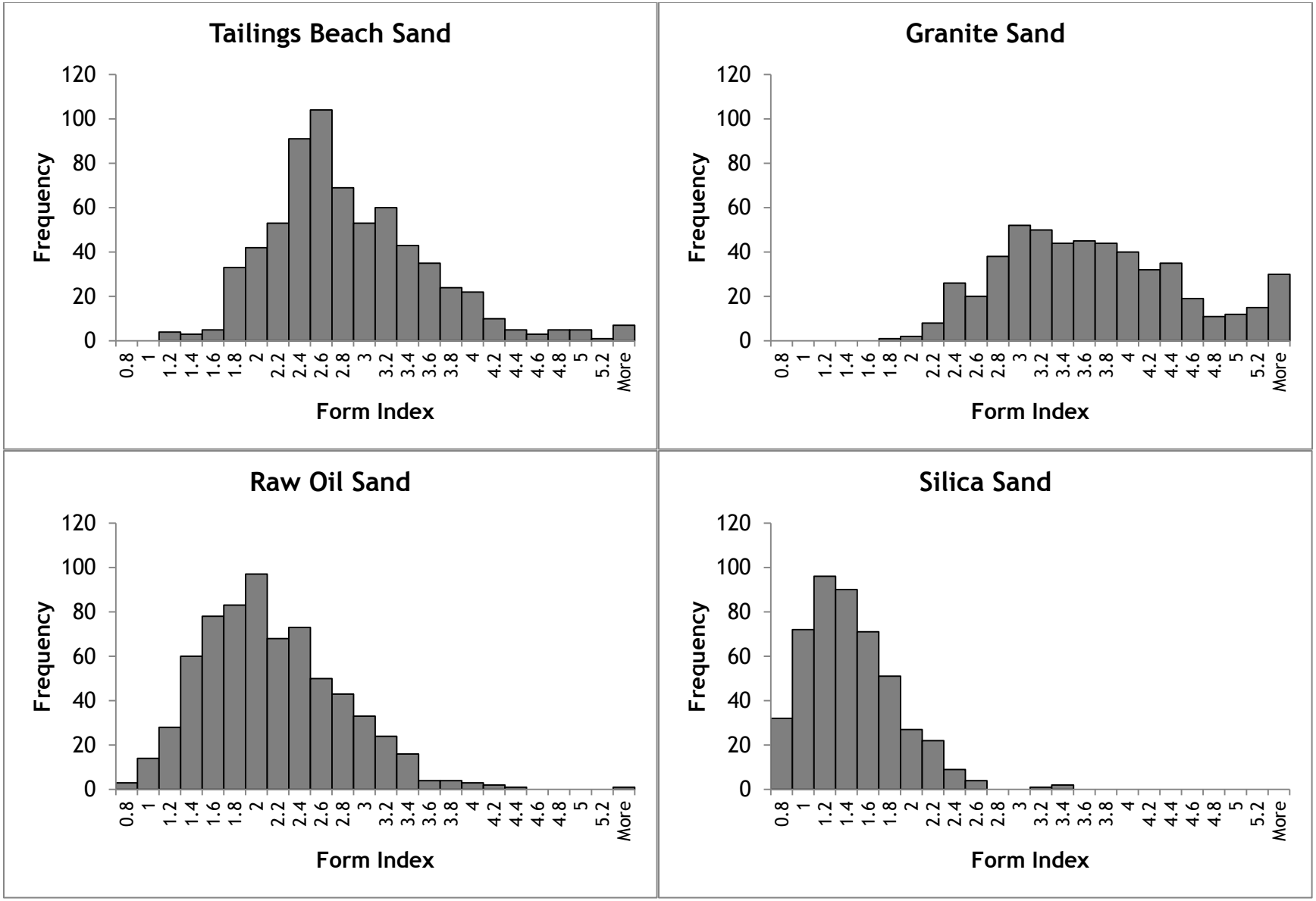


Distribution of Form Index Parameter, Broken Down by Material Type

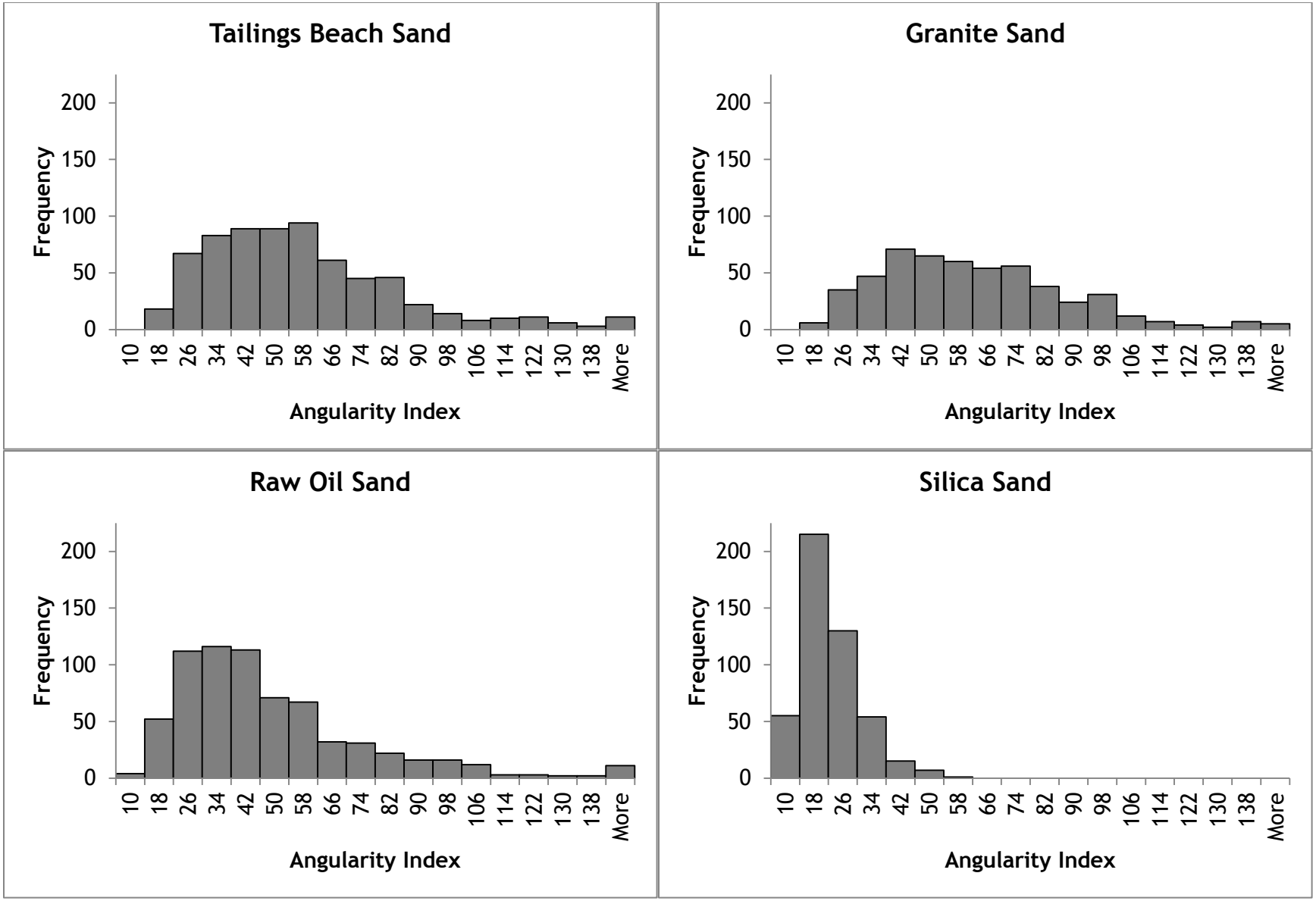


Distribution of Angularity Index Parameter, Broken Down by Material Type

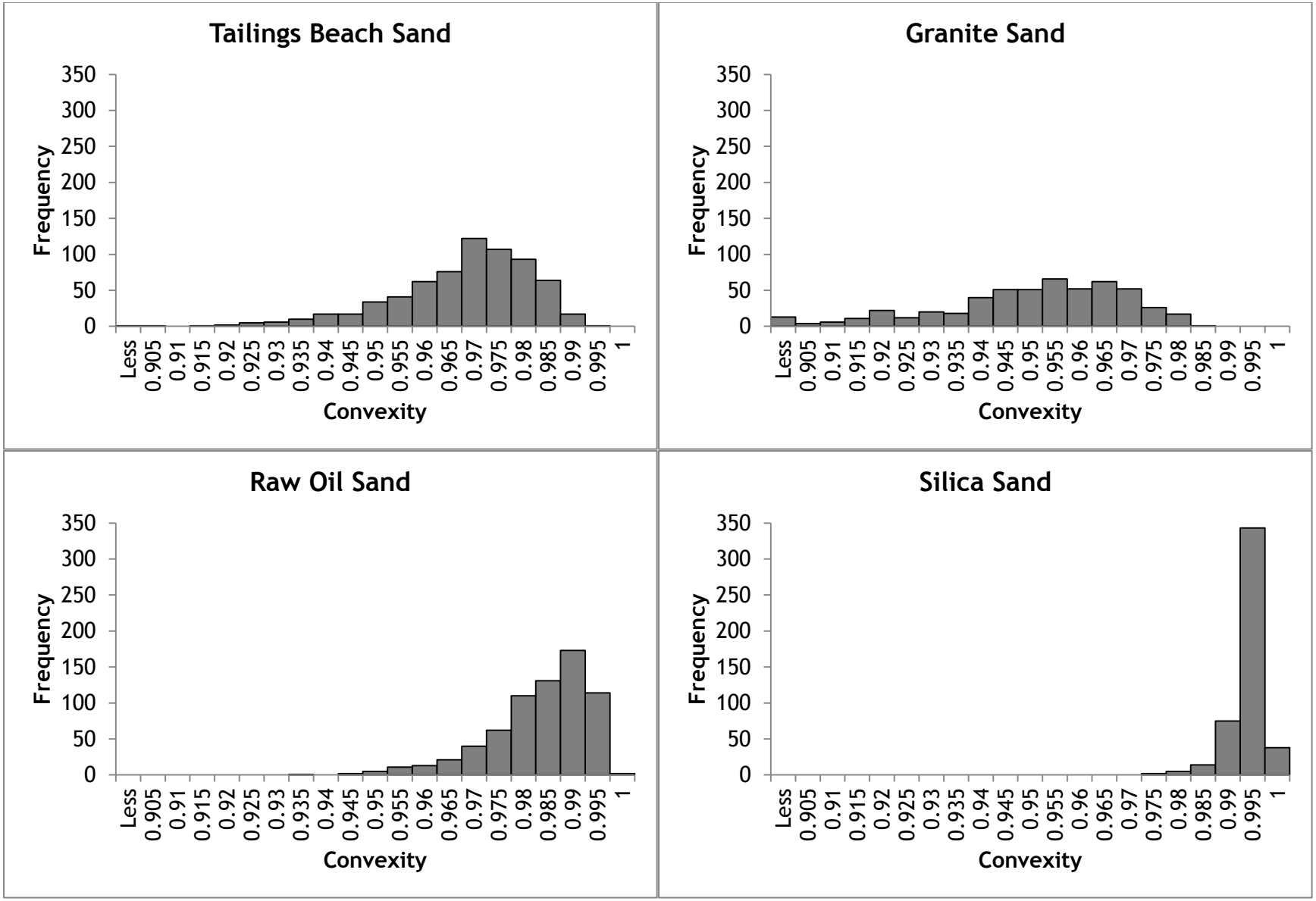


Distribution of Convexity Parameter, Broken Down by Material Type

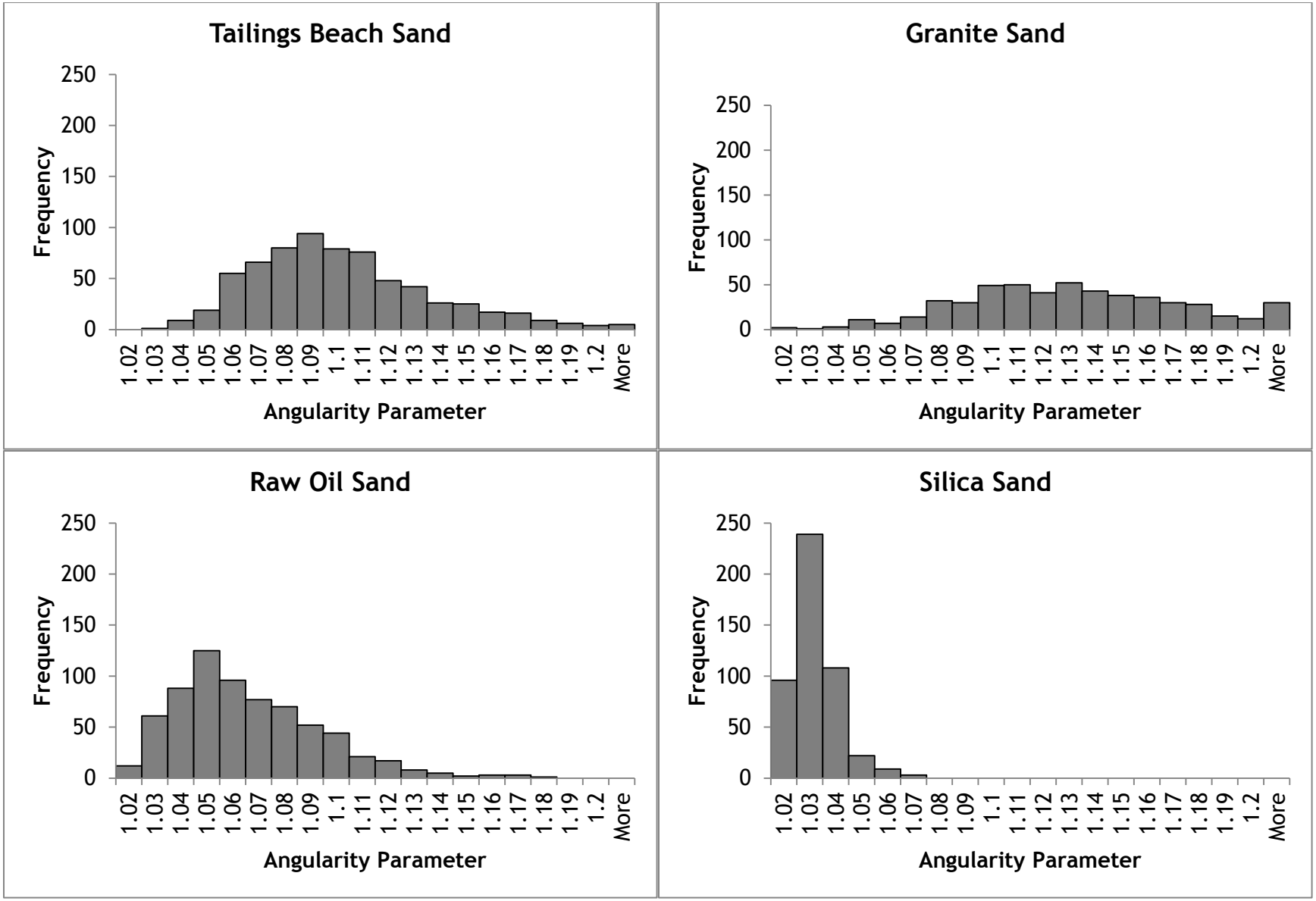


Distribution of Angularity Parameter, Broken Down by Material Type

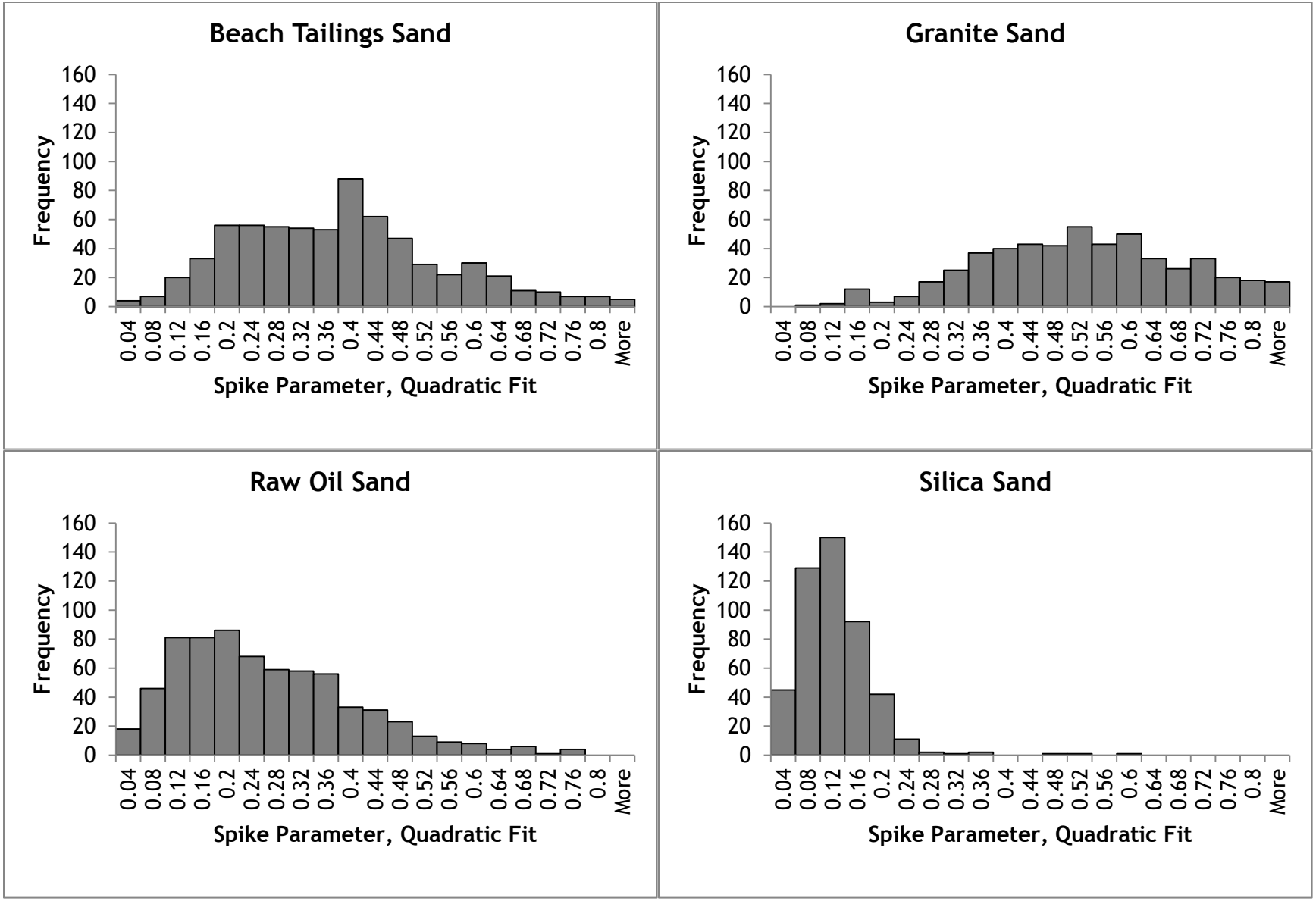


Distribution of Spike Parameter Quadratic Fit, Broken Down by Material Type

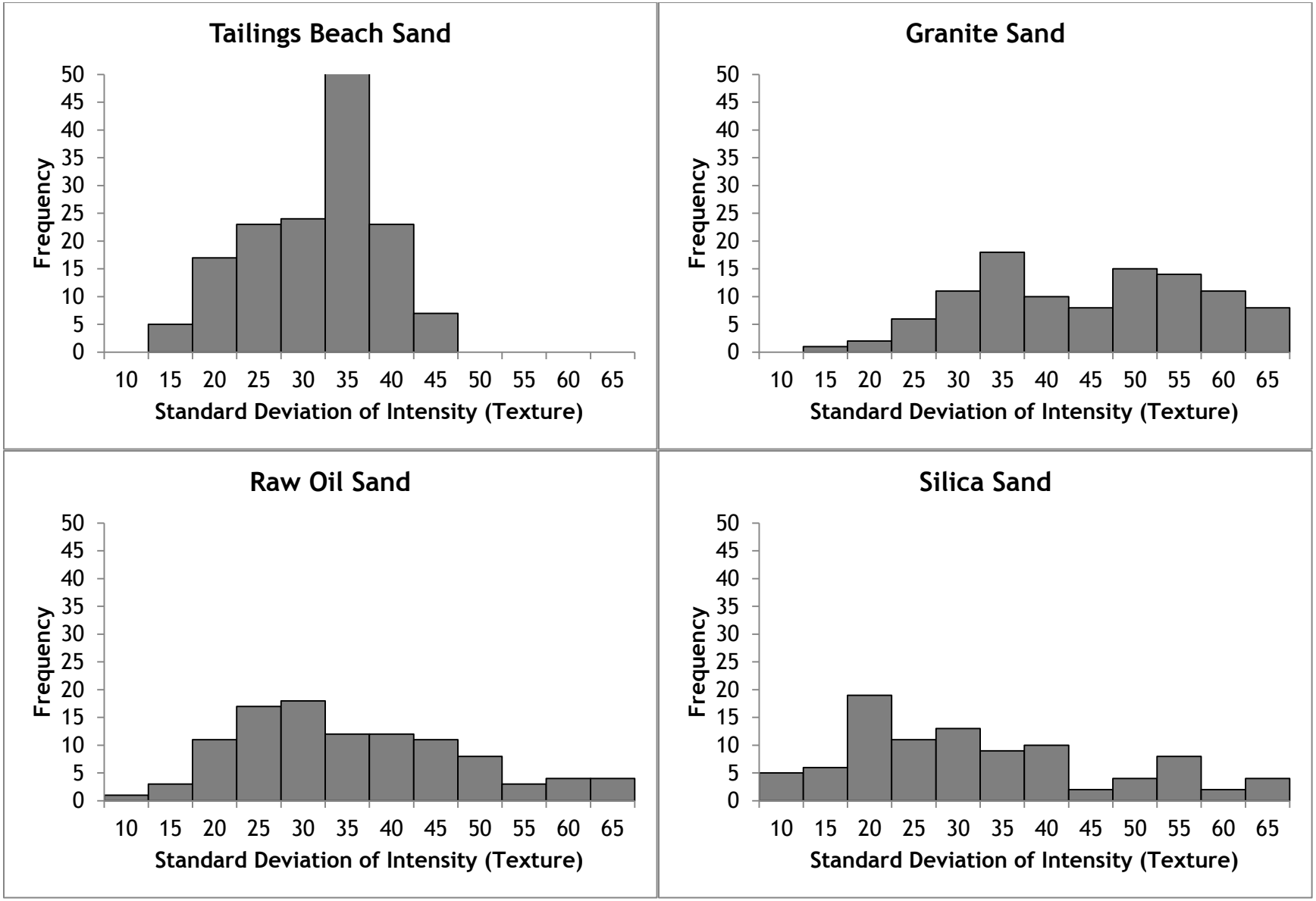


Distribution of Texture Parameter, Broken Down by Material Type

## Appendix B - General Images of Sand Particles Gathered with SEM

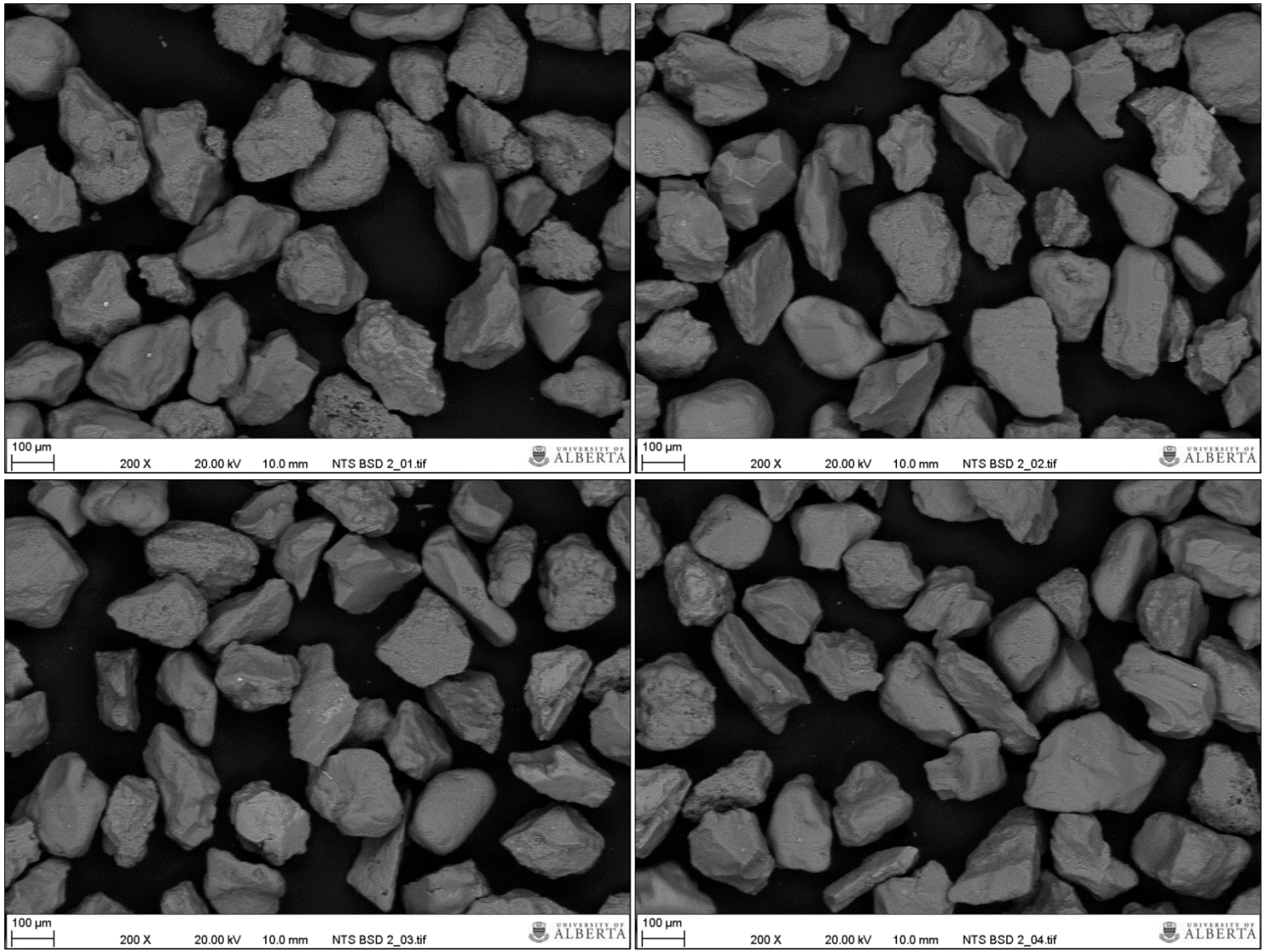


Tailings Beach Sand Imaged at 200x Magnification in Backscatter Mode

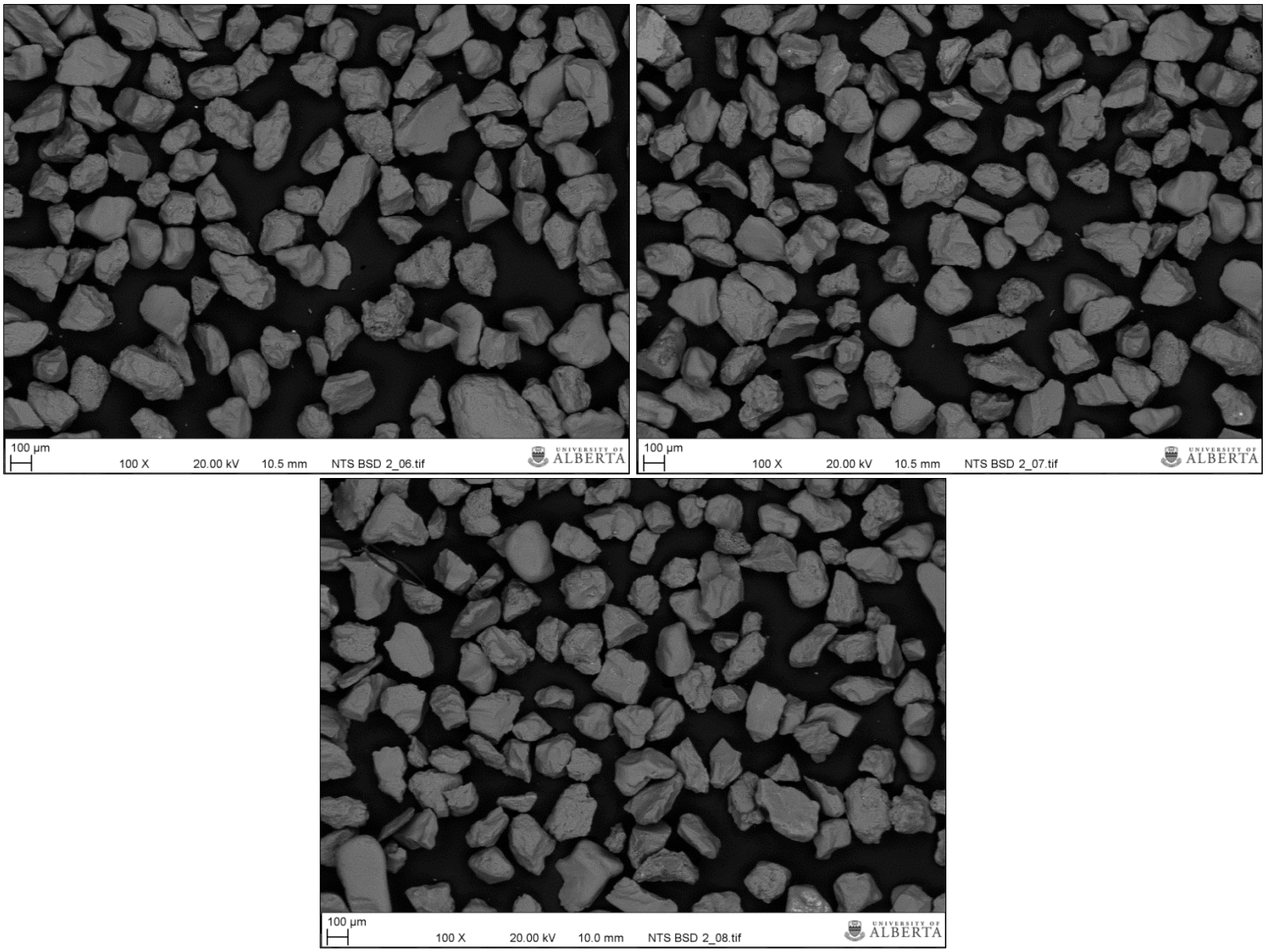


Tailings Beach Sand Imaged at 100x Magnification in Backscatter Mode

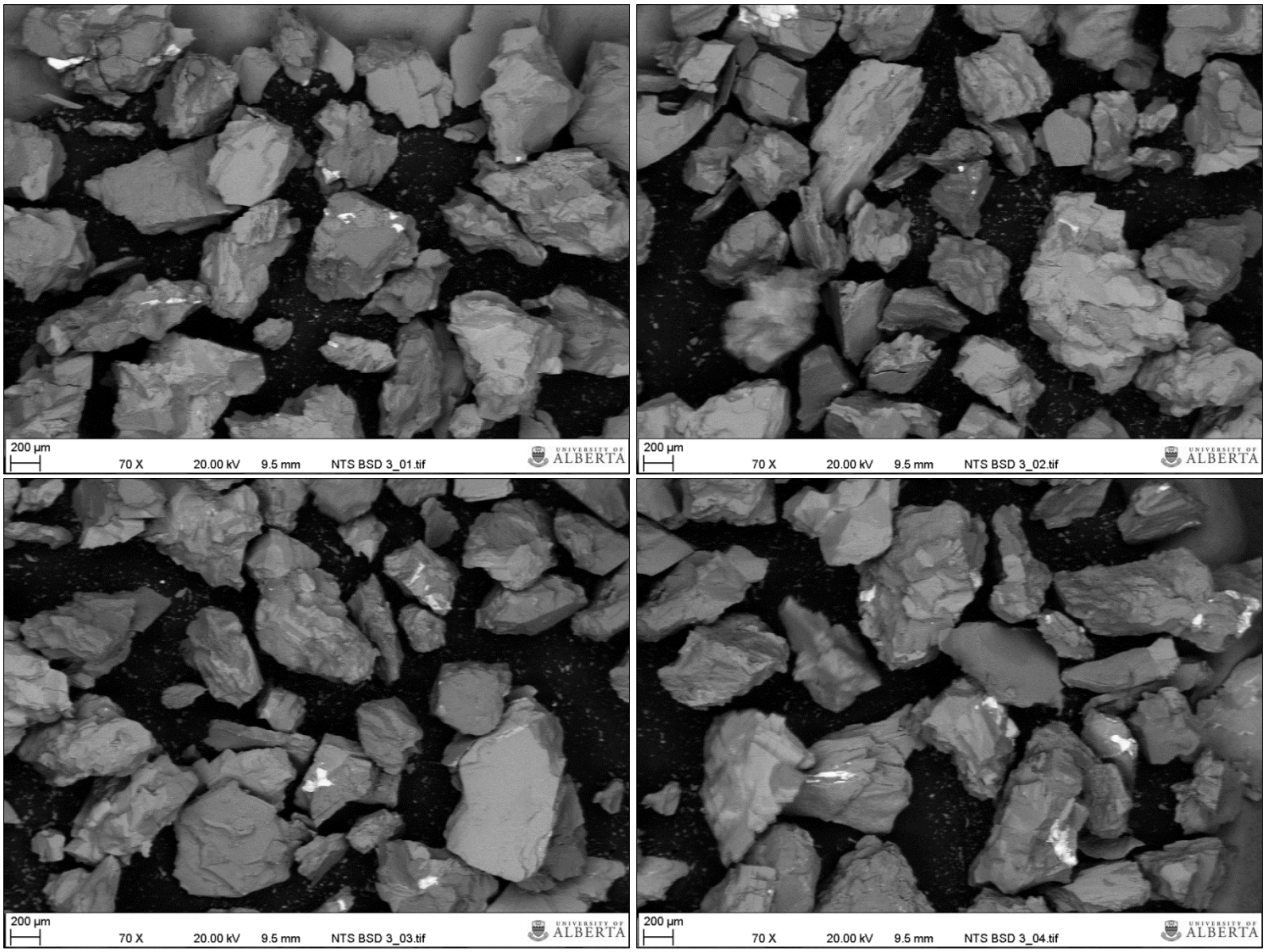


Granite Sand Imaged at 70x Magnification in Backscatter Mode

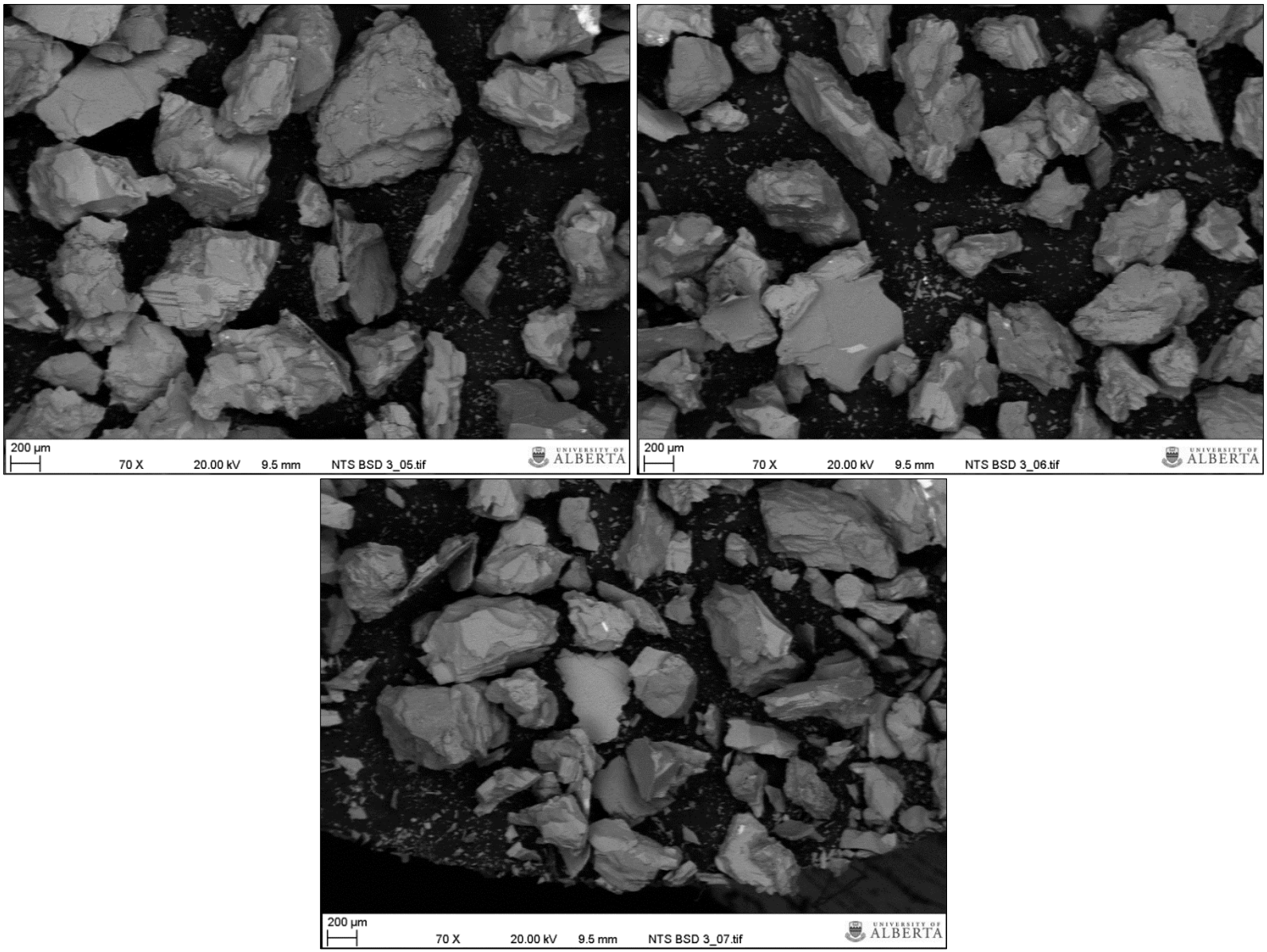


Granite Sand Imaged at 70x Magnification in Backscatter Mode

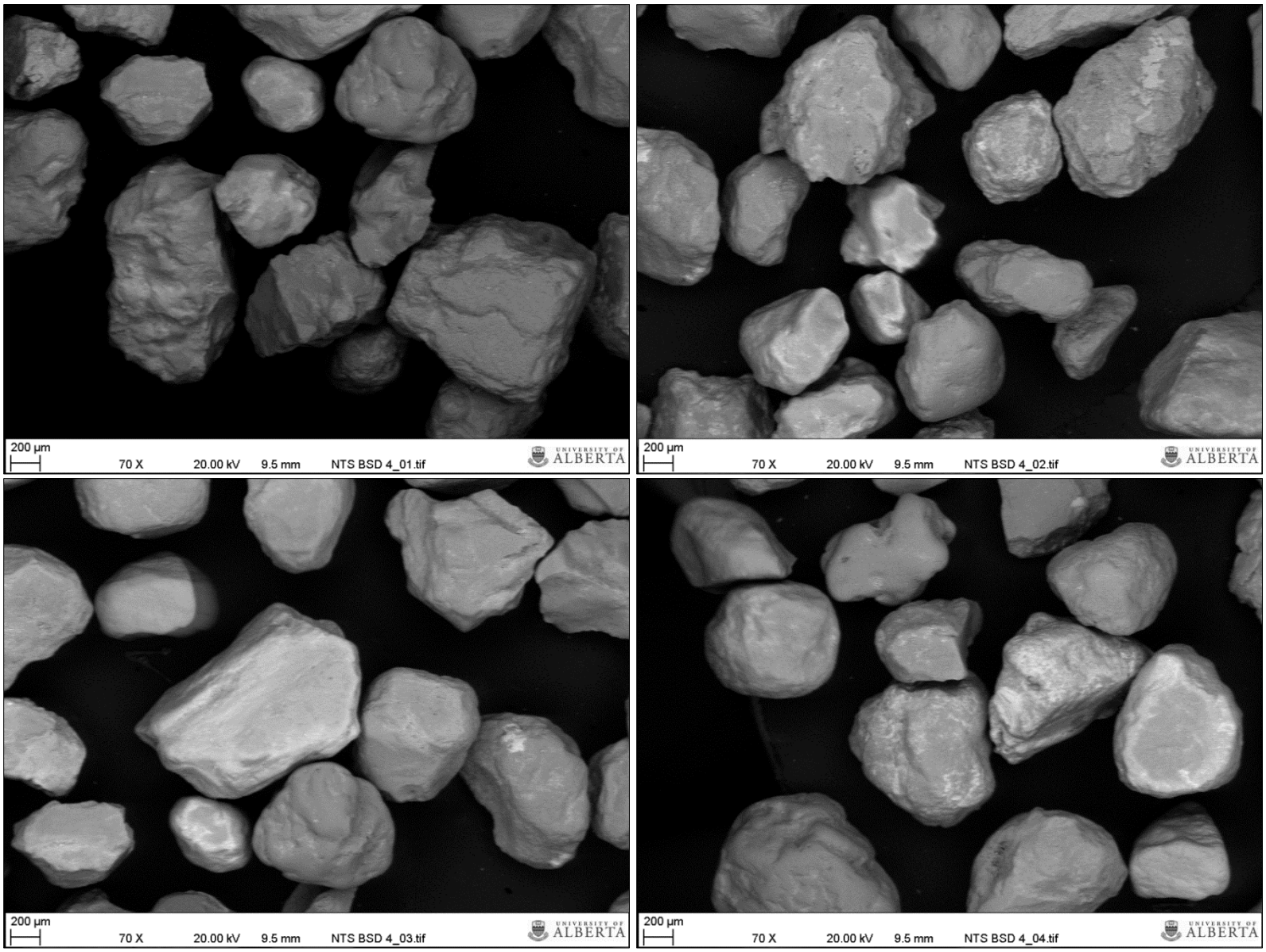


Raw Oil Sand Imaged at 70x Magnification in Backscatter Mode

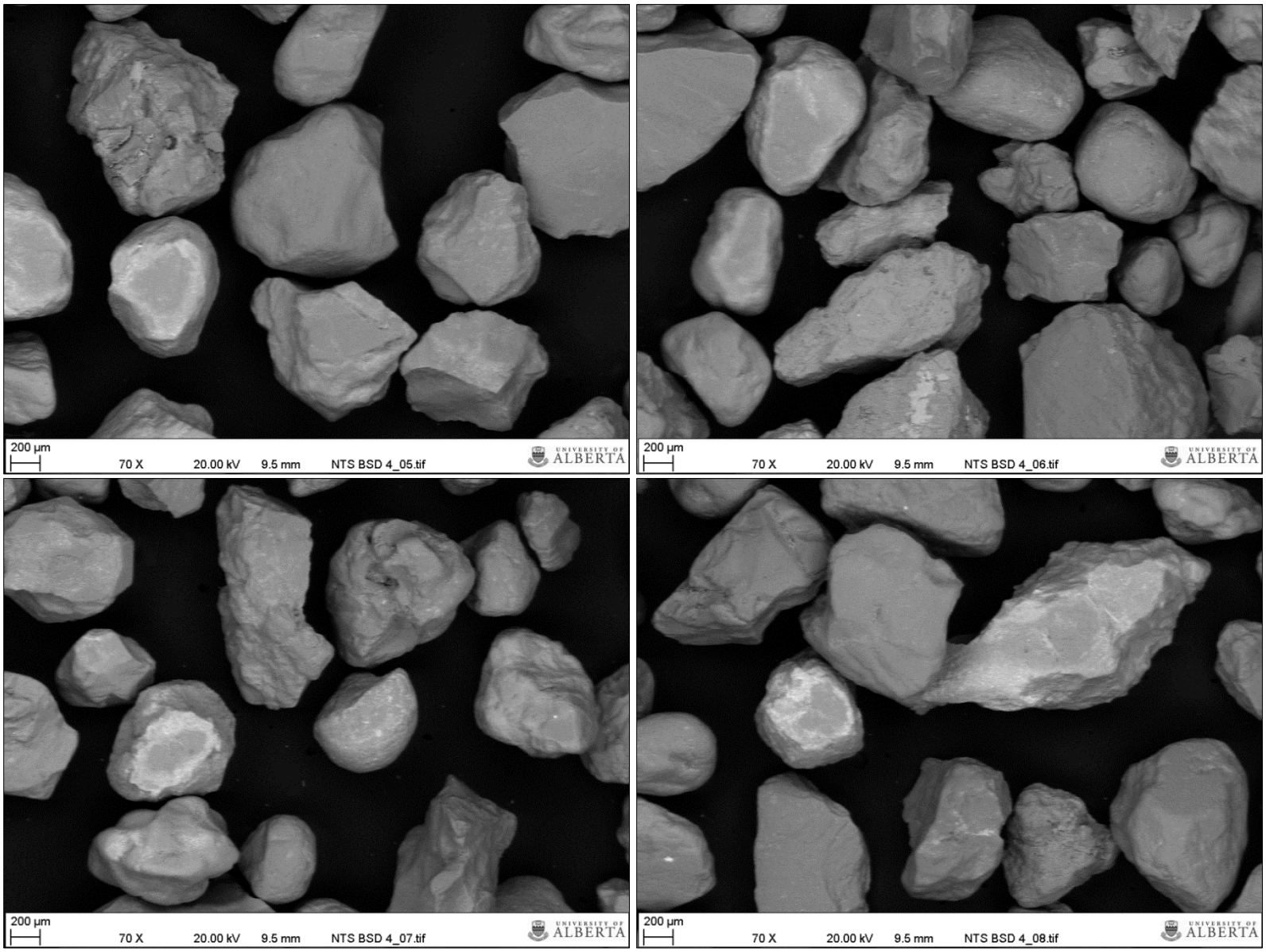


Raw Oil Sand Imaged at 70x Magnification in Backscatter Mode

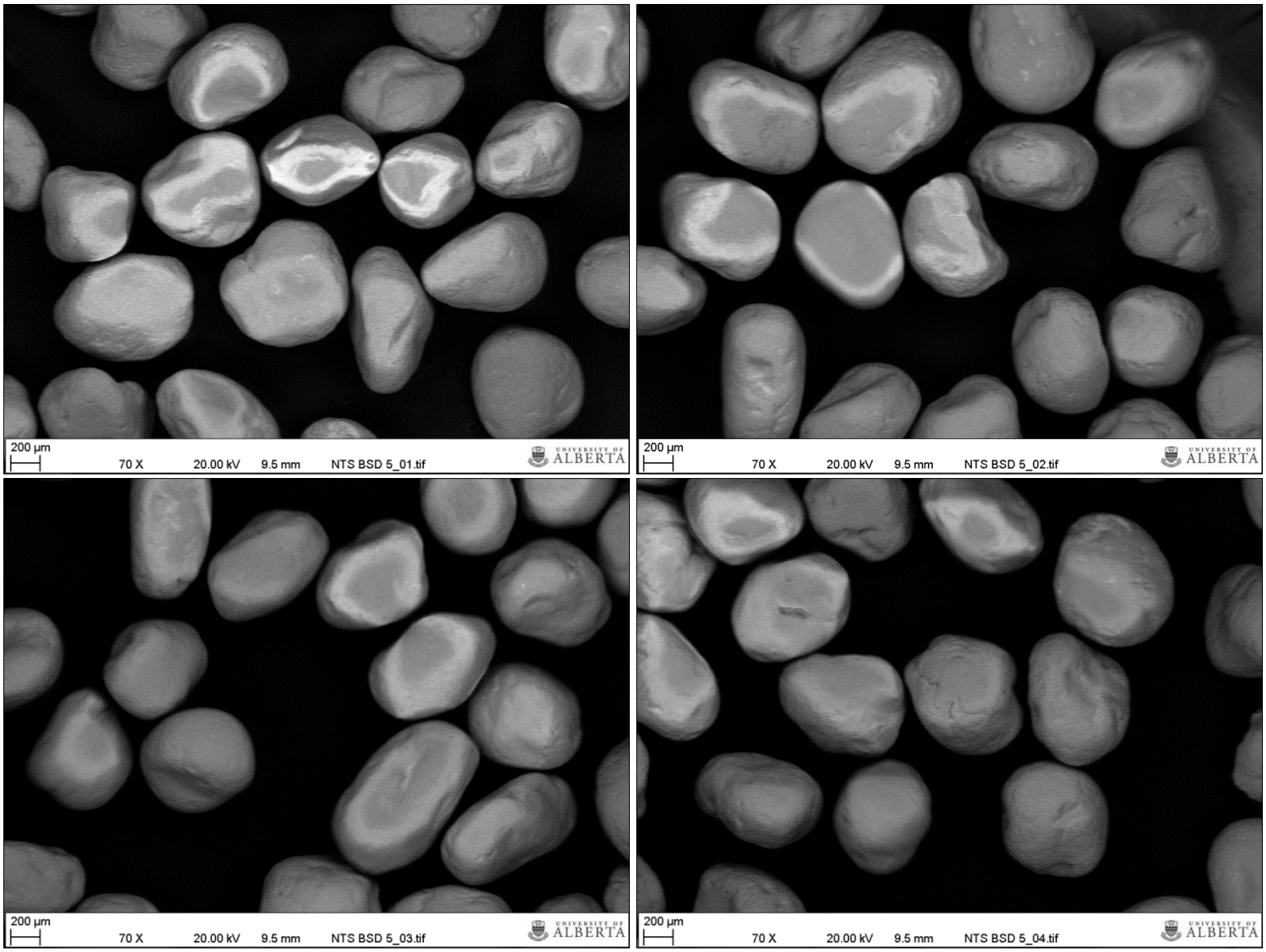


Silica Sand Imaged at 70x Magnification in Backscatter Mode

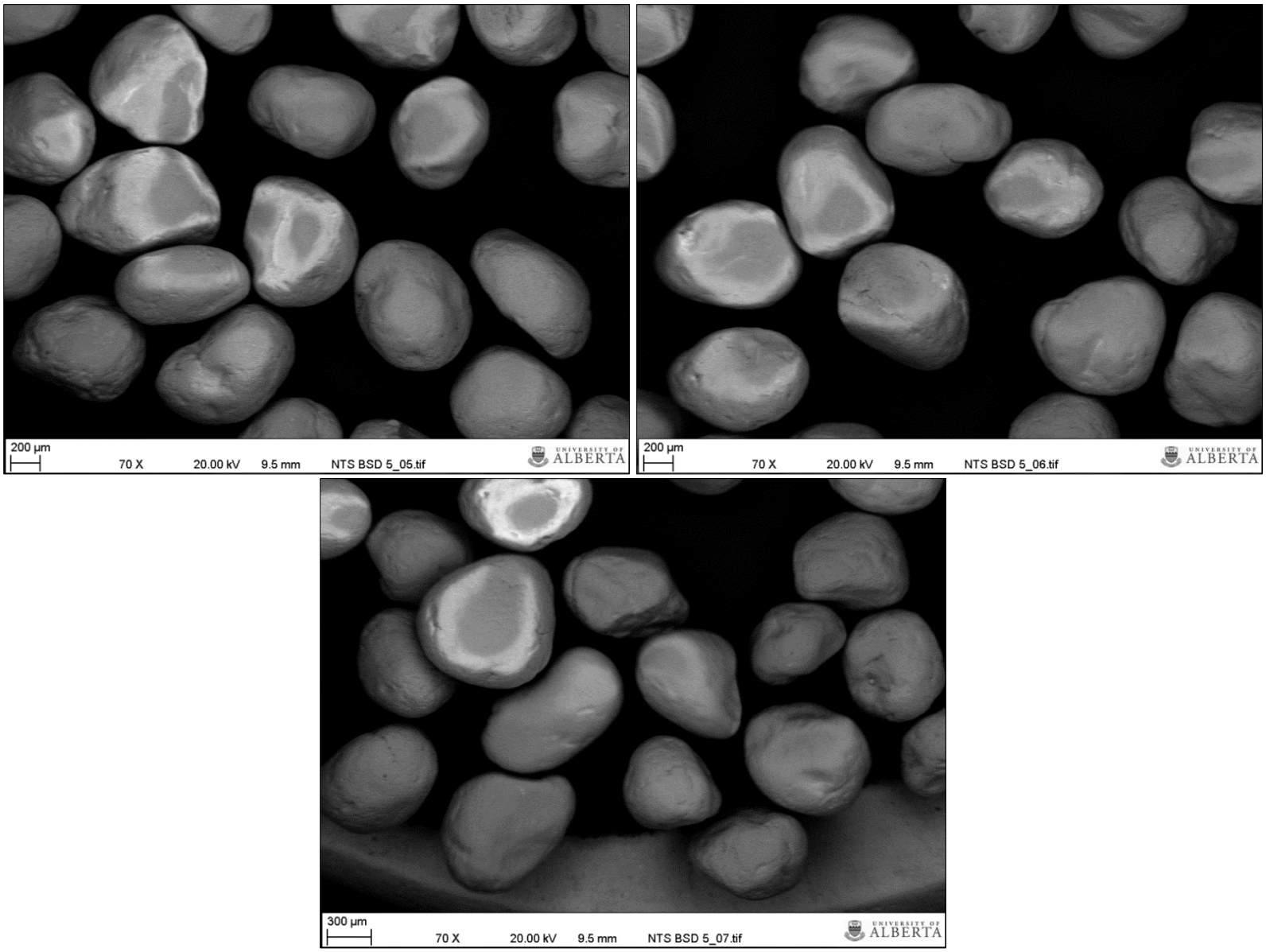


Silica Sand Imaged at 70x Magnification in Backscatter Mode

## Appendix C - Additional Wear Test Mass Loss Information

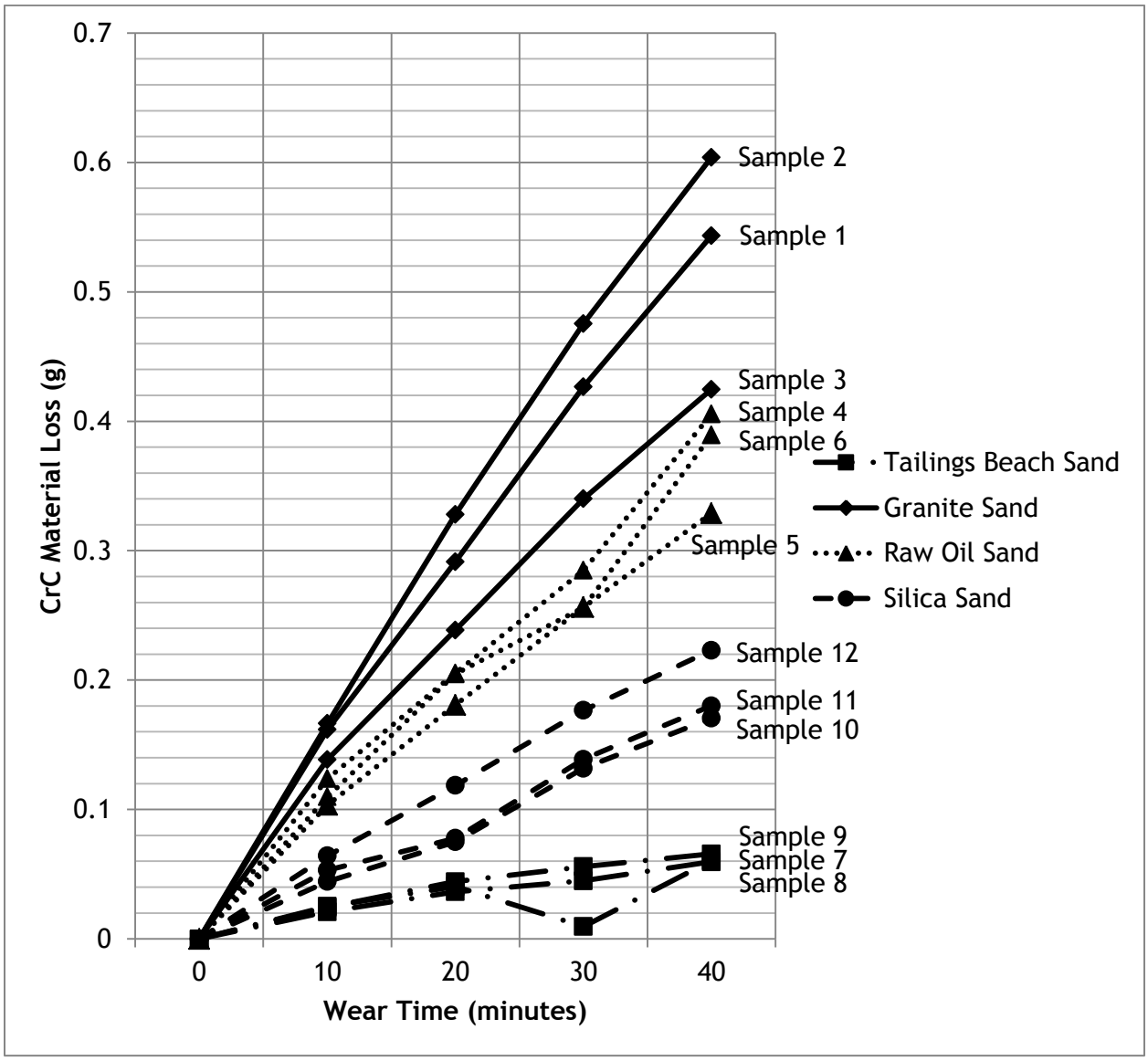


Mass Loss by Sample

Mass of Sample by Test Interval (mins)

| | Sample | Original | 10 | 20 | 30 | 40 |
|---|---|---|---|---|---|---|
| Tailings Beach Sand | 1 | 316.7534 | 316.7324 | 316.717 | 316.7085 | 316.6938 |
| | 2 | 319.0939 | 319.0695 | 319.0497 | 319.0381 | 319.0282 |
| | 3 | 313.2076 | 313.1824 | 313.1671 | 313.198 | 313.1471 |
| Granite Sand | 4 | 316.0599 | 315.8981 | 315.7684 | 315.6332 | 315.5164 |
| | 5 | 299.0649 | 298.9263 | 298.8263 | 298.7248 | 298.6402 |
| | 6 | 313.8398 | 313.6733 | 313.5118 | 313.3643 | 313.2358 |
| Raw Oil Sand | 7 | 317.1545 | 317.0447 | 316.9497 | 316.8985 | 316.7652 |
| | 8 | 314.5731 | 314.4696 | 314.3923 | 314.3168 | 314.2442 |
| | 9 | 317.4231 | 317.2993 | 317.2177 | 317.1383 | 317.0175 |
| Silica Sand | 10 | 318.3021 | 318.249 | 318.2243 | 318.1633 | 318.122 |
| | 11 | 318.5626 | 318.4984 | 318.444 | 318.386 | 318.3396 |
| | 12 | 313.809 | 313.7647 | 313.7339 | 313.6772 | 313.6384 |

On the following pages of Appendix C are full page images of the chrome carbide samples, after undergoing 40 minutes of testing. One sample has been selected for each abrasive media type that best displays the modes of wear associated with that media.

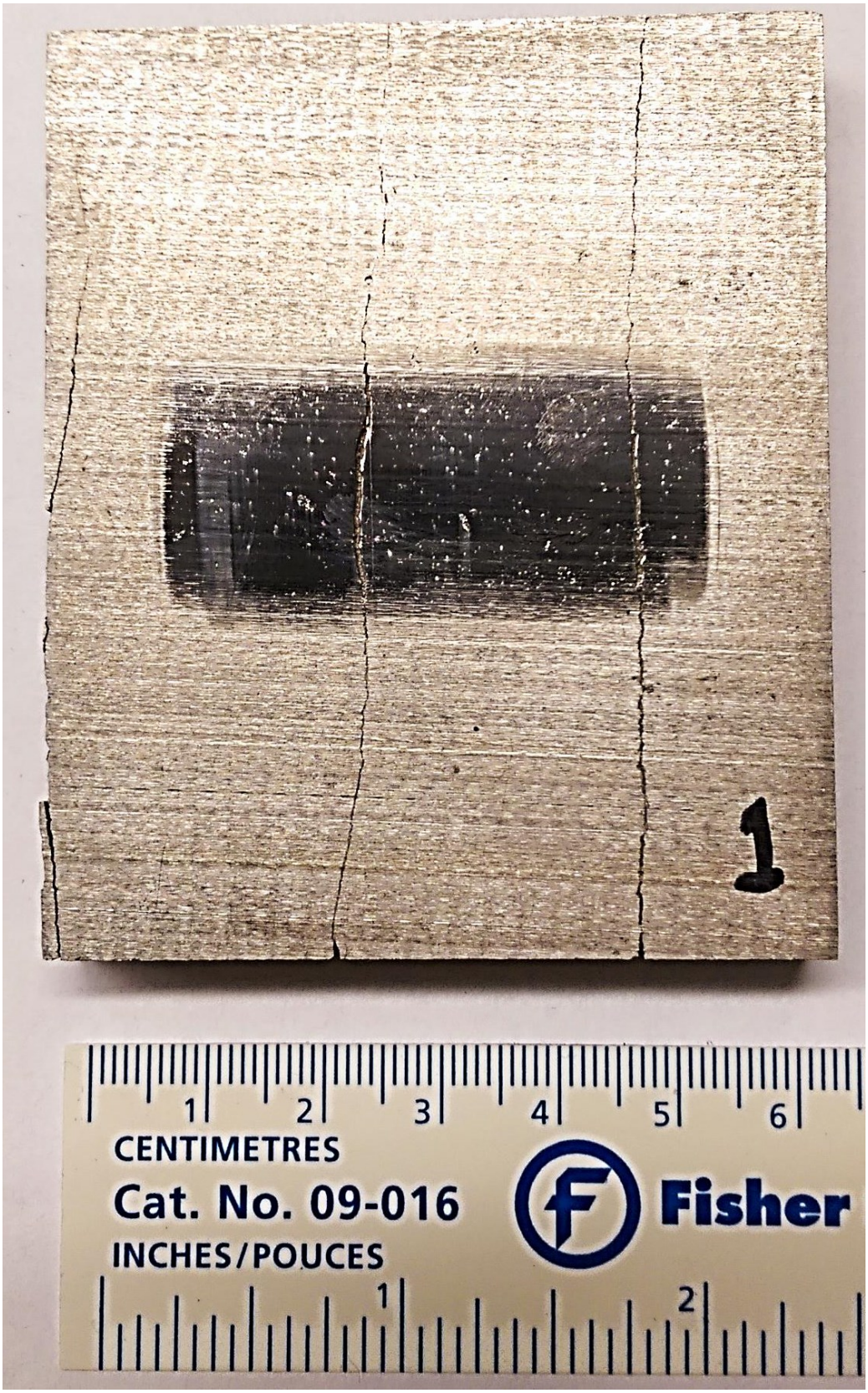


Chrome Carbide Sample Abraded by Tailings Beach Sand

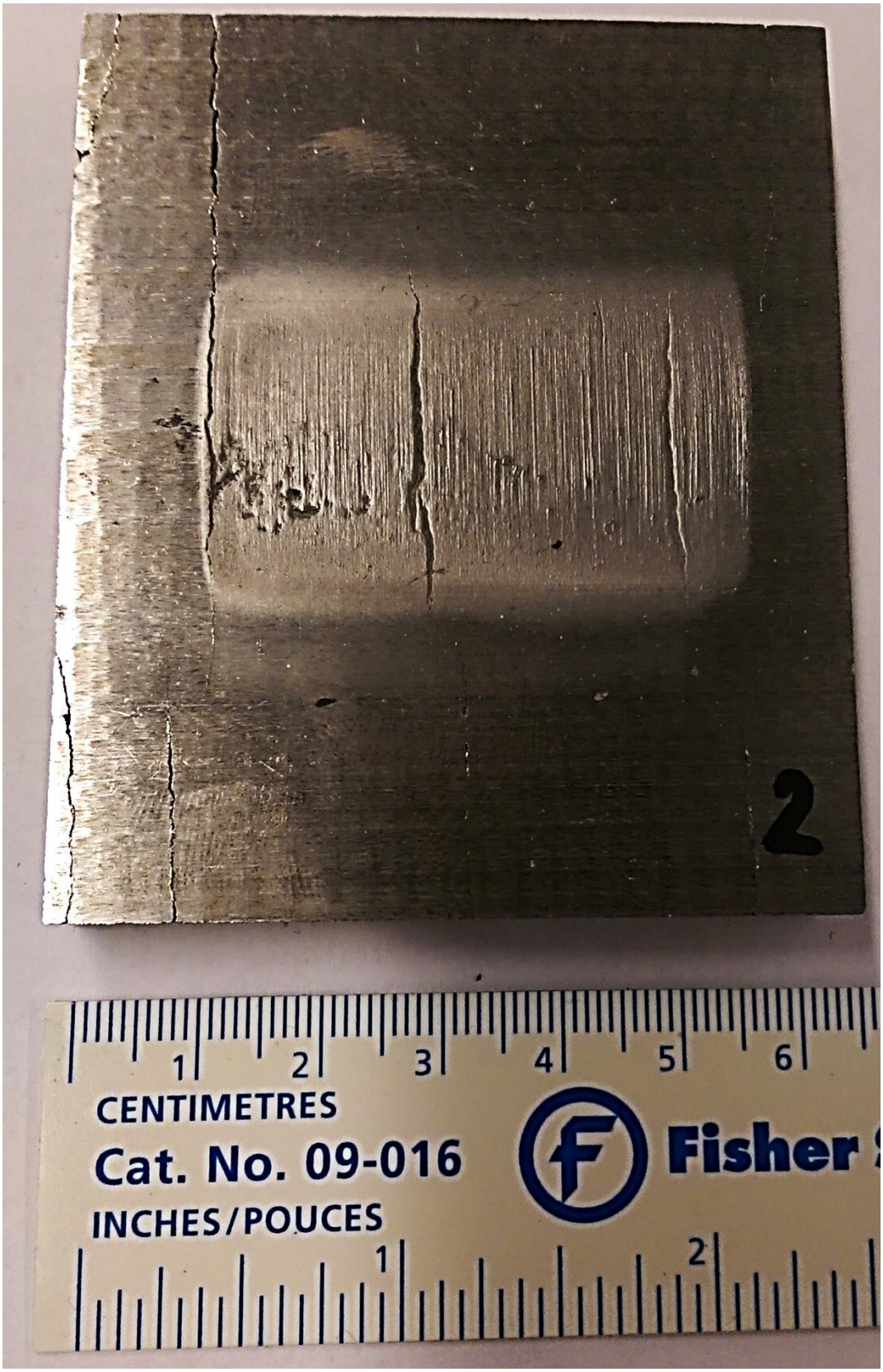


Chrome Carbide Sample Abraded by Granite Sand

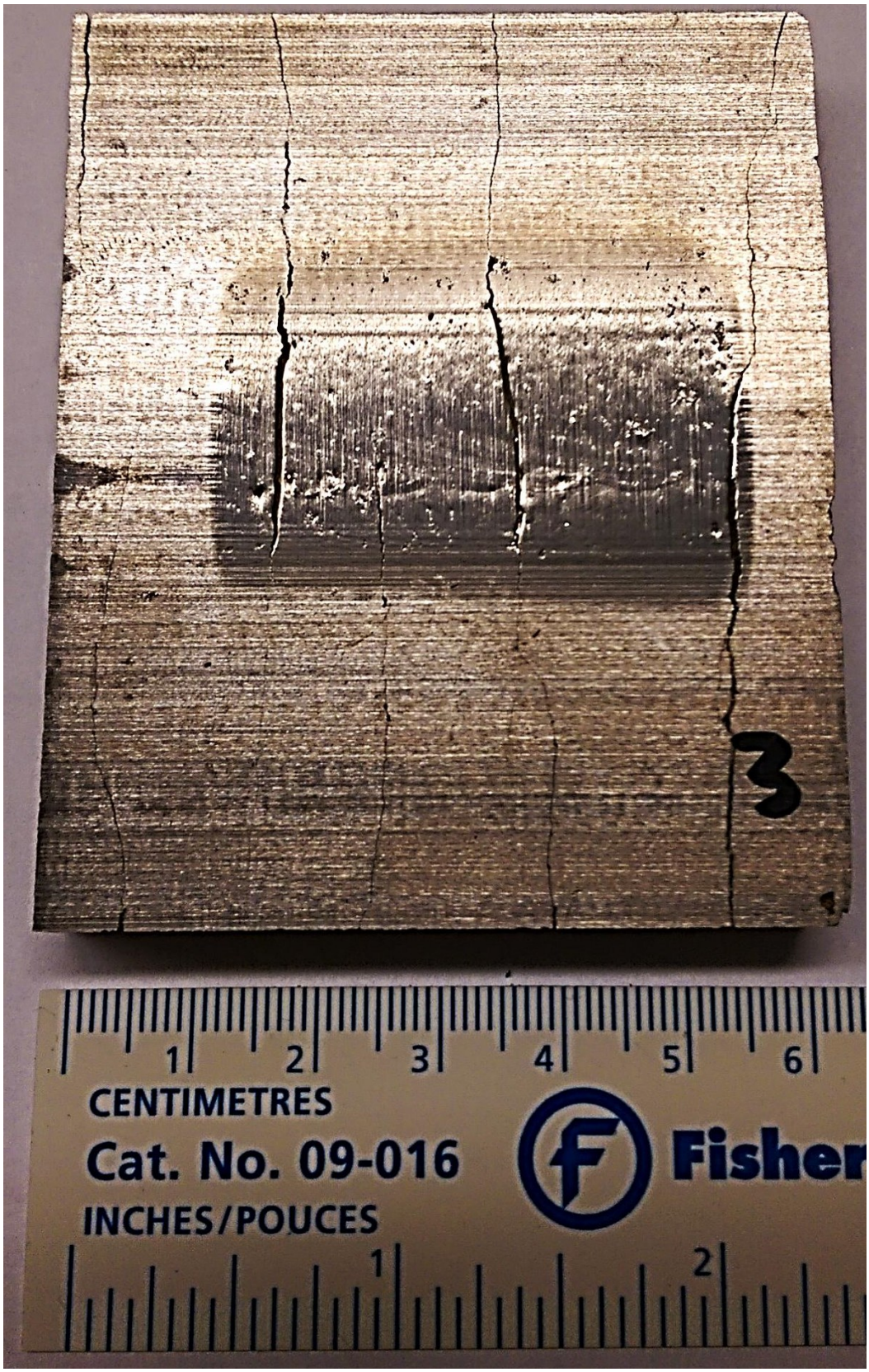


Chrome Carbide Sample Abraded by Raw Oil Sand

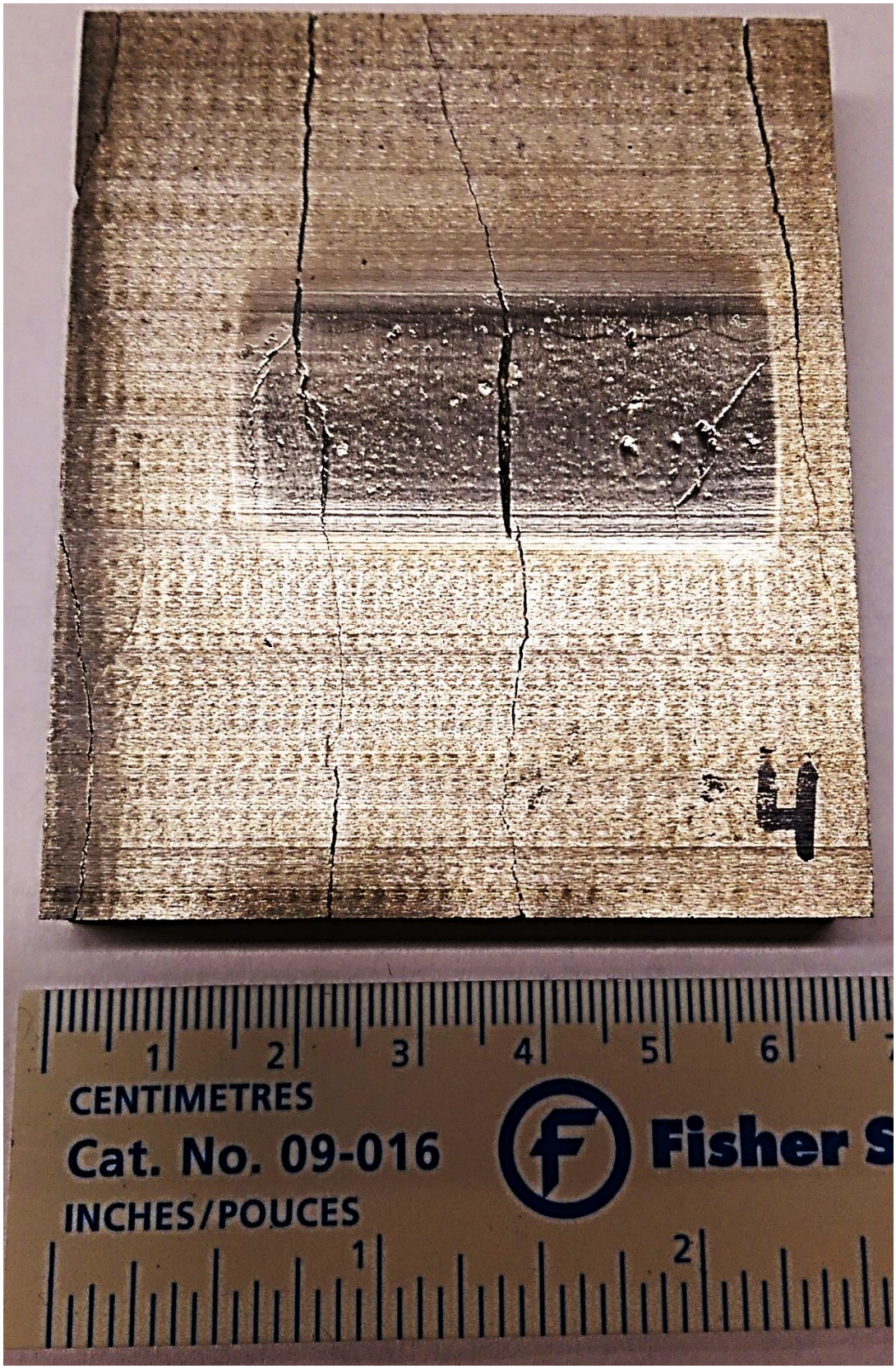


Chrome Carbide Sample Abraded by Silica Sand

## Appendix D - Scanning Electron Microcope Images Used for Analysis

The purpose of this appendix is to provide the reader with a general idea of the type of images gathered, and how they appear when edited for image analysis. This is only a small selection of photos however, as over 300 images were used in this project.

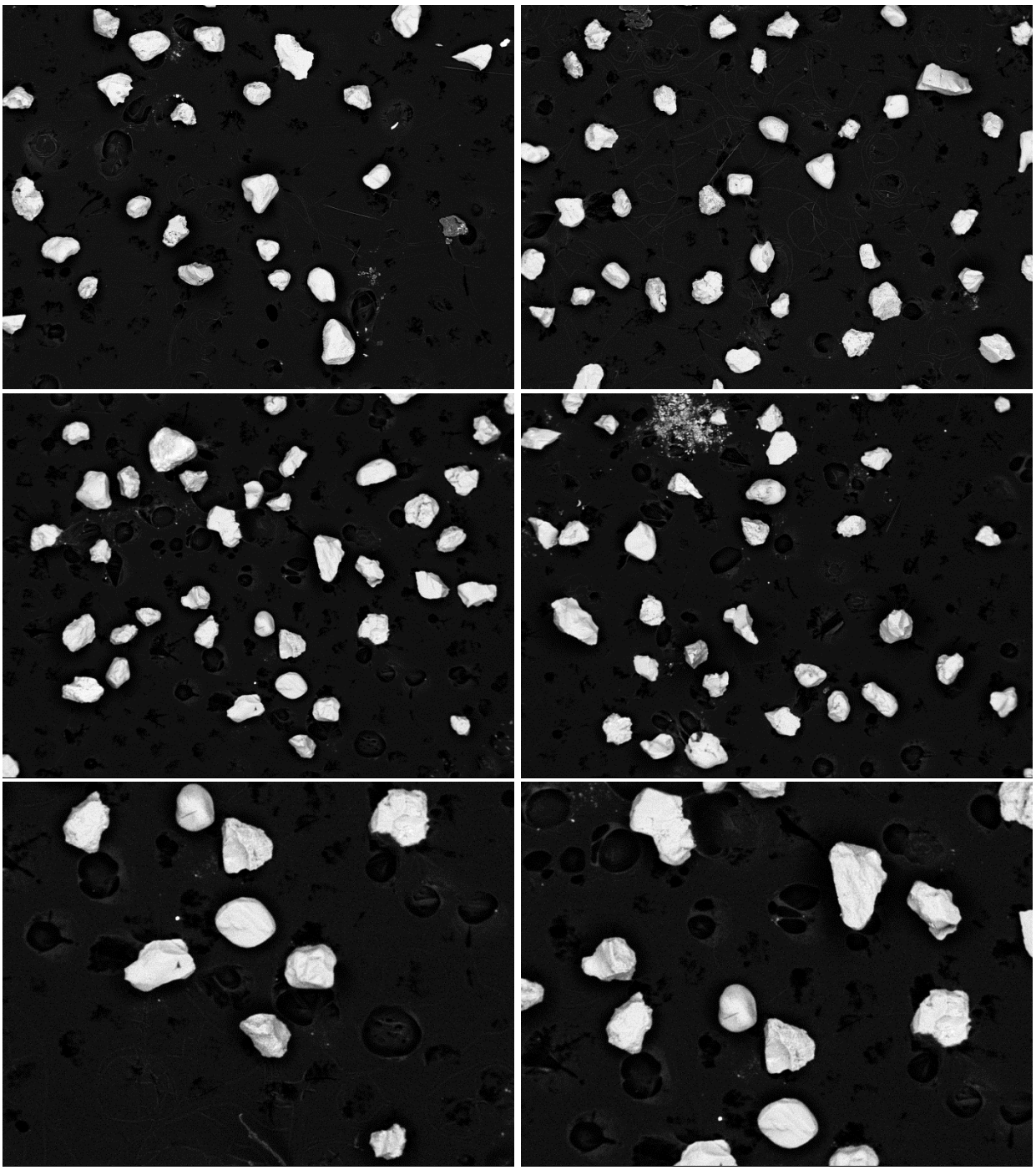

Unaltered SEM Images of Tailings Beach Sand

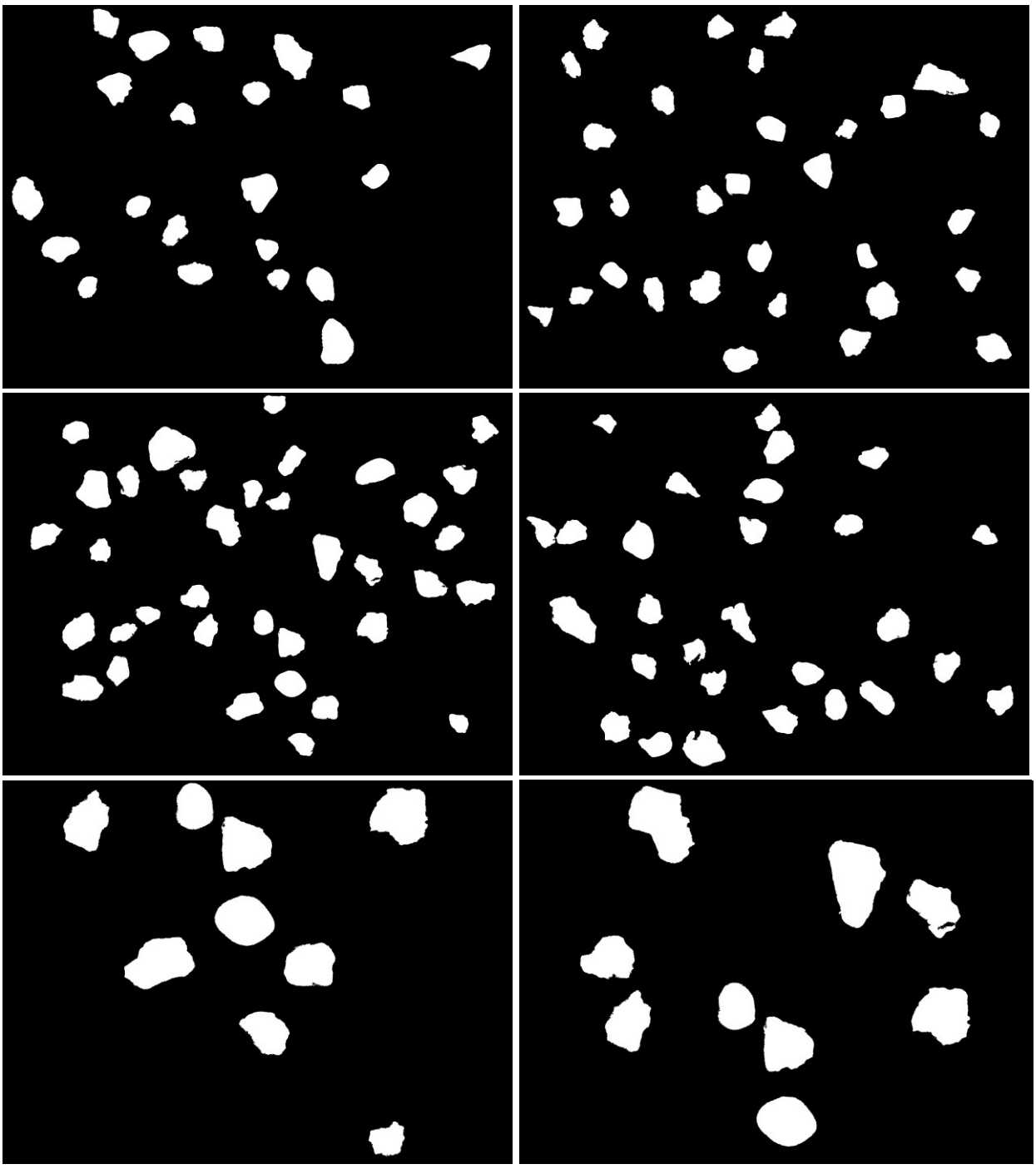

Copies of the Tailings Beach Sand Images from the Previous Page, Edited to Prepare for Particle Boundary Detection

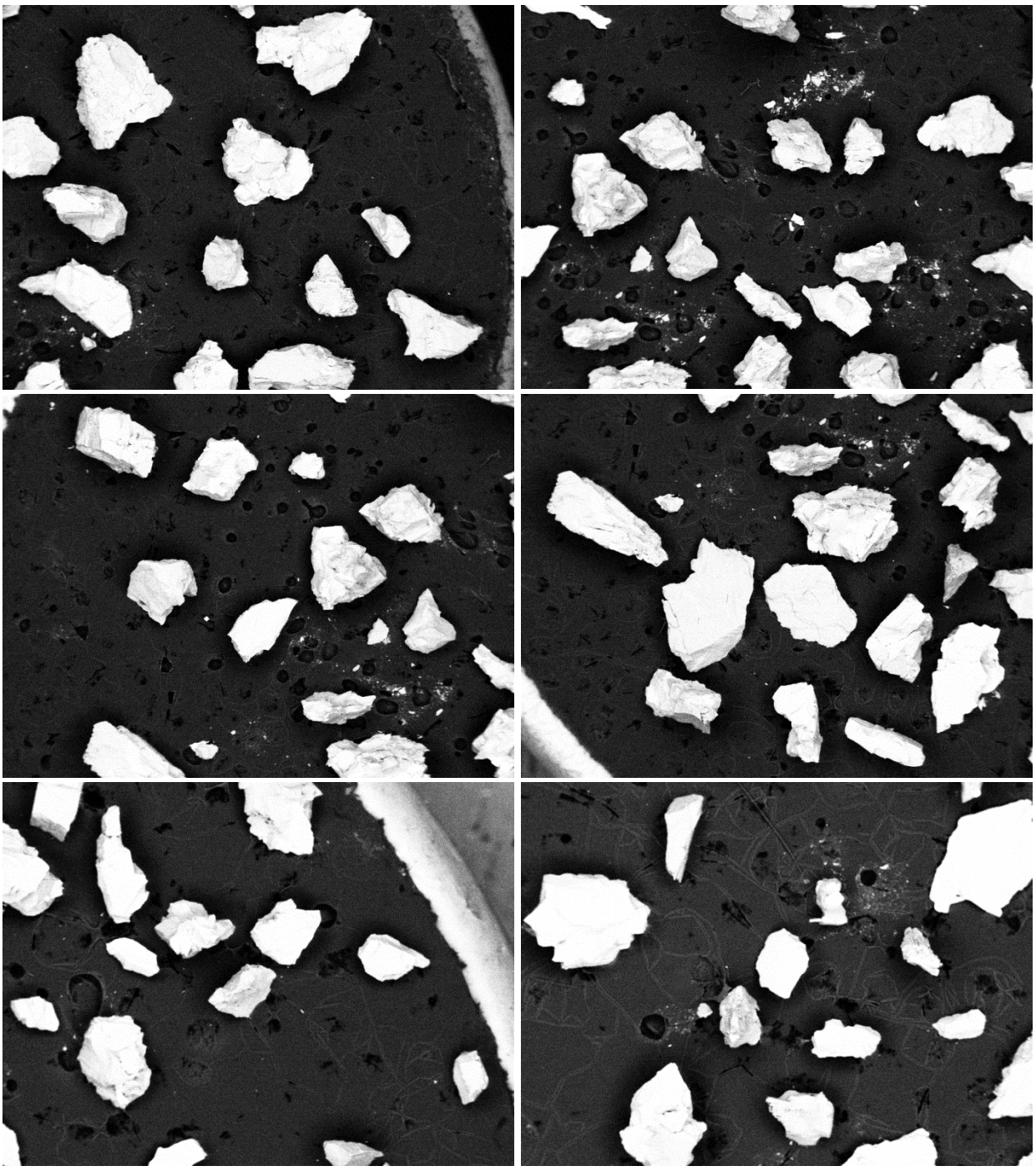

Unaltered SEM Images of Granite Sand

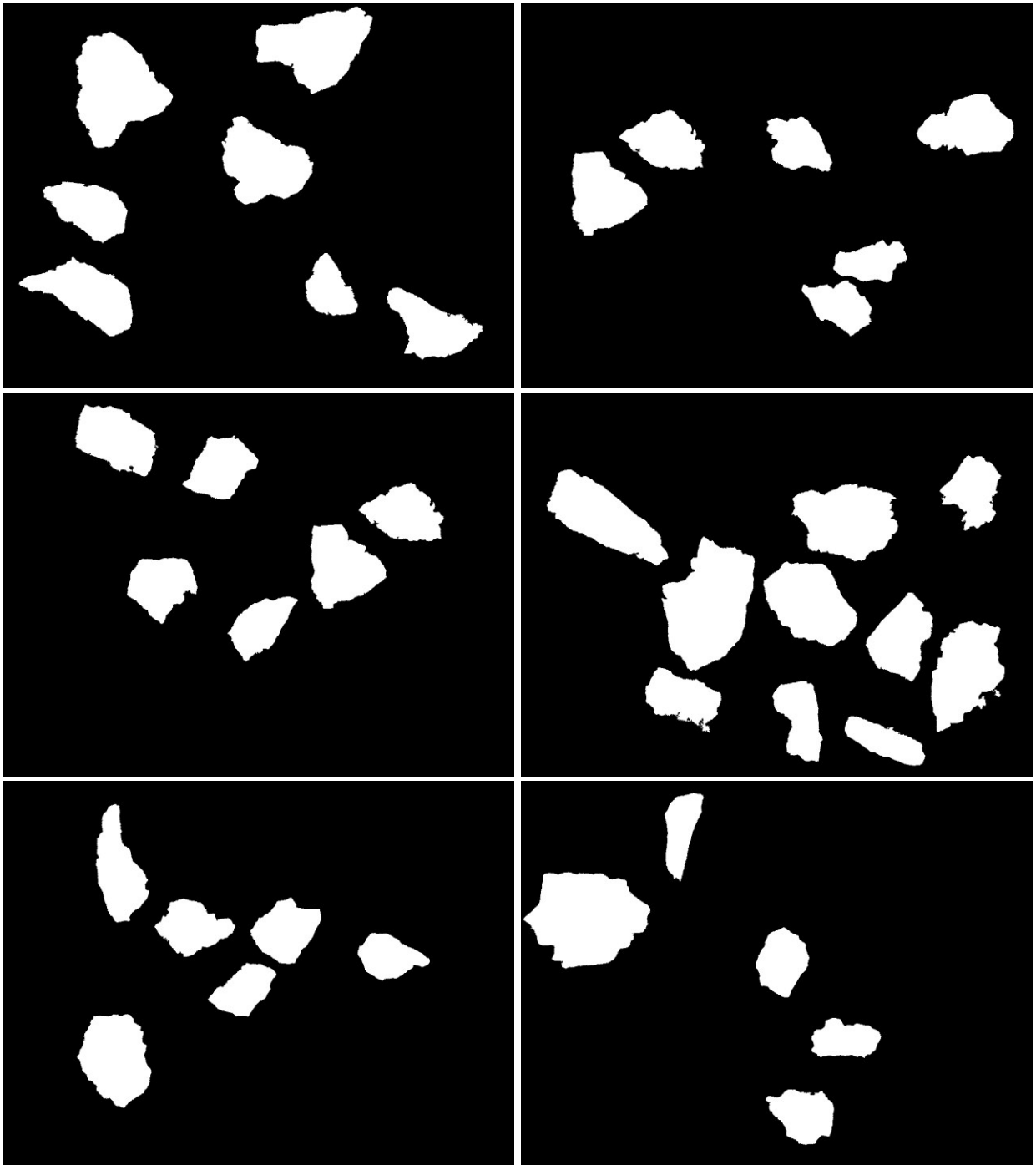

Copies of the Granite Sand Images from the Previous Page, Edited to Prepare for Particle Boundary Detection

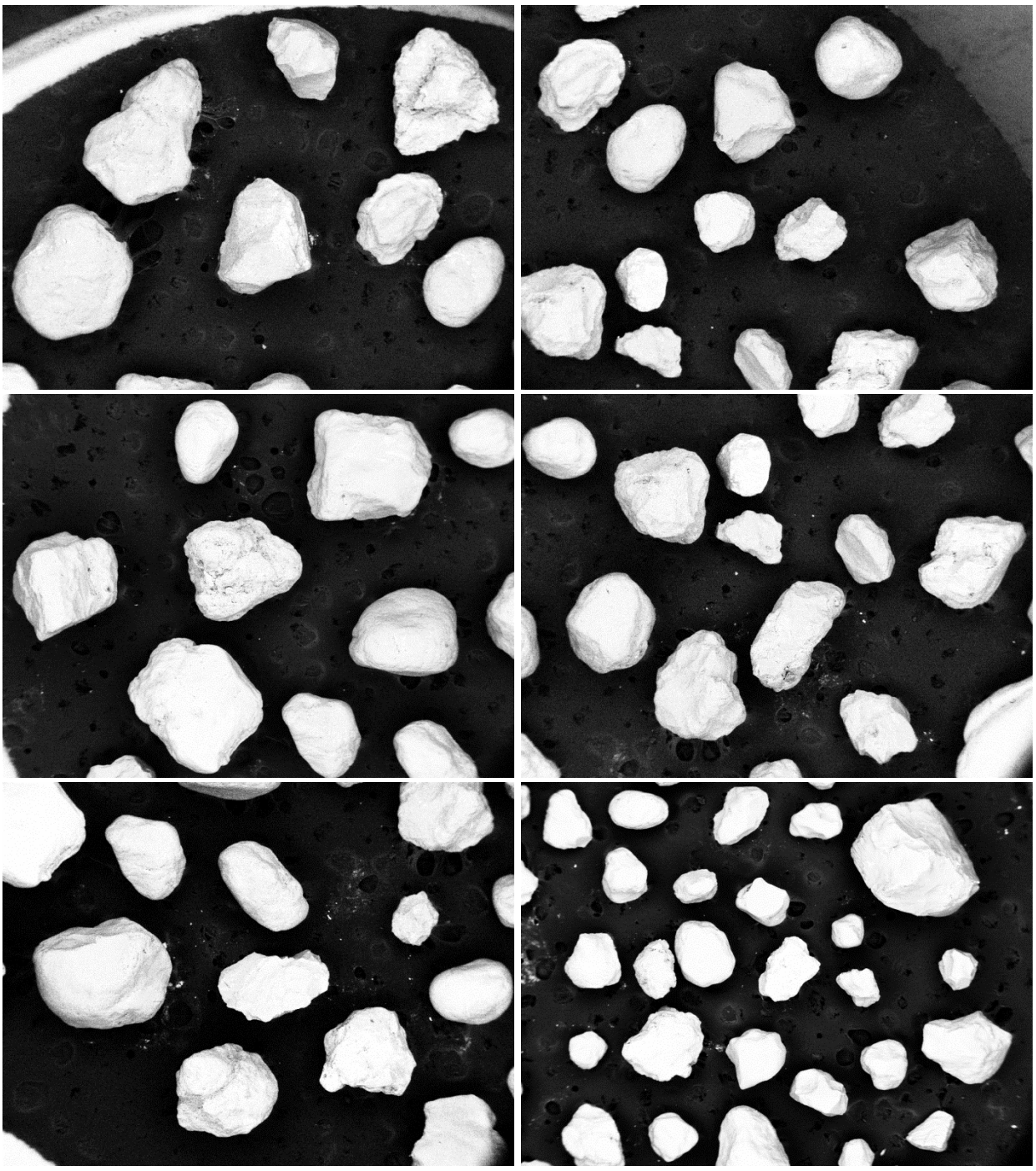

Unaltered SEM Images of Raw Oil Sand

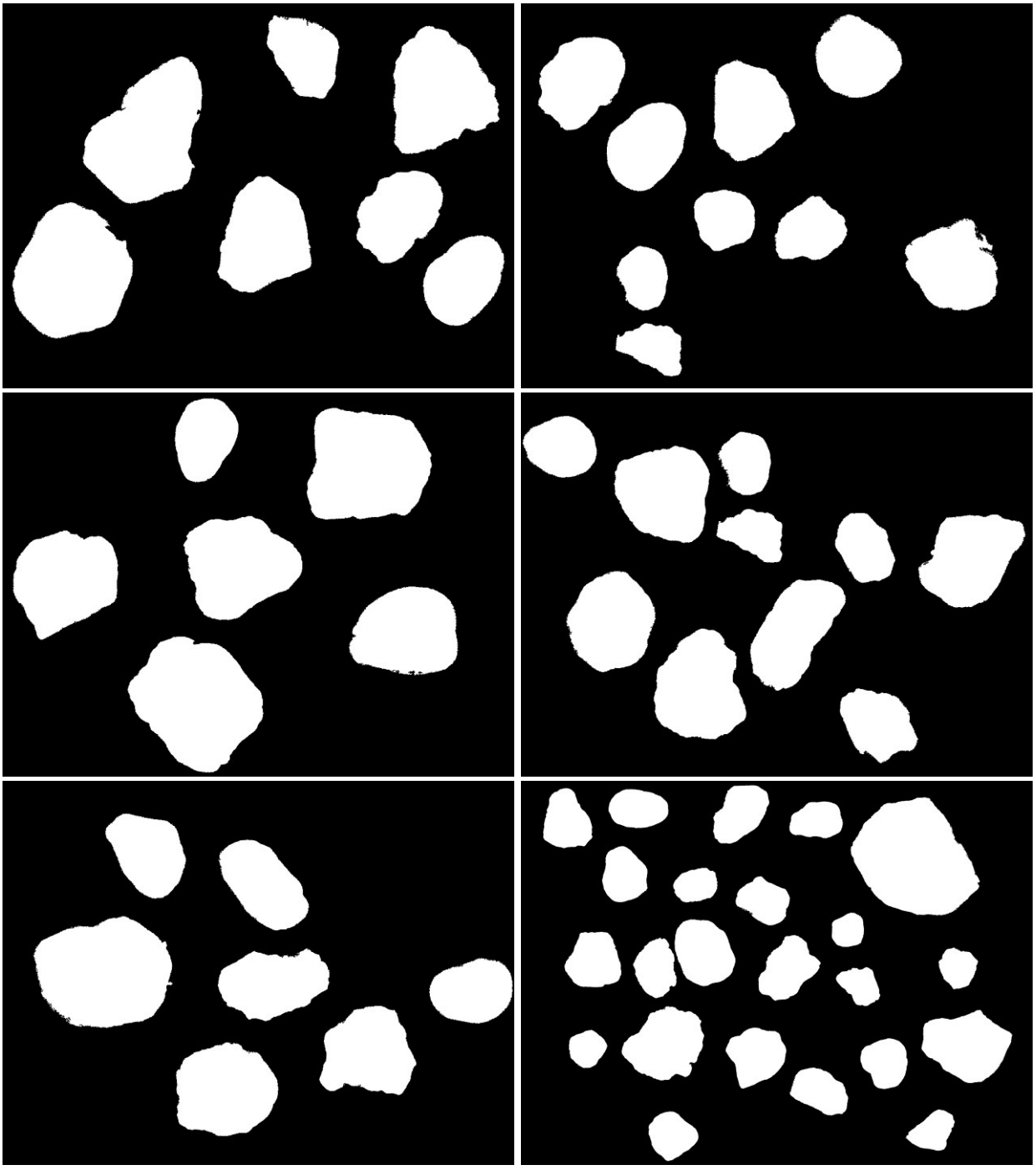

Copies of the Raw Oil Sand Images from the Previous Page, Edited to Prepare for Particle Boundary Detection

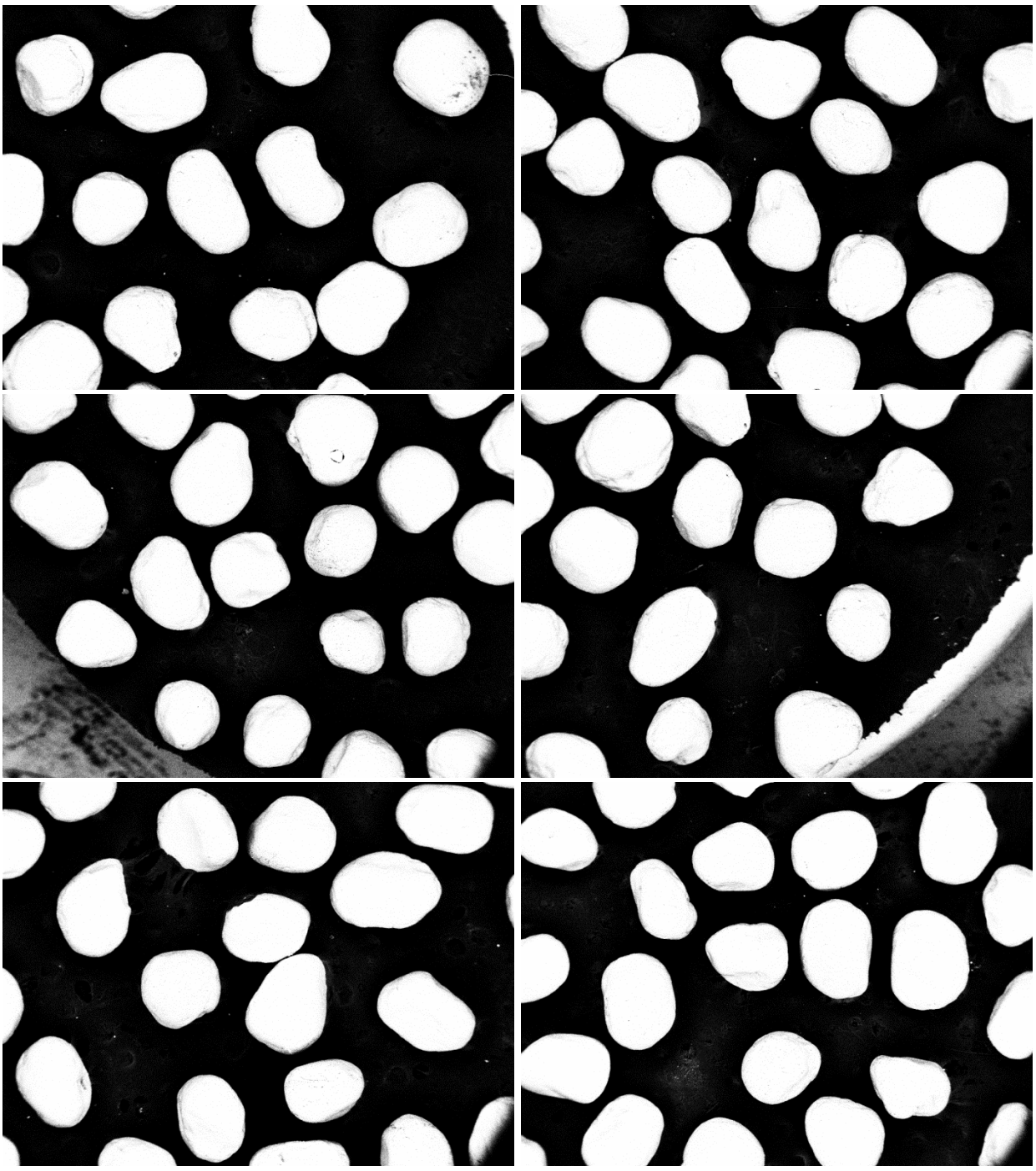

Unaltered SEM Images of Silica Sand

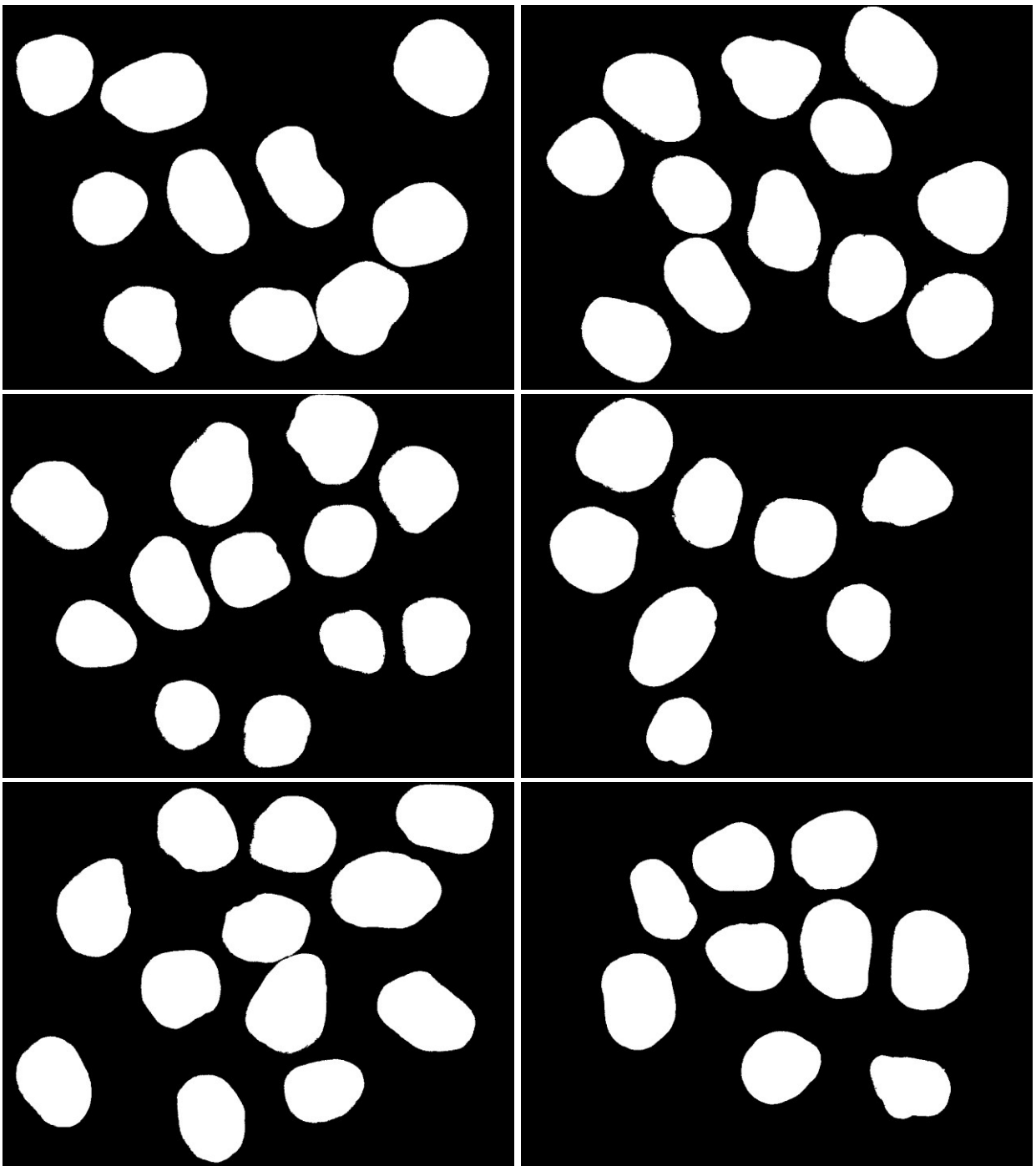

Copies of the Silica Sand Images from the Previous Page, Edited to Prepare for Particle Boundary Detection

## Appendix E - Correlation of Abrasive Wear Mass Loss with Shape Parameters, Including Tailings Beach Sand Results

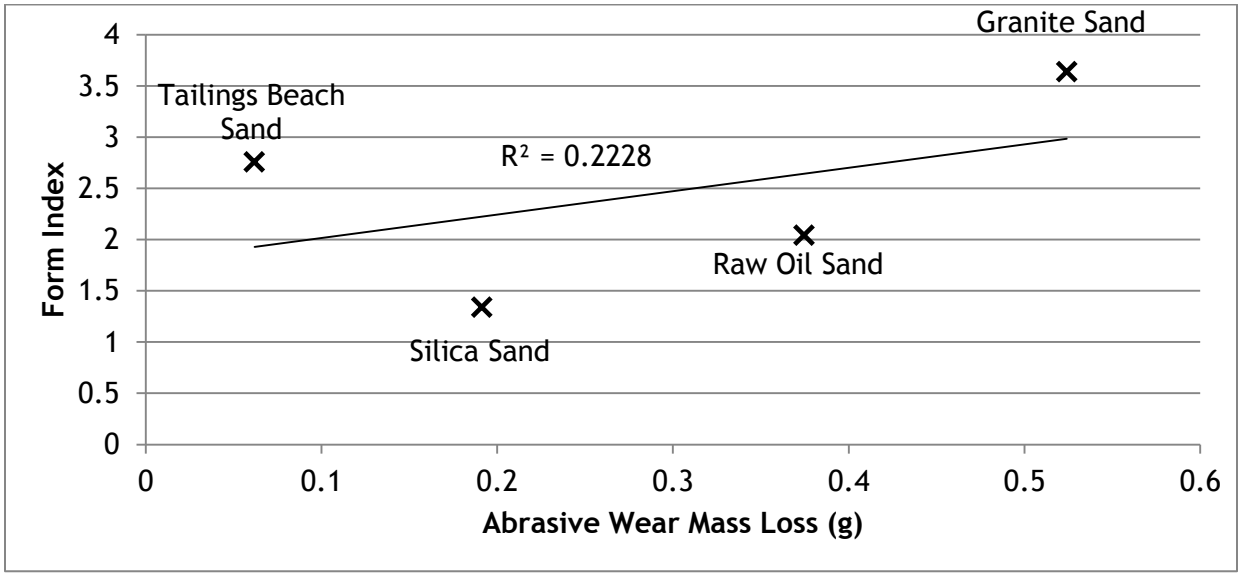


Form Index vs Abrasive Wear Mass Loss and Correlation

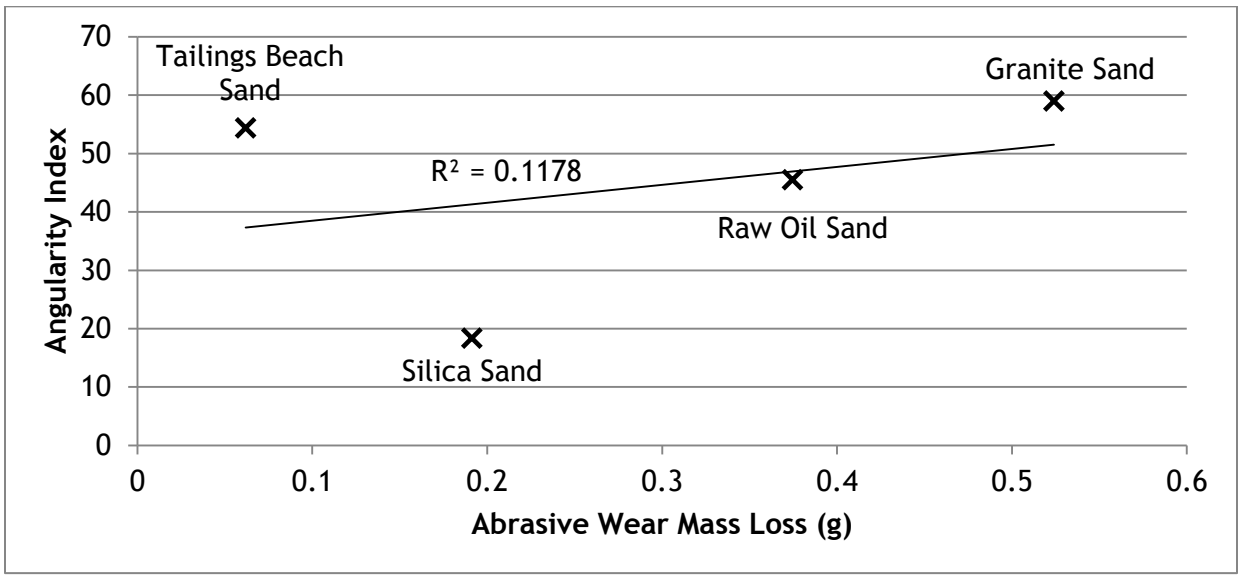


Angularity Index vs Abrasive Wear Mass Loss and Correlation

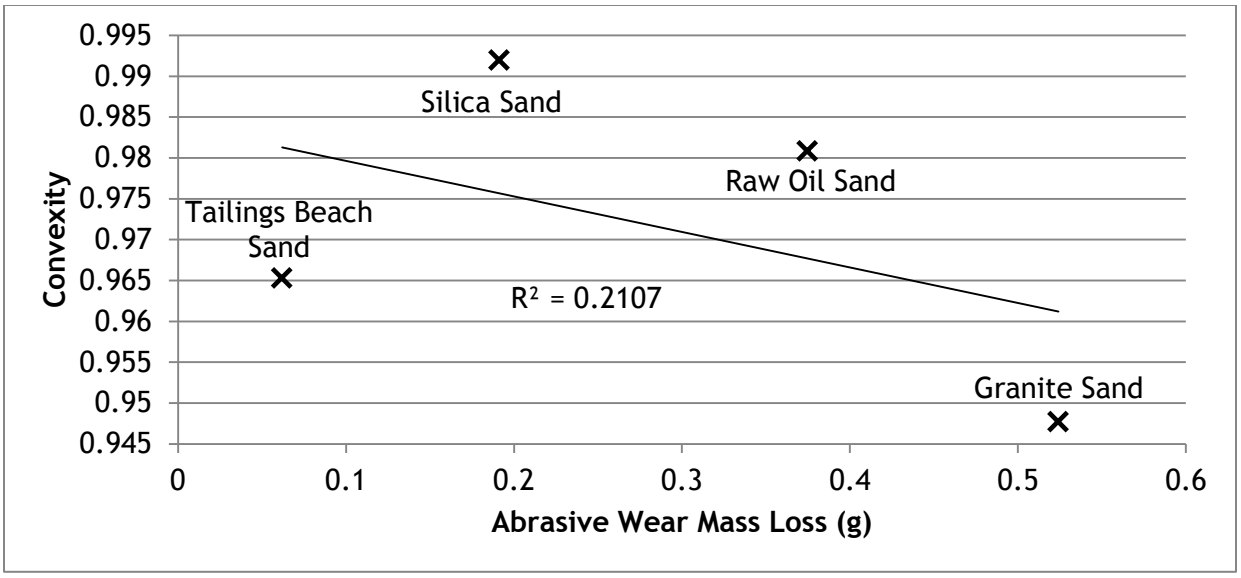


Convexity vs Abrasive Wear Mass Loss and Correlation

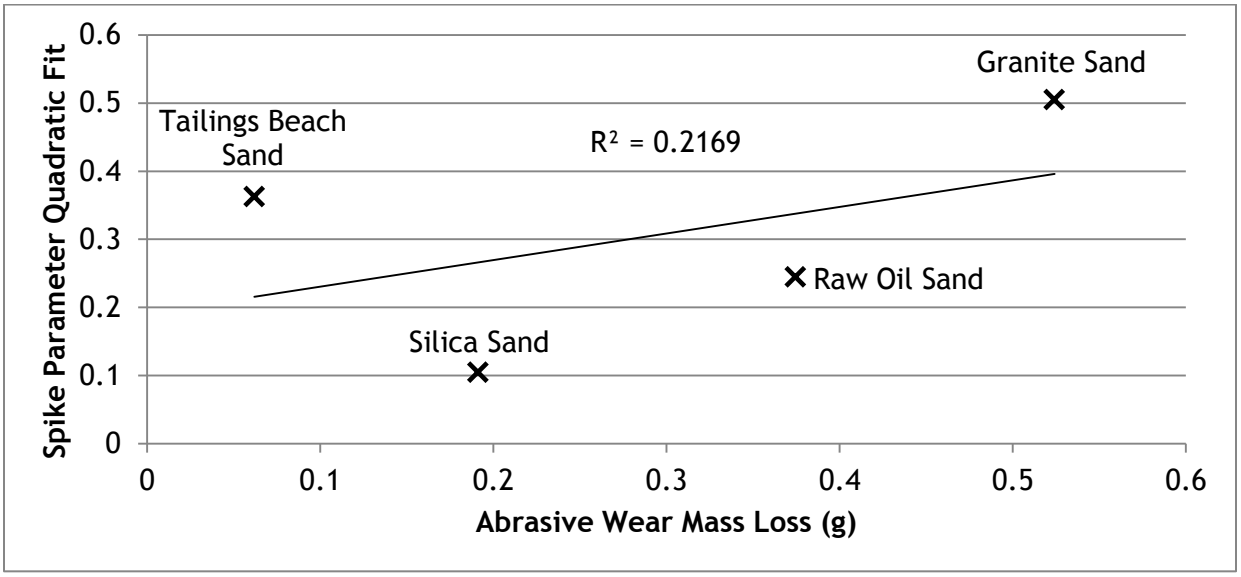


Spike Parameter Quadratic Fit vs Abrasive Wear Mass Loss and Correlation

## Appendix F - Correlation of Angle of Repose with Shape Parameters

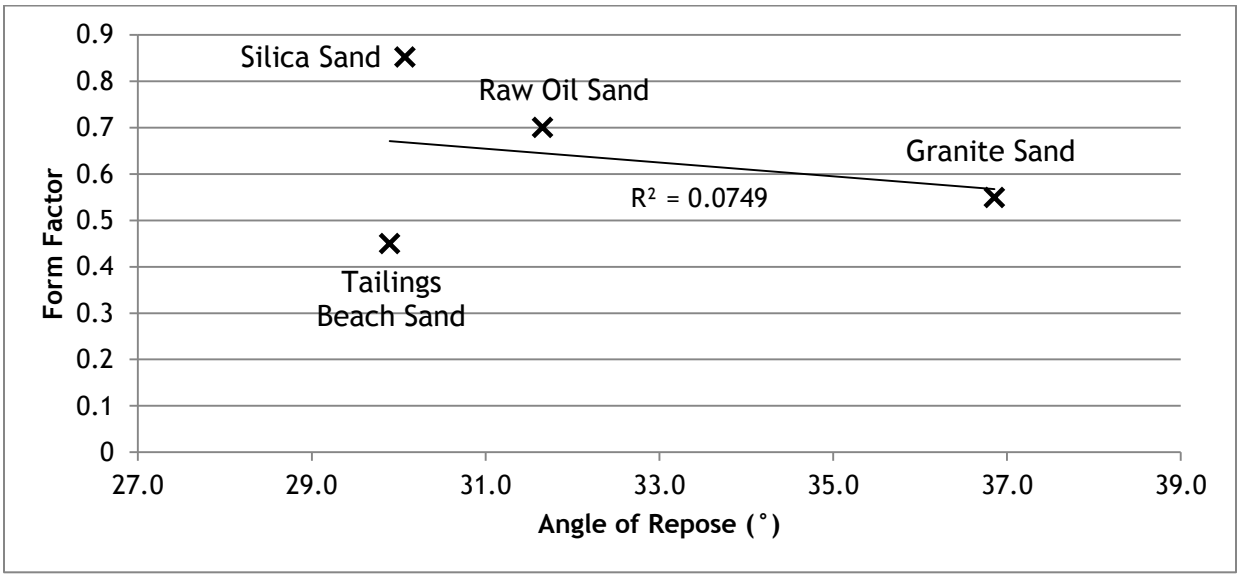


Form Factor vs Angle of Repose and Correlation

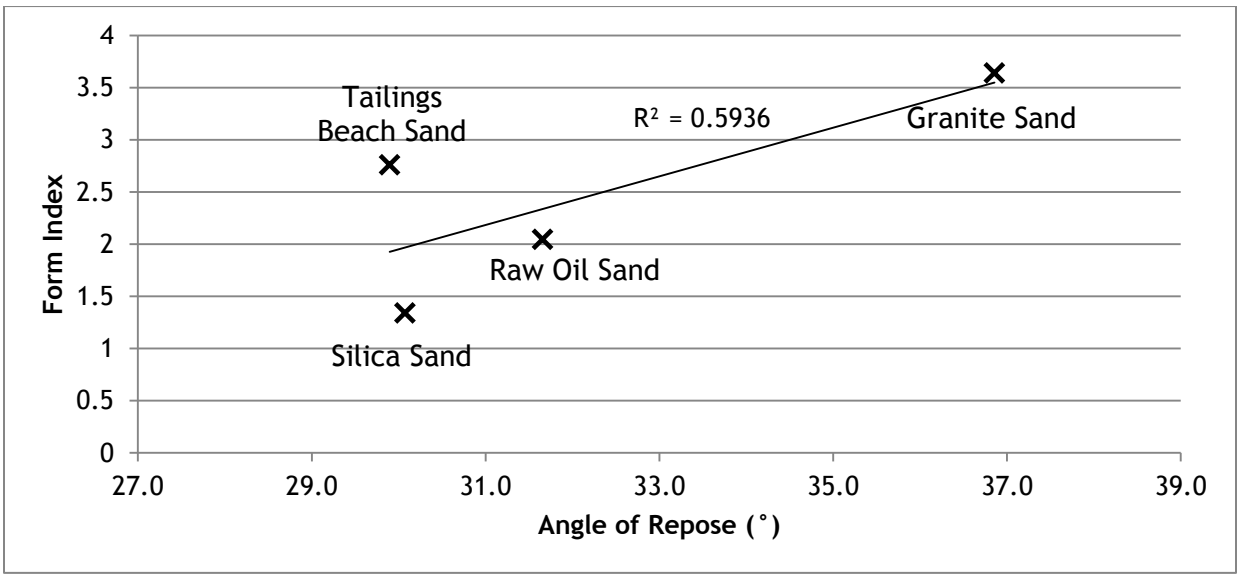


Form Index vs Angle of Repose and Correlation

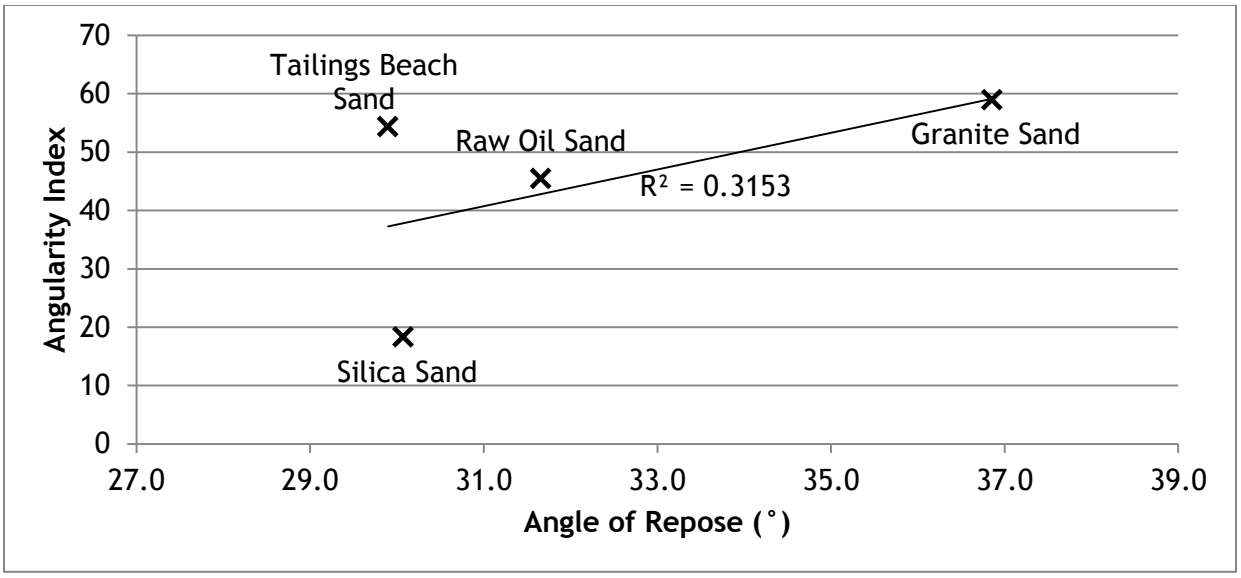


Angularity Index vs Angle of Repose and Correlation

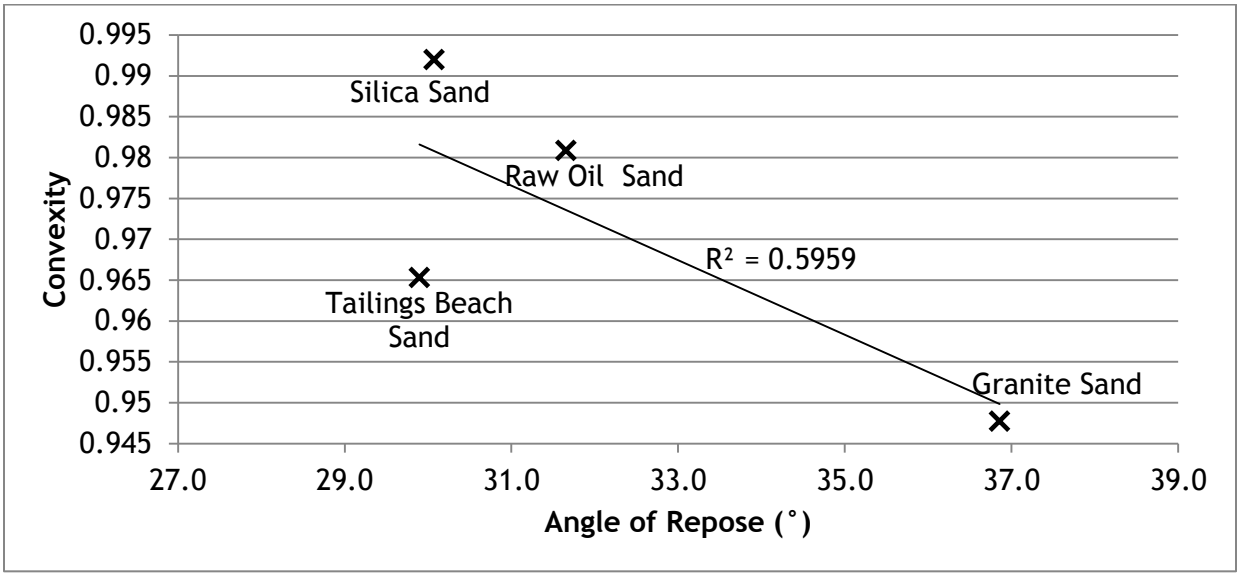


Convexity vs Angle of Repose and Correlation

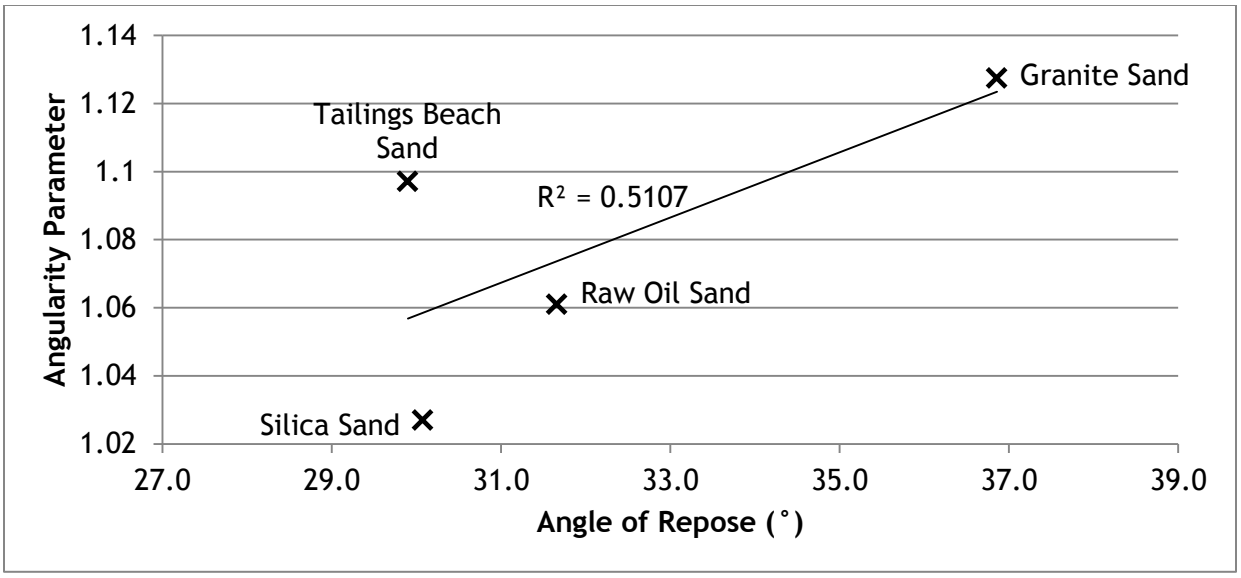


Angularity Parameter vs Angle of Repose and Correlation

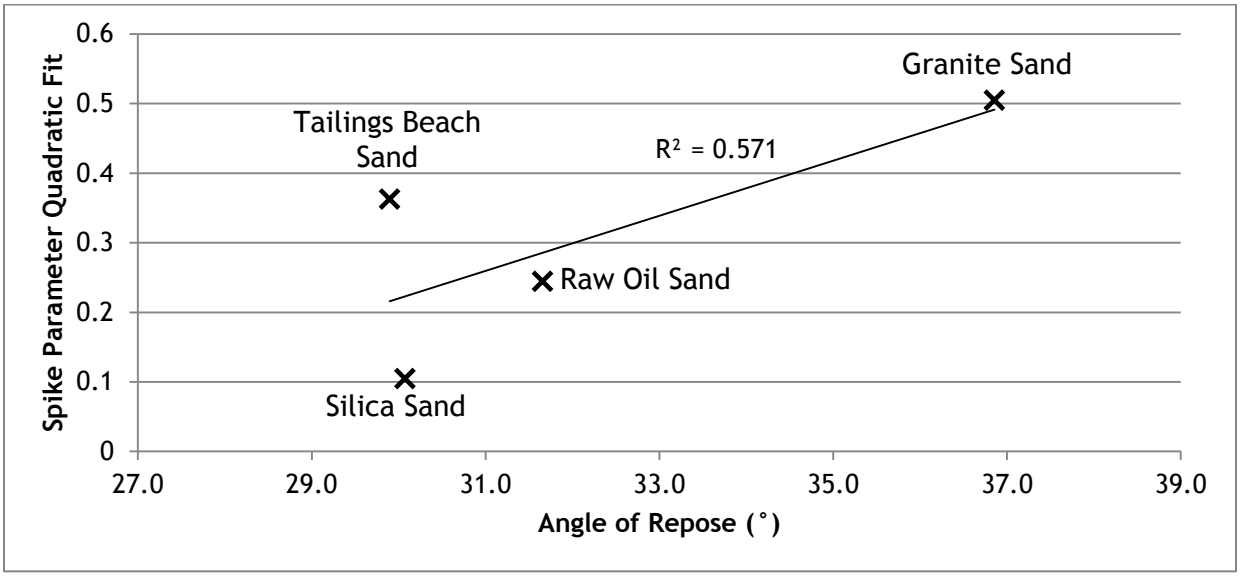


Spike Parameter Quadratic Fit vs Angle of Repose and Correlation